Draft version v6.5a (August 6, 2009)

The First *Fermi* Large Area Telescope Catalog of Gamma-ray Pulsars

Fermi LAT Collaboration and *Fermi* Pulsar Timing Consortium [1]

ABSTRACT

The dramatic increase in the number of known gamma-ray pulsars since the launch of the *Fermi Gamma-ray Space Telescope* (formerly GLAST) offers the first opportunity to study a sizable population of these high-energy objects. This catalog summarizes 46 high-confidence pulsed detections using the first six months of data taken by the Large Area Telescope (LAT), *Fermi*'s main instrument. Sixteen previously unknown pulsars were discovered by searching for pulsed signals at the positions of bright gamma-ray sources seen with the LAT, or at the positions of objects suspected to be neutron stars based on observations at other wavelengths. The dimmest observed flux among these gamma-selected pulsars is 6.0×10^{-8} ph cm^{-2} s^{-1} (for E>100 MeV). Twenty-four pulsars were discovered using ephemerides (timing solutions) derived from monitoring radio pulsars. Eight of these new gamma-ray pulsars are millisecond pulsars. The dimmest observed flux among these radio-selected pulsars is 1.4×10^{-8} ph cm^{-2} s^{-1} (for E>100 MeV). Such limiting flux, however, is not uniform over the sky owing to different background levels, especially near the Galactic plane. The remaining six gamma-ray pulsars were known since the *Compton Gamma Ray Observatory* mission, or before. Nearly all the energy spectra can be described by a power law with an exponential cutoff, and the cutoff energies lie in the range from just under 1 GeV to several GeV. The rotational energy loss ($dE/dt = \dot{E}$) of these neutron stars spans 5 decades, from 4.6 $\times$ 10^{38} erg s^{-1} down to $\sim 3 \times 10^{33}$ erg s^{-1}. Roughly 75% of the gamma-ray pulse profiles show two peaks, whereas the radio profiles of less than 30% of all known young pulsars have more than one peak. The pulse-shape parameters show substantial variety. Spatial associations suggest that many of these gamma-ray pulsars power pulsar wind nebulae. Tests of relations between the observed gamma-ray properties and the pulsar properties derived from the pulsars' rotation parameters show some correlations. For most of the pulsars, gamma-ray emission appears to come mainly from the outer magnetosphere, while polar-cap emission remains plausible for a remaining few.

Subject headings: catalogs — pulsars: general - Gamma-rays: observations

[1]Contact authors: G.A. Caliandro (andrea.caliandro@ba.infn.it), D. Parent (parent@cenbg.in2p3.fr), R.W. Romani (rwr@astro.stanford.edu)

1. Introduction

Following the 1967 discovery of pulsars by Bell and Hewish (Hewish et al. 1968), Gold (1968) and Pacini (1968) identified these objects as rapidly rotating neutron stars whose observable emission is powered by the slow-down of the rotation. With their strong electric, magnetic, and gravitational fields, pulsars offer an opportunity to study physics under extreme conditions. As endpoints of stellar evolution, these neutron stars, together with their associated supernova remnants and pulsar wind nebulae, help probe the life cycles of stars.

Over 1800 rotation-powered pulsars are now listed in the ATNF pulsar catalog (Manchester et al. 2005)[2]. The vast majority of these pulsars were discovered by radio telescopes. Small numbers of pulsars have been seen in the optical and X-ray bands.

In the high-energy gamma-ray domain ($\geq$ 30 MeV) the first indications for pulsar emission were obtained for the Crab pulsar by balloon-borne detectors (e.g. Browning et al. 1971), and confirmed by the SAS-2 satellite (Kniffen et al. 1974), which also found gamma radiation from the Vela pulsar (Thompson et al. 1975). The COS-B satellite provided additional details about these two gamma-ray pulsars, including a confirmation that the Vela pulsar gamma-ray emission was not in phase with the radio nor did it have the same emission pattern (light curve) as is seen in the radio (see e.g. Kanbach et al. 1980).

The *Compton Gamma Ray Observatory* (CGRO) expanded the number of gamma-ray pulsars to at least 7, with 6 or more of these seen by the CGRO high-energy instrument, EGRET. This gamma-ray pulsar population allowed a search for trends, such as the increase of efficiency (gamma-ray luminosity/spin-down luminosity) with decreasing values of the open field line voltage of the pulsar, first noted by Arons (1993). A summary of gamma-ray pulsar results in the CGRO era is given by Thompson (2004).

The third EGRET catalog (3EG; Hartman et al. 1999) included 271 sources of which $\sim$170 were unidentified. Determining the nature of these unidentified sources is one of the outstanding problems in high-energy astrophysics. Many of them are at high Galactic latitude and are most likely AGN or blazars. However, most of the sources at low Galactic latitudes ($|b| \leq 5°$) are associated with star-forming regions and hence may be pulsars, pulsar wind nebulae, supernova remnants, winds from massive stars, or high-mass X-ray binaries (e.g Kaaret & Cottam 1996; Yadigaroglu & Romani 1997; Romero et al. 1999). A number of newly-discovered radio pulsars were found in EGRET error boxes (e.g Kramer et al. 2003). Solving the puzzle of the unidentified sources will constrain pulsar emission models: pulsar population synthesis studies, such as those by Cheng & Zhang (1998), McLaughlin & Cordes (2000), and Gonthier et al. (2002), indicate that the number of detectable pulsars in either EGRET or *Fermi* data, as well as the expected ratio of radio-loud and radio-quiet pulsars (Harding et al. 2007), strongly depends on the assumed emission

[2]http://www.atnf.csiro.au/research/pulsar/psrcat

model.

The Large Area Telescope (LAT) on the *Fermi Gamma-ray Space Telescope* has provided a major increase in the known gamma-ray pulsar population, including pulsars discovered first in gamma rays (Abdo et al. 2009s) and millisecond pulsars (Abdo et al. 2009k) . The first aim of this paper is to summarize the properties of the gamma-ray pulsars detected by *Fermi*-LAT during its first six months of data taking. The second primary goal is to use this gamma-ray pulsar catalog to address astrophysical questions such as:

1. Are all the gamma-ray pulsars consistent with one type of emission model?
2. How do the gamma-ray pulsars compare to the radio pulsars in terms of physical properties such as age, magnetic field, spin-down luminosity, and other parameters?
3. Can any trends such as those suggested by the CGRO pulsars be found among measured or derived properties of the gamma-ray pulsars?
4. Which of the LAT pulsars are associated with supernova remnants, pulsar wind nebulae, unidentified EGRET sources, or TeV sources?

The structure of this paper is as follows: Section 2 describes the LAT and the pulsar data analysis procedures; Section 3 presents the catalog and shows some sample population statistics; section 4 studies the LAT sensitivity in detecting gamma-ray pulsars, and Section 5 is a discussion of the results. Finally, our conclusions are summarized in section 6.

2. Observations and Analysis

The *Fermi Gamma-ray Space Telescope* was successfully launched on 11 June 2008, carrying two gamma-ray instruments: the Large Area Telescope (LAT) and the Gamma-ray Burst Monitor (GBM). The LAT, *Fermi*'s main instrument, is described in detail in Atwood et al. (2009), with early on-orbit performance reported in (Abdo et al. 2009t). It is a pair-production telescope composed of a 4×4 grid of towers. Each tower consists of a silicon-strip detector and a tungsten-foil tracker/converter, mated with a hodoscopic cesium-iodide calorimeter. This grid of towers is covered by a segmented plastic scintillator anti-coincidence detector. The LAT is sensitive to gamma rays with energies in the range from 20 MeV to greater than 300 GeV, and its on-axis effective area is ~ 8000 cm^2 for $E > 1$ GeV.

Gamma-ray events recorded with the LAT have time stamps that are derived from a GPS-synchronized clock on board the *Fermi* satellite. The accuracy of the time stamps relative to UTC is < 1 μs (Abdo et al. 2009t). The timing chain from the GPS-based satellite clock through the barycentering and epoch folding software has been shown to be accurate to better than a few μs for binary orbits, and significantly better for isolated pulsars (Smith et al. 2008).

The LAT field-of-view is about 2.4 sr. Nearly the entire first year in orbit has been dedicated to an all-sky survey, imaging the entire sky every two orbits, i.e. every 3 hours. Data from any given point on the sky is recorded roughly $1/6^{th}$ of the time.

The gamma-ray point spread function (PSF) is energy dependent, and 68% of photons have reconstructed directions within $\theta_{68} \simeq 0.8^{\circ} E^{-0.75}$, where E is in GeV.

The larger effective area, the better source localization accuracy and better cosmic-ray rejection capabilities of LAT compared to EGRET lead to the detection of 46 gamma-ray pulsars in the first six months of LAT observations. These include the six gamma-ray pulsars seen with EGRET (Thompson 2004), the millisecond pulsar claimed by (Kuiper et al. 2000), and PSR J2021+3651 discovered in gamma-rays by *AGILE* (Halpern et al. 2008).

Two datasets are used to analyse the detected pulsars. For the spectral analysis the data are collected from the start of the *Fermi* sky-survey observation (4 August 2008 - shortly before the end of the commissioning period) until 1 February 2009, while the timing analysis starts from the first events recorded by the LAT after launch (25 June 2008). During the commissioning period, several configuration settings were tested that affected the LAT energy resolution and reconstruction. However, these changes had no effect on the LAT timing.

A first data selection keeps events with $E > 100$ MeV belonging to the '*diffuse*' event class, which has the tightest cosmic-ray background rejection (Atwood et al. 2009). To avoid albedo gamma-ray contamination, we select Good Time Intervals (GTIs) when the entire Region Of Interest (ROI) 10° around the source is above the albedo horizon of the Earth (105° below the zenith).

2.1. Timing Analysis

We have conducted two distinct pulsation searches of *Fermi* LAT data. One search utilizes the ephemerides of known pulsars, obtained from radio and X-ray observations. The other searches for periodicity in the arrival times of gamma rays coming from the direction of neutron star candidates ("blind period searches"). Both search strategies have advantages. The former is sensitive to lower gamma-ray fluxes, and the comparison of phase-aligned pulse profiles at different wavelengths is a powerful diagnostic of beam geometry. The blind period search allows for the discovery of new pulsars with selection biases different from those of radio searches, such as, for example, favoring pulsars with a broader range of inclinations relative to the magnetic axis. The number of observed radio-quiet (geminga-like) pulsars will constrain beaming models and population studies.

For each gamma-ray event (index i), the topocentric gamma-ray arrival time recorded by the LAT is transferred to solar-system barycentered (SSB) times t_i by correcting for the position of *Fermi* in the solar-system frame. The rotation phase $\phi_i(t_i)$ of the neutron star is calculated from a timing model, such as a truncated Taylor series expansion,

$$\phi_i(t_i) = \phi_0 + \sum_{j=0}^{j=N} \frac{f_j \times (t_i - T_0)^{j+1}}{(j+1)!}. \quad (1)$$

Here, T_0 is the reference epoch of the pulsar ephemeris and ϕ_0 is the pulsar phase at $t = T_0$. The coefficients f_j are the rotation frequency derivatives of order j. Different timing models are described in detail in Edwards et al. (2006). "Phase-folding" a light curve, or pulse profile, means filling a histogram of the ϕ_i values. An ephemeris includes the pulsar coordinates necessary for barycentering, the f_j and T_0 values, and may include parameters describing the radio dispersion measure (DM), the pulsar proper motion, glitch epochs, and more. The DM is used to extrapolate the radio pulse arrival time to infinite frequency, and the uncertainty in the DM translates to an uncertainty in the phase offset between the radio and gamma-ray peaks.

2.1.1. Pulsars with Known Rotation Ephemerides

The ATNF database[3] lists 1826 pulsars, and more have been discovered and await publication. The LAT observes them continuously during the all-sky survey. Phase folding the gamma rays coming from the positions of all of these pulsars (consistent with the energy-dependent LAT PSF) requires only modest computational resources. The challenge is the accuracy of the ephemerides. We have obtained 762 pulsar ephemerides from radio observatories, and 5 from X-ray telescopes, in two distinct groups.

The first group consists of 218 pulsars with high rotational-energy power ($\dot{E} > 10^{34}$ erg s^{-1}). These pulsars are regularly monitored as part of a timing campaign by a consortium of astronomers for the *Fermi* mission, as described in Smith et al. (2008). High-$\dot{E}$ pulsars are the best candidates for gamma-ray emission, but also the pulsars with the most rotational instabilities ("timing noise"). Such objects deserving of sensitive pulsation searches have ephemerides for which the necessary precision can degrade within days to months. With one exception (PSR J1124-5916, which faint in the radio and especially noisy), all of the 218 targets of the campaign have been timed regularly since shortly before *Fermi* launch. Some results from the timing campaign can be found in (Weltevrede et al. 2009b).

The second group is a sampling of pulsars from nearly the entire $P - \dot{P}$ plane (Figure 2) that are being timed for other studies, for which ephemerides were shared with the LAT team. These reduce the bias of the LAT gamma-ray-pulsar searches created by our current understanding of gamma-ray emission.

Table 3 lists which observatories provided ephemerides for the gamma-ray pulsars: "P" is the Parkes Radio Telescope (Manchester 2008) ; "J" is the Lovell Telescope at Jodrell Bank (Hobbs

[3]http://www.atnf.csiro.au/research/pulsar/psrcat/ version 1.36, Manchester et al. (2005)

et al. 2004) ; "N" is the Nançay Radio Telescope (Theureau et al. 2005) ; "G" is the Green Bank Telescope (Kaplan et al. 2005) ; "A" is the Arecibo Telescope (Dowd et al. 2000) ; and "W" is the Westerbork Synthesis Radio Telescope (Voûte et al. 2002). "L" indicates that the pulsar was timed using LAT gamma rays, as described in the next section. The rms' of the radio timing residuals for most of the solutions used in this paper are $< 0.5\%$ of a rotation period, but range as high as 1.2% for five of them. The ephemerides used for this catalog will be available on the *Fermi* Science Support Center data servers[4].

2.1.2. Blind Period Search for Gamma-ray Pulsations

For all 16 of the pulsars found in the blind searches of the LAT data, we determined the timing ephemerides used in this catalog directly from the LAT data as described below. In addition, for two other pulsars the LAT data provided the best available timing model. The first is the radio-quiet pulsar Geminga. Since Geminga is such a bright gamma-ray pulsar, it is best timed directly using gamma-ray observations. During the period between EGRET and *Fermi*, occasional XMM-*Newton* observations maintained the timing model (Jackson & Halpern 2005) but a substantially improved ephemeris has now been derived from the LAT data (Abdo et al. 2009b). The second is PSR J1124−5916, which is extremely faint in the radio (80 μJy at 1400 Mhz, see Table 2) and exhibits a large amount of timing noise (Camilo et al. 2002b). In this section, we briefly describe the blind pulsar searches and how the timing models for these pulsars are created. These pulsars have an "L" in the "ObsID" column of Table 3.

Even though the gamma-ray energy flux from a young pulsar can be several percent of the neutron star's spin-down energy, the gamma-ray counting rates are low. As an example, the LAT detects a gamma ray from the Crab pulsar approximately every 500 rotations, when the Crab is well within the LAT's field-of-view.

Such sparse photon arrivals make periodicity searches difficult. Extensive searches for pulsations performed on the data from EGRET (Chandler et al. 2001) were just sensitive enough to detect the very bright Geminga pulsar in a blind search, though by the time this was done the pulsar had already been detected by other means. The time-differencing method used in this work found four of the EGRET pulsars (Ziegler et al. 2008). Blind searches of *Fermi* sources for all other EGRET sources proved fruitless.

By contrast, the improvements afforded by the LAT, particularly the much larger effective area combined with the greatly reduced background made possible by the improved point spread function, have enabled highly successful blind searches for pulsars. In the first six months of operation, we discovered a total of 16 new pulsars in direct pulsation searches of the LAT data (see e.g. Abdo et al. 2008, 2009s).

[4]http://fermi.gsfc.nasa.gov/ssc/

A computationally efficient time-difference search technique made these searches possible (Atwood et al. 2006), enabling searches of hundreds of *Fermi* sources to be performed on a small computer cluster with only a modest loss in sensitivity compared to fully coherent search techniques. Still, owing to the large number of frequency and frequency derivative trials required to search a broad parameter space, the minimum gamma-ray flux needed for a statistically significant detection is considerably higher than the minimum flux needed for the phase-folding technique using a known ephemeris.

We performed these blind searches on over one hundred candidate sources identified before launch and on another couple of hundred newly detected LAT sources. Of the 16 pulsars detected in these searches, 13 are associated with previously known EGRET sources. The discoveries include several long-suspected pulsars in SNRs and known PWNe.

These 16 pulsars are gamma-ray selected, as they were discovered by the LAT and thus the population is subject to very different selection effects than the general radio pulsar population. However, this does not necessarily imply that they are radio quiet. For several cases, deep radio searches have already been performed on known PWN or X-ray point sources suspected of harboring pulsars. But in most cases, new radio searches are required to ensure that there is no radio pulsar counterpart down to a meaningful luminosity limit. These searches are now being undertaken and are yielding the first results (Camilo et al. 2009b).

For these 18 pulsars (16 new plus Geminga and PSR J1124-5916), we derived timing models from the LAT data using the procedure summarized here. A more detailed description of pulsar timing using LAT data can be found in (Ray et al. 2009). We selected photons from a small Region Of Interest (ROI) around the pulsar with a radius of $lessim 0.5°$ or $lessim 1°$ (see further Section 2.1.3 and Table 3). We used *diffuse* class photons with energies above a cutoff (typically $E > 300$ MeV) selected to optimize the signal to noise ratio for that particular pulsar. We converted the photon arrival times to the geocenter using the GTBARY science tool. This correction removes the effects of the spacecraft motion about the Earth, resulting in times as would be observed by a virtual observatory at the geocenter.

Using an initial timing model for the pulsar, we then used TEMPO2 (Hobbs et al. 2006) in its predictive mode to generate polynomial coefficients describing the pulse phase as a function of time for an observatory at the geocenter. Using these predicted phases, we produced folded pulse profiles over segments of the LAT observation. The length of the segments depends on the brightness of the pulsar but are typically 10–20 days. We then produced a pulse time of arrival (TOA) for each data segment by Fourier domain cross-correlation with a template profile (Taylor 1992). The template profile for most of the pulsars is based on a multi-gaussian fit to the observed LAT pulse profile. However, in the case of Geminga, which has very high signal to noise and a complex profile not well described by a small number of gaussians, we used a template profile that was the full mission lightcurve itself.

Finally, we used TEMPO2 to fit a timing model to each pulsar. For most of the pulsars, the model includes pulsar position, frequency and frequency derivative. In several cases, the fit also required a frequency second derivative term to account for timing noise. And in the case of PSR J1124−5916, we required three sinusoidal *"fitwave"* terms (Hobbs et al. 2006) to produce a model with white residuals. For two of the blind search pulsars (J1741−2054 and J1809−2332) the positions were too close to the ecliptic plane for the position to be well constrained by pulsar timing and thus we fixed the positions based on X-ray observations of the presumed counterparts. For Geminga and PSR J1124−5916 we also used external, fixed positions because they were of much higher precision than could be determined from less than one year of *Fermi* timing. The rms' of the timing residuals are between 0.5 and 2.0% of a rotation period, with one outlier ($< 3\%$ for PSR J1459-60).

2.1.3. Light curves

The light curves of 46 gamma-ray pulsars detected by the LAT are shown in figures 13 to 58. The gray light curve in the top panel includes all photons with $E > 0.1$ GeV, while the other panels show the profiles in exclusive energy ranges: $E > 1.0$ GeV (with $E > 3.0$ GeV in black) in the second panel from the top ; 0.3 to 1.0 GeV in the next panel; and 0.1 to 0.3 GeV in the fourth panel. Phase-aligned radio profiles for the radio selected pulsars are in the bottom panel. The light curves are plotted with 25 or 50 bins, requiring a) at least 50 counts per bin in the peak and b) that the RMS of the timing solution normalized to the pulsar period is smaller than the bin resolution, $RMS/P \leq BinWidth/\sqrt{12}$.

Table 3 lists the Z_2^2 (Buccheri et al. 1983) and H (de Jager et al. 1989) periodicity test values for the energy range $E > 0.3$ GeV. Detection of gamma-ray pulsations are claimed when the significance of the periodicity test exceeds 5σ (i.e. a chance probability of $< 6 \times 10^{-7}$). We have used the Z-test with $m = 2$ harmonics (Z_2^2) which provides an analytical distribution function for the null hypothesis described by a χ^2 distribution with $2m$ degrees of freedom. The H-test uses Monte-Carlo simulations to calculate probabilities, limited to a minimum of 4×10^{-8}. Each method is sensitive to different pulse profile shapes. Four pulsars in the catalog fall short of the 5σ significance threshold in the six-month data set with the selection cuts applied here: the 3 millisecond pulsars J0218+4232, J0751+1807, and J1744-1134 reported in Abdo et al. (2009k), and the radio pulsar PSR J2043+2740. The characteristic pulse shape as well as the trend of the significance versus time lead us to include the latter in the catalog.

Table 3 also lists "maxROI", the maximum angular radius around the pulsar position within which gamma-ray events were searched for pulsations, generally 1.0°, but 0.5° in some cases. The choice was made by using the energy spectrum for the phase-averaged source, described in Section 2.2, to maximize S^2/N over a grid of maximum radii and minimum energy thresholds (where S is the number of counts attributed to the point source, and N is the number of counts due to the diffuse background and neighboring sources). We selected photons within a radius equal to θ_{68} (68% of the PSF) of the pulsar position, requiring a radius of at least 0.35°, but no larger than the reported "maxROI".

The background level drawn in the gray light curves (top panel) was computed from the diffuse emission model fitted by the likelihood spectral analysis described in Section 2.2. Several parameters regarding the light curve shape are evaluated from the full energy range light curve (top panel). These are reported in table 6, including the peak multiplicity (2nd column), the phase difference Δ between the main peaks (3rd column), and the lag δ of the first gamma peak from the main radio peak for the radio selected pulsars (4th column).

2.2. Spectral analysis

The pulsar spectra were fitted with an exponentially cutoff power-law model of the form

$$\frac{\mathrm{d}N}{\mathrm{d}E} = K E_{\mathrm{GeV}}^{-\Gamma} \exp\left(-\frac{E}{E_{\mathrm{cutoff}}}\right) \tag{2}$$

in which the three parameters are the spectral index at low energy Γ, the cutoff energy E_{cutoff}, and a normalization factor K, in units of [ph cm^{-2} s^{-1} MeV^{-1}], in keeping with the observed spectral shape of bright pulsars (Abdo et al. 2009m). The energy at which the normalization factor K is defined is arbitrary. We chose 1 GeV because it is, for most pulsars, close to the energy at which the relative uncertainty on the differential flux is minimal.

Because the spatial resolution of the LAT is not very good at low energy ($\sim 5°$ at 100 MeV) and we wished to extend the spectra that low in order to measure the curvature, we needed to account for all neighboring sources and the diffuse emission together with each pulsar. This was done using the framework used for the LAT Bright Source List (Abdo et al. 2009o). A 6-month source list was generated in the same way as the 3-month source list described in Abdo et al. (2009o), but covering the extended period of time used for the pulsar analysis.

We used an underlying Galactic diffuse model similar to that used in Abdo et al. (2009o) (based on GALPROP). The particular GALPROP designation for our model is `54_77varh7S`. It is an evolution of the previous model, which is consistent with the electron spectrum measured by *Fermi* (Abdo et al. 2009p).

We have added the source Cyg X-3 (Abdo et al. 2009c), although it was not detected automatically as a separate source, because it is very close to PSR J2032+4127, and impacts the spectral fit of the pulsar. Cyg X-3 was fit with a simple power-law as were all other non-pulsar sources in the list.

We extracted events in a circle of radius 10° around each pulsar, and included all sources up to 17° into the model (sources outside the extraction region can contribute at low energy). Sources further away than 3° from the pulsar were assigned fixed spectra, taken from the all-sky analysis. Spectral parameters for the pulsar and sources within 3° of it were allowed to be free for the analysis.

The fit was performed by maximizing unbinned likelihood (direction and energy of each event is considered) as described in Abdo et al. (2009o) and using the MINUIT fitting engine. The uncertainties on the parameters were estimated from the quadratic development of the log(likelihood) surface around the best fit.

In addition to the index Γ and the cutoff energy $E_{\rm cutoff}$ which are explicit parameters of the fit, the important physical quantities are the photon flux F_{100} [ph cm^{-2} s^{-1}] and the energy flux G_{100} [MeV cm^{-2} s^{-1}]

$$F_{100} = \int_{100\,\rm MeV}^{100\,\rm GeV} \frac{{\rm d}N}{{\rm d}E}{\rm d}E \tag{3}$$

$$G_{100} = \int_{100\,\rm MeV}^{100\,\rm GeV} E\frac{{\rm d}N}{{\rm d}E}{\rm d}E \tag{4}$$

These are derived quantities, obtained from the primary fit parameters. Their uncertainties are obtained using their derivatives with respect to the primary parameters and the covariance matrix obtained from the fitting process.

For a number of pulsars, an exponentially cutoff power-law spectral model is not significantly better than a simple power-law. We identified these by computing $TS_{\rm cutoff} = 2\Delta$log(likelihood) (comparable to a χ^2 distribution with one degree of freedom) between the models with and without the cutoff. Pulsars with $TS_{\rm cutoff} < 10$ have poorly measured cutoff energies. These values are reported in Table 4.

The initial analysis does not make use of the pulsars' light curves, and results in a fit to the overall spectrum, including both the pulsar and any underlying unpulsed emission above the background.

To account for the fact that several pulsars (starting with the Crab) have a known pulsar wind nebula, we have split the data between on-pulse and off-pulse, on the basis of the light curve. The off-pulse phases are defined in the last column of Table 6. The off-pulse spectrum was modeled by a simple power-law, which is not ideal for the Crab or any other pulsar wind nebula that might have both a synchrotron and inverse Compton component inside the Fermi energy range. However, it is not possible to generate a better model except for a handful of pulsars. For consistency, we used the power-law in all cases.

In a second step we fitted the on-pulse emission to the exponentially cutoff power-law form of Eq. 2, on top of the off-pulse emission obtained above, scaled to the on-pulse phase interval. That fit was done in exactly the same way as that of the overall spectrum described before. In many cases the off-pulse emission was not significant at the 5σ or even 3σ level, but we kept the formal best fit anyway, in order not to bias the pulsed emission upwards.

The results of the on-pulse emission are summarized in Table 4, where the 2^{nd} and 3^{rd} columns are F_{100} and G_{100} evaluated for on-pulse emission, the 4^{th} column is the spectral index, and the 5^{th} is the energy of the cutoff. The last two columns are the test statistic (TS) for the source significance and the $TS_{\rm cutoff}$.

Judging from the Crab pulsar itself, the main effect of using a simple power-law to model the off-pulse emission is on the value of the cutoff energy. Here, $E_{\rm cutoff}$ for the Crab is found to be very high (> 10 GeV) in comparison to ~ 6 GeV from the dedicated analysis (Abdo et al. 2009d). However, the photon and energy fluxes (while formally incompatible due to very small errors) are within 10% of the values obtained with a correct model for the nebula.

For these reasons, the spectral results reported for the Crab in Table 4 are from the dedicated analysis (Abdo et al. 2009d). One additional exception in Table 4 is for PSR J1836+5925. The off-pulse analysis result for this pulsar was unclear, so the spectral parameters reported in the Table are from the initial, phase-averaged spectral analysis.

We have checked whether our imperfect knowledge of the Galactic diffuse emission may impact the pulsars' parameters by applying the same analysis with a different diffuse model, as was done in Abdo et al. (2009o). The overall emission is affected. Seven (relatively faint) pulsars see their flux move up or down by more than a factor 1.5. On the other hand, the pulsed flux is much more robust, because the off-pulse component absorbs part of the background difference, and the source-to-background ratio is better after on-pulse phase selection. Only two pulsars see their pulsed flux move up or down by more than a factor 1.2, and none by more than 1.4.

The pulsar spectra were also evaluated using an unfolding method (D'Agostini 1995; Mazziotta 2009), that takes into account the energy dispersion introduced by the instrument response function and does not assume any model for the spectral shapes. "Unfolding" is essentially a deconvolution of the observed data from the instrument response functions. For each pulsar we selected photons within 68% of the PSF with a minimum radius of 0.35° and a maximum of 5 deg.

The observed pulsed spectrum was built by selecting the events in the on-pulse phase interval and subtracting the events in the off-pulse interval, properly scaled for the phase ratio. The instrument response function, expressed in terms of a smearing matrix, was evaluated using the Monte Carlo simulation package *Gleam*, a *Geant4* based simulation code of the instrument, and taking into account the pointing history of the source.

The true pulsar energy spectra were then reconstructed from the observed ones using an iterative procedure based on Bayes' theorem (Mazziotta 2009). Typically, convergence is reached after a few iterations. When the procedure has converged, both statistical and systematic errors on the observed energy distribution can be easily propagated to the unfolded spectra.

The results obtained from the unfolding analysis were found to be consistent with the likelihood analysis results.

3. Catalog description and sample population statistics

The characteristic parameters of the detected gamma-ray pulsars are summarized in Table 2. The first two columns are pulsar names and types. We label with r the radio-selected pulsars, g gamma-selected, m milliseconds, and b binary pulsars. LAT detected five pulsars in binary systems and all of them are millisecond pulsars. The 3^{rd} and 4^{th} columns in the Table are Galactic coordinates. The 5^{th} and 6^{th} columns list the period (P) and its first derivative ($\dot{P}$). For the evaluation of this latter parameter, the kinematic Shklovskii effect (Shklovskii 1970) is taken into account: $\dot{P} = \dot{P}_{\rm obs} - \mu^2 P_{\rm obs} d/c$, where μ is the pulsar proper motion, and d the distance. This effect is especially important for the millisecond pulsars (Abdo et al. 2009k).

The next columns, except for the last one, are parameters derived from P and $\dot{P}$ assuming a dipolar magnetic field for the pulsars. They are: characteristic age

$$\tau = P/2\dot{P}, \tag{5}$$

spin-down luminosity

$$\dot{E} = -I\Omega\dot{\Omega} = -4\pi^2 I\nu\dot{\nu} = 4\pi^2 I\dot{P}P^{-3}, \tag{6}$$

and the neutron star's magnetic field at the 'light cylinder'

$$B_{\rm LC} = \left(\frac{3I8\pi^4\dot{P}}{c^3P^5}\right)^{1/2} \approx 2.943\times 10^8(\dot{P}P^{-5})^{1/2}. \tag{7}$$

In these expressions $\Omega \equiv 2\pi\nu \equiv 2\pi/P$, and I is the neutron star's moment of inertia, taken to be 10^{45}g cm^2. The radius of the light cylinder is defined as $R_{\rm LC} = c/\Omega = cP/2\pi$. The last column is the radio flux density at 1400 MHz, or an upper limit when one is available.

The pulsar distribution in the Galaxy is shown in Figure 1, while Figure 2 displays the P-$\dot{P}$ space filled with the LAT pulsars and all of the ATNF catalog (small dots). In these plots the normal gamma-ray pulsars are marked with a circle, the millisecond pulsars with a triangle, and the gamma-selected ones with a square. The small black dots are all the radio pulsars for which we have searched for gamma-ray pulsations without success. The gray dots represent all other pulsars in the ATNF catalog. These symbols are used for the otherfigures.

The light curve parameters listed in Table 6 are summarized in Figure 3, showing the gamma-peak separation Δ versus the radio lag δ . As we will discuss in section 5, high-magnetosphere emission models predict correlations between these parameters.

In this framework, the magnetic field $B_{\rm LC}$ at the light cylinder ($R_{\rm LC}$) turns out to be an interesting quantity for the gamma-ray pulsars. Figure 4 shows $B_{\rm LC}$ versus the characteristic age (τ) for the known pulsars. From this plot we note that, even though the millisecond pulsars are well-separated from the main population, their magnetic fields at the light cylinder are comparable with those of the other gamma-ray pulsars. This suggests that the emission mechanism for the two families of pulsars is the same.

In Figure 5 we plot the cutoff energy versus $B_{\rm LC}$, with the energy cutoff histogram on the right Y axis. This plot seems almost flat until at least 5×10^4 G.

In Figures 6 and 7 we plot the spectral index, and the gamma-ray peak separation versus $\dot{E}$, respectively. The histogram of the spectral indexes is distributed around ~ 1.5. The Δ distribution is bimodal `[histogram to be added to Figure 7]`, with gamma-ray peak separations peaking at ~ 0.15 and ~ 0.5 in phase.

Relating the observed energy flux G_{100} to total gamma-ray luminosity L_γ provides important model constraints and is also crucial for testing predicted population trends of L_γ vs. $\dot{E}$. The luminosity L_γ may be estimated as follows:

$$L_\gamma \equiv 4\pi d^2 f_\Omega G_{100}, \tag{8}$$

where G_{100} is the measured energy flux between $10^2 - 10^5$ MeV (Eq 4) and f_Ω is the flux correction factor (Watters et al. 2009). The factor f_Ω is model dependent and is a function of the magnetic inclination and observer angles α and ζ. For instance, a larger f_Ω is needed for pulsars with large impact angles $\beta = \zeta - \alpha$ if a particular model predicts low-level off-beam emission.

For both the outer gap and slot gap models Watters et al. (2009) find that $f_\Omega \sim 1$, in contrast to earlier adoption of $f_\Omega = 1/4\pi \approx 0.08$ (in e.g. Thompson et al. 1994), or $f_\Omega = 0.5$ for millisecond pulsars (in e.g. Fierro et al. 1995). For simplicity, we use $f_\Omega = 1$ throughout the paper. The geometry dependence of f_Ω may lead to an artificial spread of the calculated L_γ value. This is also true in the case of the outer gap model of Zhang et al. (2004), where $L_\gamma = f^3(P, B, \alpha)\dot{E}$ is dominated by the fractional gap size f.

Once L_γ is estimated, we may obtain the gamma-ray conversion efficiency $\eta_\gamma \equiv L_\gamma/\dot{E}$. This may be written as:

$$\eta_\gamma \approx 0.0486 f_\Omega d_1^2 G_{100} I_{45}^{-1} \dot{P}_{-15}^{-1} P_{0.1}^3, \tag{9}$$

where G_{100} is measured in 10^{-5} MeV cm^{-2} s^{-1}, $I_{45} = I/10^{45}\ \mathrm{g\,cm^2}$, $\dot{P}_{-15} = \dot{P}/10^{-15}\ \mathrm{s\,s^{-1}}$, $P_{0.1} = P/0.1$ s and $d_1 = d/1$ kpc. The quadratic contribution of the distance implies that uncertainties in distance will dominate uncertainties in the estimated L_γ and η_γ. We discuss the distance estimates used to evaluate L_γ in Section 3.1.

The luminosity L_γ and the gamma-ray conversion efficiency η_γ evaluated as described are listed in the last two columns of Table 4.

Figure 8 is a plot of L_γ vs. $\dot{E}$. The dashed line signifies $L_\gamma = \dot{E}$, while the dot-dashed line indicates $L_\gamma \propto \dot{E}^{1/2}$.

The 6 EGRET pulsars, the least and the most luminous millisecond pulsars (J0437-4715 and J0218+4232 respectively), as well as PSR J1836+5925 are labeled. For the latter pulsar, only an upper limit is known for the distance. Also, are labeled PSR J0659+1414, PSR J2021+4026, and PSR J0205+6449. We assumed a 30% systematic error on G_{100}. For distances evaluated from dispersion measurements (DM) a 30% error is taken into account, as well as for pulsars with a range of estimated distances. These last have two luminosity evaluation connected by dashed error bars. The largest error bars are due to distance errors greater than 50%.

Since gamma-radiation usually dominates the total radiation output $L_{\rm tot}$ from pulsars, we set $L_{\rm tot} \approx L_\gamma$. The Crab is, however, a notable exception, where the X-ray luminosity $L_X \sim 10 L_\gamma$. In this case $L_{\rm tot}$ is evaluated as $L_X + L_\gamma$, where L_γ is the Fermi luminosity for $E > 100$ MeV, while L_X is estimated for $E < 100$ MeV from the data in figure 9 of Kuiper et al. (2001). This has been taken into account in Figure 8. A break is clearly seen around $\dot{E}_{\rm break} \sim 10^{35}$ erg s^{-1}. While the millisecond pulsars seem to follow $L_\gamma \propto \dot{E}$, the pulsars with higher $\dot{E}$ seem to follow a trend which is flatter than the expected $L_\gamma \propto \dot{E}^{1/2}$.

3.1. Distances

The conversion of the detected fluxes to the energy emitted by the pulsars is based on a reliable evaluation of the distances. The most direct method to evaluate distances is the annual trigonometric parallax. Parallax measurements provide the highest confidence distance estimates, however, it also requires the measurement of the pulsar proper motion. Therefore, it can only be applied if the source is close and bright enough, which is the case only for a few pulsars.

A commonly used technique to estimate distances for radio pulsars involves the dispersed pulse profiles as a function of wavelength due to (mainly) free electrons between the pulsars and Earth. A distance can be computed from the Dispersion Measure (DM) coupled to an electron-density-distribution model. Currently, the most commonly used model is the NE 2001 model by Cordes & Lazio (2002). It is based on average values of the electron distribution in the Galaxy. For some directions the model is not suitable to describe the real local circumstances. The pulsars in the Cygnus region illustrate its limitations. NE 2001 assumes uniform electron densities in and in between the Galactic spiral arms, with smooth transitions between zones. The line-of-sight to Cygnus coincides with a tangent to a spiral arm and the highly un-smooth nature of the edges of the arm cause significant discrepancies between the true pulsar distances and those inferred from the electron-column density.

A third method, kinematic, uses the association of the pulsar with objects whose distance can be measured from absorption or emission lines in the neutral hydrogen (HI) spectrum. In this case, most of the associations are not precisely in the directions of the pulsars and the distance measurements are controversial. The kinematic-distance method is based on a rotation curve of the Galaxy. It breaks down in the directions where the velocity gradients become very small or where the distance-velocity relation has double values.

In a small number of cases, the distance is evaluated from X-ray observations either from measurements of the absorbing column at low energies (below 1 keV) or from consideration on the detected flux assuming some standard parameters of the neutron star.

Table 1 presents the best known distances of 37 pulsars detected by *Fermi*, the methods used to obtain them and the references. All distances derived from DM are computed using the Cordes & Lazio (2002) model and the references quoted in Table 1 are related to the DM measurements. Uncertainties for this method are function of the DM and the direction. To take into account systematic uncertainties, we assume a minimum uncertainty value of 30%. Whenever distances from different methods do not agree and no method is more convincing than the other, a distance range is presented. In these cases 30% uncertainties in the upper and lower values are assumed.

For the remaining 9 *Fermi*-discovered pulsars no distance estimates have been established so far. Some distance values reported in Table 1 require comments, here listed:

PSR J0205+6449 – The pulsar, within the nebula 3C 58, has a DM=141 cm^{-3} pc (Camilo et al. 2002c) that with the Taylor & Cordes (1993) model gives a distance of 6.4 kpc (Malofeev et al. 2003). This value is about twice the distance of the nebula placed between 2.6 kpc (Green & Gull 1982) and 3.2 kpc (Roberts et al. 1993) using HI absorption and emission lines from the SNR. The lower V-band reddening (Fesen et al. 1988, 2008) compared to the Galactic-disk edge (Schlegel et al. 1998) suggests that the SNR is in the range 3–4 kpc. Table 1 quotes the distance range found by Green & Gull (1982) and Roberts et al. (1993).

PSR J0218+4232 – The distance to the only millisecond pulsar which was marginally detected by EGRET (Kuiper et al. 2000) is rather uncertain. Applying the DM measurements by Navarro et al. (1995) to the NE 2001 model, the distance estimate is 2.7 ± 0.6 kpc. Studying the parameters of the binary system, Bassa et al. (2003) gave a new estimate by comparing the characteristic age of the pulsar with the cooling models of its white-dwarf companion. The best agreement between the ages of the white dwarf and neutron star yielded to a distance range of 2.5 to 4 kpc.

PSR J0248+6021 – The large DM of 376 cm^{-3} pc (Cognard I. et al 2009) puts this pulsar beyond the edge of the galaxy for this line-of-sight. The line-of-sight, however, borders the giant HII region W5 in the Perseus Arm and the distance estimate could be affected by a dense local environment. We bracket the pulsar distance as being between W5 (2 kpc) and the Galaxy edge (9 kpc).

PSR J0534+2200 – The Crab pulsar and its nebula belong to the best studied sources in the sky. Despite many instruments over the entire electromagnetic spectrum have observed the system, the distance is poorly known. According to Kaplan et al. (2008) neither timing parallax, radio interferometric parallax, nor optical parallax measurements are likely to significantly improve our knowledge of the pulsar's distance in the near future. The estimate of the distance reported in Table 1 is performed by Trimble (1973) using several different methods.

PSR J0631+1036 – The pulsar has a large DM of 125.3 cm^{-3} pc (Zepka et al. 1996) for a source located close to the Galaxy anticentre. The dark cloud LDN 1605, which is part of the active star-forming region 3 Mon, is along the line of sight and the conversion to distance could overestimate the value because of ionized material in the cloud. The distance of the cloud is $\sim$0.75 kpc and the pulsar could be inside the cloud (Zepka et al. 1996).

PSR J1124−5916 – It is located in the direction of the Carina arm where the models of the electron density are affected by systematic errors. Camilo et al. (2002b) determine 5.7 kpc. The kinematic distance of the associated SNR (G292.0+1.8) indicates a lower limit of 6.2±0.9 kpc (Gaensler & Wallace 2003) which is higher than the previous evaluation of 3.2 kpc (Caswell et al. 1975) performed with the same method. The value quoted in Table 1 is derived by Gonzalez & Safi-Harb (2003) linking the absorbing column detected in X-rays with the extinction along the pulsar direction.

PSR J1418−6058 – This pulsar is likely associated with the Rabbit PWN (G313.3+0.1), nearby the Kookaburra complex. Nearby HII measurements suggest a distance of 13.4 kpc (Caswell & Haynes 1987), but this HII region could easily be in the background of the complex and such high distance would imply an unreasonable large gamma-ray efficiency. In Table 1 we quote a crude estimate of the distance range with the lower limit (Yadigaroglu & Romani 1997) determined from the assumption that the pulsar is related to one of the near objects (Clust 3, Cl Lunga 2 or SNR G312-04) and the higher limit (Ng et al. 2005) determined by appling the relation found by Possenti et al. (2002) and the correlation between pulsar X-ray spectral index and luminosity given by Gotthelf (2003).

PSR J1709−4429 – The pulsar DM locates the pulsar at a distance of 2.31±0.69 Kpc (Koribalski et al. 1995). Kinematic distances, also available for this pulsar, give upper and lower limits of 3.2 ±0.4 kpc and 2.4 ±0.6 kpc, respectively (Koribalski et al. 1995). The X-ray flux from the neutron star detected by *Chandra* (Romani et al. 2005) and XMM-*Newton* (McGowan et al. 2004) is compatible with a distance of 1.4–2.0 kpc. We assume the range 1.4–3.6 kpc.

PSR J1747−2958 – The pulsar is associated with the radio source G359.23−0.82 better known as The Mouse. HI measurements yielded a distance upper limit of 5.5 kpc (Uchida et al. 1992), but the DM (101 pc cm^{-3}) suggests a closer value of 2.0±0.2 kpc (Camilo et al. 2002a). The X-ray absorbing column detected by *Chandra* suggests that the pulsar lies at a distance between 4 and 5 kpc, while the closer value of 2 kpc would imply an ad-hoc molecular cloud behind the pulsar (Gaensler et al. 2004).

PSR J1952+3252 – It is better known as B1951+32 and it is associated with SNR CTB80. The distance evaluated from DM is 3.1±0.2 kpc (Strom & Stappers 2000), but the kinematic distance is rather 2 kpc (Greidanus & Strom 1990).

PSR J2021+3651 – The DM (369 pc cm^{-3}) locates it at a distance ∼12 kpc that would imply a very high gamma-ray conversion efficiency respect to the other observed pulsars (Van Etten et al. 2008). Considering that the open cluster Berkeley 87 is near the line-of-sight of this pulsar, it is reasonable to expect an electron column density higher than foreseen by the Cordes & Lazio (2002) model. The value quoted in the Table 1 is provided by Van Etten et al. (2008) from a *Chandra* X-ray observation of the pulsar and its surrounding nebula. Assuming canonical values for the radius and the mass of the neutron star, the emission detected from the neutron star is compatible with a distance of $2.1^{+2.1}_{-1.0}$ kpc (value quoted in Table 1). A similar range (1.3–4.1 kpc) was obtained for the X-ray flux detected from the associated PWN.

PSR J2032+4127 – The measured DM value (115 pc cm^{-3}) would imply a distance of 3.6 kpc, however, if the pulsar belongs to the star cluster Cyg OB2, its distance would be between 1.45 and 1.7 kpc (Camilo et al. 2009b).

PSR J2229+6114 – The distance evaluated from the X-ray absorption column (Halpern et al. 2001b) before the discovery of pulsed emission from the source is $\sim$3 kpc. This value is between the value obtained from the DM (6.5 kpc; Halpern et al. 2001a) and the one yielded by kinematic method (0.8 kpc; Kothes et al. 2001). These two values are quoted as a range in Table 1.

To show how these pulsars are distributed around us, the projection of the sky on the Galactic plane is plotted in Figure 9. The large star represents the Galactic center. The two circles are centered on the Sun with the radii of 3 kpc and 5 kpc.

3.2. Associations

Table 5 shows some alternate names and positional associations of the pulsars in this catalog with other astrophysical sources. Column 2 shows alternate pulsar names, those with B1950 or colloquial names. Column 3 shows the name appearing in the LAT Bright Source List (Abdo et al. 2009o). Column 4 shows positional associations with EGRET sources. Column 5 gives positional associations with supernova remnants and pulsar wind nebulae.

Column 4 illustrates that 22 of the 46 pulsars were EGRET sources, though most were not seen as pulsars by EGRET, but instead were unidentified sources in the EGRET catalogs. A number of these unidentified EGRET sources had previously been associated with SNR, PWNe, or other objects (e.g. Walker et al. 2003; De Becker et al. 2005). In all cases, the gamma-ray emission seen with the LAT is dominated by the pulsed emission. Of the 22 EGRET sources, 10 are blind search pulsars and 2 are millisecond pulsars. All 6 high-confidence EGRET pulsars are detected and the 3 marginal EGRET detections are confirmed as pulsars. An additional 15 previously detected radio pulsars have been confirmed as pulsed gamma-ray sources.

Not surprisingly, many of the young pulsars have SNR or PWN associations. At least 19 of the 38 non-millisecond pulsars are associated with a PWN and/or SNR (Roberts et al. 2005; Green 2009). A key test of whether any of these associations include any gamma-ray component other than the pulsar will depend on seeing spatially-extended emission or off-pulse emission with a different energy spectrum from that produced by the pulsar.

At least 12 of the 38 non-millisecond pulsars are associated with TeV sources (e.g. Abdo et al. 2009u; Aharonian et al. 2006a,b, and others), most of which (9 of 12) are also associated with pulsar wind nebulae. Those pulsars with both TeV and PWN associations are typically young, with ages less than 20 kyr.

4. Pulsar flux sensitivity

In order to interpret the population of gamma-ray pulsars discovered with the LAT, we needed to evaluate the sensitivity of our searches for pulsed emission. While the precise sensitivity at any location is a function of the local background flux, the pulsar spectrum, and the pulse shape, we can derive an approximate pulsed sensitivity by calculating the *unpulsed* flux sensitivity for a typical pulsar spectrum at all locations in the sky and correlating with the observed Z_2^2 test statistic for the ensemble of detected pulsars.

Figures 5 and 6 show the distributions of the cutoff energy and the spectral index, respectively, for all the LAT-detected pulsars. The distribution of spectral indices peaks in the range $\Gamma = 1 - 2$, and the distribution of cutoffs peaks at $E_c = 1 - 3$ GeV. For a typical spectrum, we used $\Gamma = 1.4$ and $E_c = 2.2$ GeV, values approximately equal to their respective weighted averages.

We then generated a sensitivity map for unpulsed emission for the six-month data set used here. For each *(l,b)* location in the sky, we computed the DC flux sensitivity at a likelihood test statistic TS = 25 threshold integrated above 100 MeV, assuming the typical pulsar spectrum and a diffuse gamma-ray flux under the source PSF from the `rings_Galaxy_v0.fits` model (Abdo et al. 2009e). We note that the likelihood calculation assumes that the source flux is small compared to the diffuse background flux within the PSF, which is appropriate for a source just at the detection limit. Finally, we converted this map to pulsed sensitivity by a simple scale factor that accounts for the correspondence between the Z_2^2 periodicity test confidence level and the unpulsed likelihood TS for the detected pulsars.

The resulting 5σ sensitivity map for pulsed emission is shown in Figure 10. Comparing the measured fluxes with the predicted sensitivities at the pulsar locations (Figure 11), we see that this 5σ limit indeed provides a reasonable lower envelope to the pulsed detections in this catalog. Thus the effective sensitivity for high latitude (e.g. millisecond) pulsars with known rotation ephemerides is $1 - 2 \times 10^{-8}$ cm^{-2} s^{-1}; at low latitude there is large variation, with typical detection thresholds $3 - 5\times$ higher. We expect the threshold to be somewhat higher for pulsars found in blind period searches. Figure 11 suggests that this threshold is $2 - 3\times$ higher than that for pulsars discovered in folding searches, with resulting values as high as 2×10^{-7} cm^{-2} s^{-1}s on the Galactic plane.

The LogN-LogS plot is shown in Figure 12. The dashed line is for all the detected pulsars, the radio-selected gamma-ray pulsars (including millisecond pulsars) are colored gray, and the blue histogram is for the gamma-selected pulsars. This confirms that while radio-selected pulsars are detected down to a threshold of 2×10^{-8} cm^{-2} s^{-1}, the faintest gamma-selected pulsar detected has a flux $\sim 3\times$ higher at 6×10^{-8} cm^{-2} s^{-1}. It is interesting to note that, aside from the lower flux threshold for the former, the radio- and gamma- selected histograms are well matched, suggesting similar underlying populations.

5. Discussion

The striking results of the early *Fermi* pulsar discoveries demonstrate the LAT's excellent power for pulsed gamma-ray detection. By increasing the gamma-ray pulsar sample size by an order of magnitude and by firmly establishing the gamma-selected (radio-faint Geminga-type) and millisecond gamma-ray pulsar populations, we have promoted GeV pulsar astronomy to a major probe of the energetic pulsar population and its magnetospheric physics. Our large pulsar sample allows us both to establish patterns in the pulse emission that point to a common origin of pulsar gamma-rays and to find anomalous systems that may point to exceptional pulsar geometries and/or unusual emission physics. In this section we discuss some initial conclusions drawn from the sample, recognizing that the full exploitation of these new results will flow from the detailed population and emission physics studies to follow.

5.1. Pulsar Detectability

One of the best predictors of gamma-ray pulsar detectability is the spindown flux at Earth $\dot{E}/d^2$. However, as argued by Arons (2006) (see also Harding & Muslimov 2002), it is natural in many models for the gamma-ray emitting gap to maintain a fixed voltage drop. This implies that L_γ is simply proportional to the particle current (Harding 1981), which gives $L_\gamma \propto \dot{E}^{1/2}$, i.e. gamma-ray efficiency increases with decreasing spin-down power down to $\dot{E} \sim 10^{34} - 10^{35}$ erg s^{-1} where the gap saturates at large efficiency. In Figure 8 we plot our present best estimate of the gamma-ray luminosity against $\dot{E}$, based on the pulsed flux measured for each pulsar. Two important caveats must be emphasized here. First, the inferred fluxes are quadratically sensitive to the often large distance uncertainties. Indeed, for many radio selected pulsars (green points) we have only DM-based distance estimates. For many gamma-selected pulsars we have only rather tenuous SNR or birth cluster associations with rough distance bounds. Only a handful of pulsars have secure parallax-based distances. Second, we have assumed here uniform phase-averaged beaming across the sky (f_Ω=1). This is not realized for many emission models, especially for low $\dot{E}$ pulsars (Watters et al. 2009).

To guide the eye, Figure 8 shows lines for 100% conversion efficiency ($L_\gamma = \dot{E}$) and a heuristic constant voltage line $L_\gamma = (10^{33}$ erg s$^{-1}\dot{E})^{1/2}$. In view of the large luminosity uncertainties, we must conclude that it is not yet possible to test the details of the luminosity evolution. However, some trends are apparent and individual objects highlight possible complicating factors. For the highest $\dot{E}$ pulsars, there does seem to be rough agreement with the $\dot{E}^{1/2}$ trend. However, large variance between different distance estimates for the Vela-like PSR J2021+3651 and PSR B1706−44 complicate the interpretation. In the range 10^{35} erg s^{-1} $< \dot{E} < 10^{36.5}$ erg s^{-1}, the L_γ seems nearly constant, although the lack of precise distance measurements limits our ability to draw conclusions. For example the very large nominal DM distance of PSR J0248+6021 would require $> 100\%$ efficiency, and so is unlikely to be correct. The association distances for the gamma-selected pulsars must additionally be treated with caution. For example PSR J2021+4026 has a $\tau_c \sim 10\times$ larger than the age of the putative associated SNR γ Cygni. Improved distance estimates in this range are the key to probing luminosity evolution.

From 10^{34} erg s$^{-1} < \dot{E} < 10^{35}$ erg s^{-1} we have several nearby pulsars with reasonably accurate parallax distance estimates. However we see a wide range of gamma-ray efficiencies. This is the range over which gap saturation is expected to occur in both slot gap and outer gap models. In slot gap models (Harding & Muslimov 2002) (check this reference), the break occurs at about 10^{35} erg s^{-1}, the saturation of the gap at the limit for screening of the accelerating field by pairs, and the efficiency below saturation is predicted to $\sim 10\%$. In outer gap models (Zhang et al. 2004), the break is predicted to occur at somewhat lower $\dot{E} \sim 10^{34}$ erg s^{-1}. With the present statistics and uncertainties, it is not possible to discriminate between these model predictions except to note that both are consistent with the observed results. In some models the gap saturation dramatically affects the shape of the beam on the sky and accordingly the flux conversion factor f_Ω; for outer gap models Watters et al. (2009) estimate $f_\Omega \sim 0.1 - 0.15$ for Geminga (similar values are obtained for J1836+5925), driving down the rather high inferred luminosity of these pulsars by an order of magnitude. In contrast, another pulsar with an accurate parallax distance, PSR J0659+1414, has an inferred luminosity $30\times$ *lower* than the $\dot{E}^{1/2}$ prediction. Clearly, some parameter in addition to $\dot{E}$ controls the observed L_γ. Finally, for $< 10^{34}$ erg s^{-1} the sample is dominated by the MSPs. These nearby, low luminosity objects clearly lie below the $\dot{E}^{1/2}$ trend, and in fact seem more consistent with $L_\gamma \propto \dot{E}$.

As upper limits on pulsar gamma-ray fluxes improve we should obtain additional constraints on the factors controlling pulsar detectability. For example, PSR J1740+1000 shows $< 1/5$ of the flux expected from the constant voltage line. PSRs J1357-6429 and J1930+1852 also have upper limits below the expected fluxes, although such comparison relies on the rather uncertain distance estimates (here dist1 from the ATNF pulsar catalog, Manchester et al. 2005). There are, in addition, a few detected pulsars significantly below the constant voltage trend, e.g. PSRs J0659+1414 and J0205+6449.

One likely candidate for the additional factor affecting gamma-ray detectability is beaming. For PSR J1930+1852, X-ray torus fitting Ng & Romani (2008) suggest a small viewing angle $|\zeta| \sim 33^\circ$. In outer gap models this makes it highly unlikely that the pulsar will produce strong emission on the Earth line-of-sight. Similarly it has been argued that PSR J0659+1414 has a small viewing angle $\zeta < 20^\circ$ (Everett & Weisberg (2001), but see Weltevrede & Wright (2009) for a discussion of uncertainties). Again, strong emission from above the null charge surface is not expected for this ζ. One possible interpretation is that we are seeing slot gap or even polar cap emission from this pulsar, which is expected at this ζ. The unusual pulse profile and spectrum of this pulsar may allow us to test this idea of alternate emission zones.

In discussing non-detections, we should also note that the only binary pulsar systems reported in this paper are the radio-timed MSPs. In particular, our blind searches are not, as yet, sensitive to pulsars that are undergoing strong acceleration in binary systems. However, we do expect such objects to exist. Population synthesis sums in fact suggest that 20-30% of young pulsars are born while retained in massive star binary systems. A few such systems are known in the radio pulsar sample (e.g. the TeV-detected PSR B1259-63); we expect that with the gamma-ray signal immune to dispersion effects an appreciable number of pulsar massive-star binaries will eventually be discovered. Indeed, it is entirely possible that the bright gamma-ray binaries LSI +61 303 (Abdo et al. 2009n) and LS 5039 (Abdo et al. 2009f) may host pulsed GeV signals that have not yet been found.

5.2. Pulsar Population

With the above caveats about missing binary systems in mind, we can already draw some conclusions about the *single* gamma-ray pulsar population. For example, we have 15 non-millisecond radio-selected pulsars and 17 gamma-ray selected pulsars to the shallower flux limit ($\sim 6 \times 10^{-8}$ cm^{-2} s^{-1}) of the latter. Of course, some gamma-ray selected objects can indeed be detected in the radio (Camilo et al. 2009b). Indeed, the detection of PSR J1741-2054 at $L_{1.4\rm GHz} \approx 0.03$ mJy kpc^2 underlines the fact that the radio emission can be very faint. Deep searches for additional radio counterparts are underway. However, with deep radio observations of several objects (e.g. Geminga, PSR J0007+7303=CTA1, PSR J1836+5925) providing no convincing detections, it is clear that some objects are truly radio faint. The substantial number of radio faint objects suggests that gamma-ray emission has an appreciably larger extent than the radio cones, such as expected in the outer gap and slot-gap/two pole caustic models.

Population synthesis studies for normal (non-millisecond) pulsars predicted that LAT would detect from 40 - 80 radio loud pulsars and comparable numbers of radio quiet pulsars in the first year (Gonthier et al. 2004; Zhang et al. 2007). The ratio of radio-selected to gamma-ray selected gamma-ray pulsars has been noted as a particularly sensitive discriminator of models, since the outer magnetosphere models predict much smaller ratios than polar cap models (Harding et al. 2007). Studies of the millisecond pulsar population (Story et al. 2007) predicted that LAT would detect around 12 radio-selected and 33-40 gamma-ray selected millisecond pulsars in the first year, in rough agreement with the number of radio-selected millisecond pulsars seen to date (searches for gamma-ray selected millisecond pulsars have not yet been conducted). Thus, in the first six months the numbers of LAT pulsar detections are consistent with the predicted range, and the large number of gamma-ray selected pulsars discovered so early in the mission points towards the outer magnetosphere models.

We can in fact use our sample of detected gamma-ray pulsars to estimate the Galactic birthrates. For each object with an available distance estimate, we estimate the maximum distance for detection from $D_{max} = D_{est}(F_\gamma/F_{min})^{1/2}$, where D_{est} comes from Table 1, F_γ from Table 4 and F_{min} from Figure 10. We limit D_{max} to 15 kpc, and compare the enclosed volume to the detectable volume V_{max} in a Galactic disk with radius 10 kpc and thickness 1 kpc. If we assume a blind search threshold 2× higher than that for a folding search at a given sky position, the inferred values of $\langle V/V_{max}\rangle$ are 0.49, 0.59 and 0.55 for the radio-selected young pulsars, millisecond pulsars and gamma-ray selected pulsars, respectively. These are close to the expected value of 0.5; the MSP value is somewhat high as our sample includes three objects detected at $< 5\sigma$. The value for the gamma-selected pulsars is also high but is controlled by the very faint PSR J2021+4127. If we exclude this object from the sample, we get $\langle V/V_{max}\rangle = 0.5$ at an effective threshold of 3× the ephemeris-folding value.

Although we do not attempt a full population synthesis here, our early pulsar sample can give rough estimates for local volume birthrates of 8.4×10^{-5} kpc^{-3} y^{-1} (young radio-selected), 3.7×10^{-5} kpc^{-3} y^{-1} (young gamma-selected, 2× threshold) and 1.7×10^{-8} kpc^{-3} y^{-1} (MSP). Note that only half of the gamma-selected objects had distance estimates. If we assume that the set without distance information has comparable luminosity, the gamma-selected birthrate is thus $\sim 2\times$ larger. Also note that for 3× detection threshold this birthrate increases by an additional $\sim$ 65%. We can extrapolate these birthrates to a full disk with an effective radius of 10 kpc. The result are 1/120y (radio-selected young pulsars), 1/140y to 1/85y (gamma-selected pulsars) and $1/(6 \times 10^5$y) (radio selected MSP). Normally in estimating radio pulsar birthrates one would correct for the radio beaming fraction. However if young gamma-selected pulsars are simply similar objects viewed outside of the radio beam, this would result in double-counting. In any case one infers a total Galactic birthrate for energetic pulsars as $\sim$ 1/65y to 1/50y, with gamma-selected objects representing half or more. This represents a large fraction of estimated Galactic supernova rate, so clearly more careful population synthesis sums will be needed to see if these numbers are compatible.

5.3. Trends in Light Curves and Other Observables

The pulse shape properties can also help us probe the geometry and physics of the emission region. The great majority of the pulsars show two dominant, relatively sharp peaks, suggesting that we are seeing caustics from the edge of a hollow cone. When a single peak is seen, it tends to be broader, suggesting a tangential cut through an emission cone. This picture is realized in the outer gap and the high altitude portion of the slot-gap models.

For the radio-emitting pulsars, we can compare the phase lag between the radio and first gamma-ray peak δ with the separation of the two gamma-ray peaks Δ. As first pointed out in Romani & Yadigaroglu (1995), these should be correlated in outer magnetosphere models – this is indeed seen (Figure 3). The distribution can be compared with predictions of the TPC and OG models shown in Watters et al. (2009). The $\delta - \Delta$ distribution and in particular the presence of $\Delta \sim 0.2 - 0.3$ values appear to favor the OG picture. However, there are a greater number having $\Delta \sim 0.4 - 0.5$, which favors TPC models. A full comparison will require detailed population models, which are being created. It may also be hoped that the precise distribution of measured values can help probe details of the emission geometry. In particular, whenever we have external constraints on the viewing angle ζ (typically from X-ray images of the PWN) or magnetic inclination α (occasionally measured from radio polarization), then the observed values of δ and Δ become a powerful probe of the precise location of the emission sheet within the magnetosphere. This can be sensitive to the field perturbations from magnetospheric currents and hence can probe the global electrodynamics of the pulsar magnetosphere.

The distribution of gamma-ray peak separations for all pulsars, and for the different pulsar types, also shows the preponderance of $\Delta \sim 0.4 - 0.5$, for both radio-selected and gamma-selected pulsars (Figure 7). However, we see that the lower values of peak separation Δ are preferentially found at $\dot{E} < 10^{36}$. The meaning of this trend is not yet clear.

If one examines the energy dependence of the light curves of both the radio-selected and gamma-selected pulsars, a decrease in the P1/P2 ratio with increasing energy seems to be a common feature. However, the P1/P2 ratio evolution does not occur for all pulsars, notably J1028-5820, J2021+3651, J0633+0632, J1124-5916, J1813-1246, J1826-1256, J1836+5925, J2238+59. Most of these pulsars have two peaks with phase separation of ~0.5 and little or no inter-peak emission. Perhaps the lack of P1/P2 energy evolution is connected with an overall symmetry of the light curve.

The LAT pulsar sample also shows evidence of trends in other observables that may offer additional clues to the pulsar physics. While the detected objects have a wide range of surface magnetic fields, their inferred light cylinder magnetic fields $B_{\rm LC}$ are uniformly relatively large ($\gtrsim 10^3$ G). Indeed, the LAT detected MSPs are those with the highest light cylinder fields with values very similar to those of the detected normal pulsars. Comparison of the spectral cut-off E_c with surface magnetic field shows no strong significant correlation. This evidence argues against classical low altitude polar cap models supported by γ-B cascades. However, there is a weak correlation of E_c with $B_{\rm LC}$, as shown in Figure 5. It is interesting that the values of E_c have a range of only about a decade, from 1 to 10 GeV, and all the different types of pulsars seem to follow the same correlation. This strongly implies that the gamma-ray emission originates in similar locations in the magnetosphere relative to the light cylinder. Such a correlation of E_c with $B_{\rm LC}$ is actually expected in all outer magnetosphere models where the gamma-ray emission primarily comes from curvature radiation of electrons whose acceleration is balanced by radiation losses. In this case,

$$E_c = 0.32 \lambda_c \left(\frac{E_\|}{e} \right)^{3/4} \rho_c^{1/2} \tag{10}$$

in mc^2, where λ_c is the electron Compton wavelength, $E_\|$ is the electric field that accelerates particles parallel to the magnetic field and ρ_c is the magnetic field radius of curvature. In both slot gap (Muslimov & Harding 2004) and outer gap (Zhang et al. 2004; Hirotani 2008), $E_\| \propto B_{\rm LC}\, w^2$, where w is the gap width. All these models give values of E_c that are roughly consistent with those measured for the LAT pulsars. Although $\rho_c \sim R_{\rm LC}$, the gap widths are expected to decrease with increasing $B_{\rm LC}$, so that E_c is predicted to be only weakly dependent on $B_{\rm LC}$ in most outer magnetosphere models, as observed.

In Figure 6, we see a general trend for the young pulsars to show a softer spectrum at large $\dot{E}$, although there is a great deal of scatter; a similar trend was noted in (Thompson et al. 1999). This may be indicative of higher pair multiplicity, which would steepen the spectrum for the more energetic pulsars, either by steepening the spectrum of the curvature radiation-generating primary electrons (Romani 1996) or by inclusion of an additional soft spectral component associated with robust pair formation (Harding et al. 2008; Takata & Chang 2007). In either case, one would expect steepening from the simple monoenergetic curvature radiation spectrum $\Gamma = 2/3$ for the higher $\dot{E}$ pulsars. Interestingly, the MSPs do not extend the trend to lower $\dot{E}$. Of course EGRET (and now the LAT) find strong variations of spectral index with phase for the brighter pulsars. A full understanding of spectral index trends will doubtless require phase-resolved modeling.

6. Conclusion

The new gamma-ray pulsar populations established by early LAT observations show that we are detecting many nearby young pulsars. In addition we are detecting the millisecond pulsars with the highest spin-down flux at Earth. Thus we see that the LAT is providing a new, local, but relatively unbiased view of the energetic pulsar population (see Figure 2). These detections provide a new window into pulsar demographics and physics.

We conclude that a large fraction of the local energetic pulsars are GeV emitters. There is also a significant correlation with X-ray and TeV bright pulsar wind nebulae. Conversely, we have now uncovered the pulsar origin of a large fraction of the bright unidentified Galactic EGRET sources, as proposed by several authors (Kaaret & Cottam 1996; Yadigaroglu & Romani 1997). We have also found plausible pulsar counterparts for several previously identified TeV sources. In this sense the 'mystery' of the unidentified EGRET sources is largely solved. It is possible that the two massive binaries (LSI +61 303, LS 5059) and some of the remaining unidentified sources also contain spin-powered pulsars. Thus we expect that the LAT pulsar population will increase, with both the detection of binary gamma-ray pulsars and fainter and more distant pulsars.

The light curve and spectral evidence summarized above suggests that these pulsars have high altitude beams, whose fan-like emission scans over a large portion of the celestial sphere. This means that they should provide an unbiased census of energetic neutron star formation. A rough estimate of the young gamma-ray pulsar birthrate extrapolating from our local sample suggests a Galactic birthrate of 1/50-70y, a large fraction of the estimated Galactic supernova rate. Gamma-ray detectable millisecond pulsars in the Galactic field are born rarely, $\sim 1/6 \times 10^5$y, but with their long lifetimes are inferred to contribute comparably to the number of (in principle) detectable Galactic gamma-ray pulsars.

The data also advance our understanding of emission zone physics. It is now clear that the gamma-ray emission from the brightest pulsars arises largely in the outer magnetosphere. The photon emission also occupies a large fraction of the spin-down luminosity, increasing as the pulsars approach $\dot{E} \sim 10^{33-34}$ erg s^{-1}. While these wide, bright beams are a boon for population studies, as noted above, they represent a challenge for theorists trying to understand pulsar magnetospheres. Further LAT pulsar observations and, in particular, the high quality, highly phase-resolved spectra now being obtained for the brightest LAT pulsars will surely sharpen this challenge.

The *Fermi* LAT Collaboration acknowledges the generous support of a number of agencies and institutes that have supported the Fermi LAT Collaboration. These include the National Aeronautics and Space Administration and the Department of Energy in the United States, the Commissariat à l'Energie Atomique and the Centre National de la Recherche Scientifique / Institut National de Physique Nucléaire et de Physique des Particules in France, the Agenzia Spaziale Italiana and the Istituto Nazionale di Fisica Nucleare in Italy, the Ministry of Education, Culture, Sports, Science and Technology (MEXT), High Energy Accelerator Research Organization (KEK) and Japan Aerospace Exploration Agency (JAXA) in Japan, and the K. A. Wallenberg Foundation and the Swedish National Space Board in Sweden.

The Parkes radio telescope is part of the Australia Telescope which is funded by the Commonwealth Government for operation as a National Facility managed by CSIRO. The Green Bank Telescope is operated by the National Radio Astronomy Observatory, a facility of the National Science Foundation operated under cooperative agreement by Associated Universities, Inc. The Arecibo Observatory is part of the National Astronomy and Ionosphere Center (NAIC), a national research center operated by Cornell University under a cooperative agreement with the National Science Foundation. The Nançay Radio Observatory is operated by the Paris Observatory, associated with the French Centre National de la Recherche Scientifique (CNRS). The Lovell Telescope is owned and operated by the University of Manchester as part of the Jodrell Bank Centre for Astrophysics with support from the Science and Technology Facilities Council of the United Kingdom. The Westerbork Synthesis Radio Telescope is operated by Netherlands Foundation for Radio Astronomy, ASTRON.

REFERENCES

Abdo, A. A. et al. 2009a, ApJ, 699, L102

—. 2008, Science, 322, 1218

—. 2009b, ApJ, in prep - *Fermi* LAT Observations of the Geminga Pulsar

—. 2009c, ApJ, in prep - *Fermi* LAT Observations of Cygnus X-3

—. 2009d, ApJ, submitted - *Fermi* LAT Observations of the Crab

—. 2009e, ApJ, in prep - *Fermi* LAT detection of pulsed gamma-rays from the Vela-like pulsars PSR J1048−5832 and PSR J2229+6114

—. 2009f, ApJ, in prep - *Fermi* LAT Observations of LS5039

—. 2009g, ApJ, in prep - The *Fermi* LAT View of Three EGRET Pulsars

—. 2009h, ApJ, in prep - PSR J1907+0602 powering a bright TeV PWN

—. 2009i, ApJ, in prep - *Fermi* LAT PSR J2021+4026 near the gamma Cygni SNR

—. 2009j, ApJ, in prep - *Fermi* LAT PSR J2032+4127 near Cygnus OB2

—. 2009k, Science, in press (10.1126/science.1176113)

—. 2009l, ApJ, 695, L72

—. 2009m, ApJ, 696, 1084

—. 2009n, ArXiv e-prints, (arXiv:0907.4307)

—. 2009o, ApJS, 183, 46

—. 2009p, Physical Review Letters, 102, 181101

—. 2009q, ApJ, 700, 1059

—. 2009r, ApJ, in press - Pulsed Gamma-rays from the millisecond pulsar J0030+0451 with the Fermi Large Area Telescope, arXiv:0904.4377

—. 2009s, Science, in press (10.1126/science.1175558)

—. 2009t, ArXiv e-prints

—. 2009u, ApJ, 700, L127

Aharonian, F. et al. 2009, A&A, 499, 723

—. 2007, A&A, 472, 489

—. 2006a, A&A, 457, 899

—. 2006b, A&A, 448, L43

—. 2006c, A&A, 456, 245

Arons, J. 1993, ApJ, 408, 160

—. 2006, On the Present and Future of Pulsar Astronomy, 26th meeting of the IAU, Joint Discussion 2, 16-17 August, 2006, Prague, Czech Republic, JD02, #39, 2

Atwood, W. B. et al. 2009, ApJ, 697, 1071

Atwood, W. B., Ziegler, M., Johnson, R. P., & Baughman, B. M. 2006, ApJ, 652, L49

Bassa, C. G., van Kerkwijk, M. H., & Kulkarni, S. R. 2003, A&A, 403, 1067

Brisken, W. F., Fruchter, A. S., Goss, W. M., Herrnstein, R. M., & Thorsett, S. E. 2003, AJ, 126, 3090

Browning, R., Ramsden, D., & Wright, P. J. 1971, Nature, 232, 99

Buccheri, R. et al. 1983, A&A, 128, 245

Camilo, F. et al. 2009a, ApJ, in prep - Pulsed Gamma-rays from the Young Pulsars PSR J1833−1034 and PSR J1747−2958

Camilo, F., Manchester, R. N., Gaensler, B. M., & Lorimer, D. R. 2002a, ApJ, 579, L25

Camilo, F., Manchester, R. N., Gaensler, B. M., Lorimer, D. R., & Sarkissian, J. 2002b, ApJ, 567, L71

Camilo, F., Ransom, S. M., Gaensler, B. M., Slane, P. O., Lorimer, D. R., Reynolds, J., Manchester, R. N., & Murray, S. S. 2006, ApJ, 637, 456

Camilo, F. et al. 2009b, ApJ, submitted - Radio detection of two gamma-ray pulsars

—. 2002c, ApJ, 571, L41

Caswell, J. L., & Haynes, R. F. 1987, A&A, 171, 261

Caswell, J. L., Murray, J. D., Roger, R. S., Cole, D. J., & Cooke, D. J. 1975, A&A, 45, 239

Chandler, A. M., Koh, D. T., Lamb, R. C., Macomb, D. J., Mattox, J. R., Prince, T. A., & Ray, P. S. 2001, ApJ, 556, 59

Cheng, K. S., & Zhang, L. 1998, ApJ, 498, 327

Cognard I. et al, a. 2009, A&A, in prep - PSRJ0248+6021, a young pulsar in the northern Galactic plane

Cordes, J. M., & Lazio, T. J. W. 2002, ArXiv e-prints, (arXiv:astro-ph/0207156)

Crawford, F., Roberts, M. S. E., Hessels, J. W. T., Ransom, S. M., Livingstone, M., Tam, C. R., & Kaspi, V. M. 2006, ApJ, 652, 1499

D'Agostini, G. 1995, Nuclear Instruments and Methods in Physics Research A, 362, 487

D'Amico, N. et al. 2001, ApJ, 552, L45

De Becker, M., Rauw, G., & Swings, J.-P. 2005, Ap&SS, 297, 291 de Jager, O. C., Raubenheimer, B. C., & Swanepoel, J. W. H. 1989, A&A, 221, 180

Deller, A. T., Verbiest, J. P. W., Tingay, S. J., & Bailes, M. 2008, ApJ, 685, L67

Dodson, R., Legge, D., Reynolds, J. E., & McCulloch, P. M. 2003, ApJ, 596, 1137

Dowd, A., Sisk, W., & Hagen, J. 2000, in Astronomical Society of the Pacific Conference Series, Vol. 202, IAU Colloq. 177: Pulsar Astronomy - 2000 and Beyond, ed. M. Kramer, N. Wex, & R. Wielebinski, 275–+

Edwards, R. T., Hobbs, G. B., & Manchester, R. N. 2006, MNRAS, 372, 1549

Everett, J. E., & Weisberg, J. M. 2001, ApJ, 553, 341

Faherty, J., Walter, F. M., & Anderson, J. 2007, Ap&SS, 308, 225

Fesen, R., Rudie, G., Hurford, A., & Soto, A. 2008, ApJS, 174, 379

Fesen, R. A., Kirshner, R. P., & Becker, R. H. 1988, in IAU Colloq. 101: Supernova Remnants and the Interstellar Medium, ed. R. S. Roger & T. L. Landecker, 55–+

Fierro, J. M. et al. 1995, ApJ, 447, 807

Gaensler, B. M., van der Swaluw, E., Camilo, F., Kaspi, V. M., Baganoff, F. K., Yusef-Zadeh, F., & Manchester, R. N. 2004, ApJ, 616, 383

Gaensler, B. M., & Wallace, B. J. 2003, ApJ, 594, 326

Gold, T. 1968, Nature, 218, 731

Gonthier, P. L., Ouellette, M. S., Berrier, J., O'Brien, S., & Harding, A. K. 2002, ApJ, 565, 482

Gonthier, P. L., Van Guilder, R., & Harding, A. K. 2004, ApJ, 604, 775

Gonzalez, M., & Safi-Harb, S. 2003, ApJ, 583, L91

Gotthelf, E. V. 2003, ApJ, 591, 361

Green, D. A. 2009, Bulletin of the Astronomical Society of India, 37, 45

Green, D. A., & Gull, S. F. 1982, Nature, 299, 606

Greidanus, H., & Strom, R. G. 1990, A&A, 240, 376

H. E. S. S. Collaboration: A. Djannati-Atai, De Jager, O. C., Terrier, R., Gallant, Y. A., & Hoppe, S. 2007, ArXiv e-prints, (arXiv:0710.2247)

Halpern, J. P. et al. 2008, ApJ, 688, L33

Halpern, J. P., Camilo, F., & Gotthelf, E. V. 2007, ApJ, 668, 1154

Halpern, J. P., Camilo, F., Gotthelf, E. V., Helfand, D. J., Kramer, M., Lyne, A. G., Leighly, K. M., & Eracleous, M. 2001a, ApJ, 552, L125

Halpern, J. P., Gotthelf, E. V., Camilo, F., Helfand, D. J., & Ransom, S. M. 2004, ApJ, 612, 398

Halpern, J. P., Gotthelf, E. V., Leighly, K. M., & Helfand, D. J. 2001b, ApJ, 547, 323

Harding, A. K. 1981, ApJ, 245, 267

Harding, A. K., Grenier, I. A., & Gonthier, P. L. 2007, Ap&SS, 309, 221

Harding, A. K., & Muslimov, A. G. 2002, ApJ, 568, 862

Harding, A. K., Stern, J. V., Dyks, J., & Frackowiak, M. 2008, ApJ, 680, 1378

Hartman, R. C. et al. 1999, ApJS, 123, 79

Hewish, A., Bell, S. J., Pilkington, J. D. H., Scott, P. F., & Collins, R. A. 1968, Nature, 217, 709

Hirotani, K. 2008, ApJ, 688, L25

Hobbs, G., Edwards, R., & Manchester, R. 2006, Chinese Journal of Astronomy and Astrophysics Supplement, 6, 020000

Hobbs, G. B., Lyne, A. G., Kramer, M., Martin, C. E., & Jordan, C. 2004, MNRAS, 353, 1311

Hoppe, S., de Oña-Wilhemi, E., Khélifi, B., Chaves, R. C. G., de Jager, O. C., Stegmann, C., Terrier, R., & for the H. E. S. S. Collaboration. 2009, ArXiv e-prints, (arXiv:0906.5574)

Hotan, A. W., Bailes, M., & Ord, S. M. 2006, MNRAS, 369, 1502

Hui, C. Y., & Becker, W. 2007, A&A, 470, 965

Jackson, M. S., & Halpern, J. P. 2005, ApJ, 633, 1114

Johnston, S., Manchester, R. N., Lyne, A. G., D'Amico, N., Bailes, M., Gaensler, B. M., & Nicastro, L. 1996, MNRAS, 279, 1026

Kaaret, P., & Cottam, J. 1996, ApJ, 462, L35+

Kanbach, G. et al. 1980, A&A, 90, 163

Kaplan, D. L., Chatterjee, S., Gaensler, B. M., & Anderson, J. 2008, ApJ, 677, 1201

Kaplan, D. L. et al. 2005, PASP, 117, 643

Keith, M. J., Johnston, S., Kramer, M., Weltevrede, P., Watters, K. P., & Stappers, B. W. 2008, MNRAS, 389, 1881

Kniffen, D. A., Hartman, R. C., Thompson, D. J., Bignami, G. F., & Fichtel, C. E. 1974, Nature, 251, 397

Koribalski, B., Johnston, S., Weisberg, J. M., & Wilson, W. 1995, ApJ, 441, 756

Kothes, R., Uyaniker, B., & Pineault, S. 2001, ApJ, 560, 236

Kramer, M. et al. 2003, VizieR Online Data Catalog, 834, 21299

Kuiper, L., Hermsen, W., Cusumano, G., Diehl, R., Schönfelder, V., Strong, A., Bennett, K., & McConnell, M. L. 2001, A&A, 378, 918

Kuiper, L., Hermsen, W., Verbunt, F., Thompson, D. J., Stairs, I. H., Lyne, A. G., Strickman, M. S., & Cusumano, G. 2000, A&A, 359, 615

Landecker, T. L., Roger, R. S., & Higgs, L. A. 1980, A&AS, 39, 133

Lommen, A. N., Kipphorn, R. A., Nice, D. J., Splaver, E. M., Stairs, I. H., & Backer, D. C. 2006, ApJ, 642, 1012

Malofeev, V. M., Malov, I. F., Malov, O. I., & Glushak, A. P. 2003, Astronomy Reports, 47, 413

Manchester, R. N. 2008, in American Institute of Physics Conference Series, Vol. 983, 40 Years of Pulsars: Millisecond Pulsars, Magnetars and More, ed. C. Bassa, Z. Wang, A. Cumming, & V. M. Kaspi, 584–592

Manchester, R. N., Hobbs, G. B., Teoh, A., & Hobbs, M. 2005, AJ, 129, 1993

Manchester, R. N. et al. 2001, MNRAS, 328, 17

Mazziotta, M. N. 2009, ArXiv e-prints, (arXiv:0907.0638)

McGowan, K. E., Zane, S., Cropper, M., Kennea, J. A., Córdova, F. A., Ho, C., Sasseen, T., & Vestrand, W. T. 2004, ApJ, 600, 343

McLaughlin, M. A., & Cordes, J. M. 2000, ApJ, 538, 818

Muslimov, A. G., & Harding, A. K. 2004, ApJ, 606, 1143

Navarro, J., de Bruyn, A. G., Frail, D. A., Kulkarni, S. R., & Lyne, A. G. 1995, ApJ, 455, L55+

Ng, C.-Y., Roberts, M. S. E., & Romani, R. W. 2005, ApJ, 627, 904

Ng, C.-Y., & Romani, R. W. 2008, ApJ, 673, 411

Nice, D. J., Splaver, E. M., Stairs, I. H., Löhmer, O., Jessner, A., Kramer, M., & Cordes, J. M. 2005, ApJ, 634, 1242

Noutsos, A. et al. 2009, ApJ, in prep - *Fermi* LAT Observations of the pulsar J2043+2740

Oka, T., Kawai, N., Naito, T., Horiuchi, T., Namiki, M., Saito, Y., Romani, R. W., & Kifune, T. 1999, ApJ, 526, 764

Pacini, F. 1968, Nature, 219, 145

Pineault, S., Landecker, T. L., Madore, B., & Gaumont-Guay, S. 1993, AJ, 105, 1060

Possenti, A., Cerutti, R., Colpi, M., & Mereghetti, S. 2002, A&A, 387, 993

Ray, P. S., Thorsett, S. E., Jenet, F. A., van Kerkwijk, M. H., Kulkarni, S. R., Prince, T. A., Sandhu, J. S., & Nice, D. J. 1996, ApJ, 470, 1103

Ray, P. S., et al. 2009, ApJ, in prep - Precise Timing of Fermi Gamma-Ray Pulsars

Roberts, D. A., Goss, W. M., Kalberla, P. M. W., Herbstmeier, U., & Schwarz, U. J. 1993, A&A, 274, 427

Roberts, M. S. E., Brogan, C. L., Gaensler, B. M., Hessels, J. W. T., Ng, C.-Y., & Romani, R. W. 2005, Ap&SS, 297, 93

Roberts, M. S. E., Hessels, J. W. T., Ransom, S. M., Kaspi, V. M., Freire, P. C. C., Crawford, F., & Lorimer, D. R. 2002, ApJ, 577, L19

Romani, R. W. 1996, ApJ, 470, 469

Romani, R. W., Ng, C.-Y., Dodson, R., & Brisken, W. 2005, ApJ, 631, 480

Romani, R. W., & Yadigaroglu, I.-A. 1995, ApJ, 438, 314

Romero, G. E., Benaglia, P., & Torres, D. F. 1999, A&A, 348, 868

Schlegel, D. J., Finkbeiner, D. P., & Davis, M. 1998, ApJ, 500, 525

Shklovskii, I. S. 1970, Soviet Astronomy, 13, 562

Smith, D. A. et al. 2008, A&A, 492, 923

Story, S. A., Gonthier, P. L., & Harding, A. K. 2007, ApJ, 671, 713

Strom, R. G., & Stappers, B. W. 2000, in Astronomical Society of the Pacific Conference Series, Vol. 202, IAU Colloq. 177: Pulsar Astronomy - 2000 and Beyond, ed. M. Kramer, N. Wex, & R. Wielebinski, 509–+

Takata, J., & Chang, H.-K. 2007, ApJ, 670, 677

Taylor, J. H. 1992, Royal Society of London Philosophical Transactions Series A, 341, 117

Taylor, J. H., & Cordes, J. M. 1993, ApJ, 411, 674

Theureau, G. et al. 2005, A&A, 430, 373

Thompson, D. J. 2004, in Astrophysics and Space Science Library, Vol. 304, Cosmic Gamma-Ray Sources, ed. K. S. Cheng & G. E. Romero, 149–+

Thompson, D. J. et al. 1994, ApJ, 436, 229

—. 1999, ApJ, 516, 297

Thompson, D. J., Fichtel, C. E., Kniffen, D. A., & Ogelman, H. B. 1975, ApJ, 200, L79

Toscano, M., Britton, M. C., Manchester, R. N., Bailes, M., Sandhu, J. S., Kulkarni, S. R., & Anderson, S. B. 1999, ApJ, 523, L171

Trimble, V. 1973, PASP, 85, 579

Uchida, K., Morris, M., & Yusef-Zadeh, F. 1992, AJ, 104, 1533

Van Etten, A., Romani, R. W., & Ng, C.-Y. 2008, ApJ, 680, 1417

Voûte, J. L. L., Kouwenhoven, M. L. A., van Haren, P. C., Langerak, J. J., Stappers, B. W., Driesens, D., Ramachandran, R., & Beijaard, T. D. 2002, A&A, 385, 733

Walker, M., Mori, M., & Ohishi, M. 2003, ApJ, 589, 810

Watters, K. P., Romani, R. W., Weltevrede, P., & Johnston, S. 2009, ApJ, 695, 1289

Weltevrede, P. et al. 2009a, ApJ, in prep - A study of six moderately energetic gamma-ray pulsars using the *Fermi* LAT

Weltevrede, P., Johnston, S., et al. 2009b, PASA, submitted

Weltevrede, P., & Wright, G. 2009, MNRAS, 395, 2117

Yadigaroglu, I.-A., & Romani, R. W. 1997, ApJ, 476, 347

Zepka, A., Cordes, J. M., Wasserman, I., & Lundgren, S. C. 1996, ApJ, 456, 305

Zhang, L., Cheng, K. S., Jiang, Z. J., & Leung, P. 2004, ApJ, 604, 317

Zhang, L., Fang, J., & Chen, S. B. 2007, ApJ, 666, 1165

Ziegler, M., Baughman, B. M., Johnson, R. P., & Atwood, W. B. 2008, ApJ, 680, 620

Table 1. Pulsar Distances

Pulsar Name	Distance (kpc)	Method*	(Ref+)
J0007+7303	1.4±0.3	K	(30)
J0030+0451	0.300±0.090	P	(24)
J0205+6449	2.6–3.2	K	(13,32)
J0218+4232	2.5–4	O	(1)
J0248+6021	2–9	O	(6)
J0437−4715	0.1563±0.0013	P	(9)
J0534+2200	2.0±0.5	O	(34)
J0613−0200	$0.48^{+0.19}_{-0.11}$	P	(17)
J0631+1036	0.75–3.62	O	(38)
J0633+1746	$0.250^{+0.120}_{-0.062}$	P	(11)
J0659+1414	$0.288^{+0.033}_{-0.027}$	P	(2)
J0742−2822	$2.07^{+1.38}_{-1.07}$	DM	(20)
J0751+1807	$0.6^{+0.6}_{-0.2}$	P	(28)
J0835−4510	$0.287^{+0.019}_{-0.017}$	P	(10)
J1028−5819	2.33±0.70	DM	(19)
J1048−5832	2.71±0.81	DM	(22)
J1057−5226	0.72 ±0.2	DM	(36)
J1124−5916	$4.8^{+0.7}_{-1.2}$	O	(12)
J1418−6058	2–5	O	(27,37)
J1420−6048	5.6±1.7	DM	(8)
J1509−5850	2.6±0.8	DM	(18)
J1614−2230	1.27±0.39	DM	(7)
J1709−4429	1.4–3.6	O	(26,20)
J1718−3825	3.82±1.15	DM	(25)
J1741−2054	0.38±0.11	DM	(3)
J1744−1134	$0.357^{+0.043}_{-0.035}$	P	(33)
J1747−2958	2.0±0.6	DM	(5)
J1809−2332	1.7±1.0	K	(29)
J1833−1034	4.7±0.4	K	(4)
J1836+5925	<0.8	O	(15)
J1952+3252	2.0±0.5	K	(14)
J2021+3651	$2.1^{+2.1}_{-1.0}$	O	(35)
J2021+4026	1.5±0.45	K	(23)
J2032+4127	3.6±1.08	DM	(3)
J2043+2740	1.80±0.54	DM	(31)
J2124−3358	$0.25^{+0.25}_{-0.08}$	P	(17)
J2229+6114	0.8–6.5	O	(21,16)

*K distance evaluation from kinematic model; P from parallax; DM from dispersion measure using the Cordes & Lazio (2002) model; O from other measurements.

+For DM, the reference gives the DM measurement.

References. — (1) Bassa et al. (2003); (2) Brisken et al. (2003); (3) Camilo et al. (2009b); (4) Camilo et al. (2006); (5) Camilo et al. (2002a); (6) Cognard I. et al (2009); (7) Crawford et al. (2006); (8) D'Amico et al. (2001) (9) Deller et al. (2008); (10) Dodson et al. (2003); (11) Faherty et al. (2007); (12) Gonzalez & Safi-Harb (2003); (13) Green & Gull (1982); (14) Greidanus & Strom (1990); (15) Halpern et al. (2007); (16) Halpern et al. (2001a); (17) Hotan et al. (2006); (18) Hui & Becker (2007); (19) Keith et al. (2008); (20) Koribalski et al. (1995); (21) Kothes et al. (2001) (22) Johnston et al. (1996); (23) Landecker et al. (1980); (24) Lommen et al. (2006); (25) Manchester et al. (2001); (26) McGowan et al. (2004); (27) Ng et al. (2005); (28) Nice et al. (2005); (29) Oka et al. (1999); (30) Pineault et al. (1993); (31) Ray et al. (1996); (32) Roberts et al. (1993); (33) Toscano et al. (1999); (34) Trimble (1973); (35) Van Etten et al. (2008); (36) Weltevrede & Wright (2009); (37) Yadigaroglu & Romani (1997); (38) Zepka et al. (1996)

Table 2. Characteristic parameters.

PSR	Type, *Ref.*	l (°)	b (°)	P (ms)	$\dot{\rm P}$ (10^{-15})	age τ (kyr)	$\dot{\rm E}$ 10^{34} erg s^{-1}	B$_{LC}$ (kG)	S_{1400} (mJy)
J0007+7303	g [a,b]	119.7	10.5	316	361	13.9	45.2	3.1	[1] < 0.1
J0030+0451	m [c,d]	113.1	-57.6	4.87	1.0×10^{-5}	7.7×10^{6}	0.34	17.8	0.60
J0205+6449	r [e]	130.7	3.1	65.7	194	5.37	2700	115.9	0.04
J0218+4232	mb [d]	139.5	-17.5	2.32	7.7×10^{-5}	4.8×10^{5}	24	313.1	0.90
J0248+6021	r [f]	137.0	0.4	217	55.1	63.1	21	3.1	9
J0357+32	g [b]	162.7	-16.0	444	12.0	585.0	0.5	0.2	*
J0437−4715	mb [d]	253.4	-42.0	5.76	1.4×10^{-5}	6.6×10^{6}	0.29	13.7	142
J0534+2200	r [h]	184.6	-5.8	33.1	423	1.24	46100	950.0	14.0
J0613−0200	mb [d]	210.4	-9.3	3.06	9×10^{-6}	5.3×10^{6}	1.3	54.3	1.40
J0631+1036	r [i]	201.2	0.5	288	105	43.6	17.3	2.1	0.80
J0633+06	g [b]	205.0	-1.0	297	79.5	59.3	11.9	1.7	[2] < 0.2
J0633+1746	g [h]	195.1	4.3	237	11.0	342	3.25	1.1	< 1
J0659+1414	r [i]	201.1	8.3	385	55.0	111	3.81	0.7	3.70
J0742−2822	r [i]	243.8	-2.4	167	16.8	157	14.3	3.3	15.0
J0751+1807	mb [d]	202.7	21.1	3.48	6.2×10^{-6}	8.0×10^{6}	0.6	32.3	3.20
J0835−4510	r [k]	263.6	-2.8	89.3	124	11.3	688	43.4	1100
J1028−5819	r [l]	285.1	-0.5	91.4	16.1	90	83.2	14.6	0.36
J1048−5832	r [m]	287.4	0.6	124	96.3	20.3	201	16.8	6.50
J1057−5226	r [n]	286.0	6.6	197	5.83	535	3.01	1.3	11
J1124−5916	r	292.0	1.8	135	747	2.87	1190	37.3	0.08
J1418−6058	g [b]	313.3	0.1	111	170	10.3	495.2	29.4	[2,3] < 0.06
J1420−6048	r [i]	313.5	0.2	68.2	83.2	13.4	1000	69.1	0.90
J1459−60	g [b]	317.9	-1.8	103	25.5	64.0	91.9	13.6	[2] < 0.2
J1509−5850	r [i]	320.0	-0.6	88.9	9.17	154	51.5	11.8	0.15
J1614−2230	mb [d]	352.5	20.3	3.15	4×10^{-6}	1.2×10^{6}	0.5	33.7	*
J1709−4429	r [n]	343.1	-2.7	102	93.0	17.5	341	26.4	7.30
J1718−3825	r [i]	349.0	-0.4	74.7	13.2	89.5	125	21.9	1.30
J1732−31	g [b]	356.2	0.9	197	26.1	120.0	13.6	2.7	[2] < 0.2
J1741−2054	g [b]	6.4	4.6	414	16.9	392.1	0.9	0.3	0.16
J1744−1134	m [d]	14.8	9.2	4.08	7×10^{-6}	9×10^{6}	0.4	24.0	3.00
J1747−2958	r [o]	359.3	-0.8	98.8	61.3	25.5	251	23.5	0.25
J1809−2332	g [b]	7.4	-2.0	147	34.4	67.6	43.0	6.5	[2,3] < 0.06
J1813−1246	g [b]	17.2	2.4	48.1	17.6	43.3	625.7	76.2	[2] < 0.2
J1826−1256	g [b]	18.5	-0.4	110	121	14.4	358.2	25.2	[2,3] < 0.06
J1833−1034	r [o]	21.5	-0.9	61.9	202	4.85	3370	137.3	0.07
J1836+5925	g [b]	88.9	25.0	173	1.53	1800.0	1.2	0.9	[4] < 0.007
J1907+06	g [b,r]	40.2	-0.9	107	87.3	19.4	284.4	23.2	< 0.02
J1952+3252	r [n]	68.8	2.8	39.5	5.84	107	374	71.6	1.00
J1958+2846	g [b]	65.9	-0.2	290	222	20.7	35.8	3.0	*
J2021+3651	r [p]	75.2	0.1	104	95.6	17.2	338	26.0	0.10
J2021+4026	g [b,s]	78.2	2.1	265	54.8	76.8	11.6	1.9	*
J2032+4127	g [b,t]	80.2	1.0	143	19.6	115.8	26.3	5.3	[5] 0.12
J2043+2740	r [q]	70.6	-9.2	96.1	1.27	1200	5.64	3.6	[6] 7
J2124−3358	m [d]	10.9	-45.4	4.93	1.2×10^{-5}	6×10^{5}	0.4	18.8	1.60
J2229+6114	r [m]	106.6	2.9	51.6	78.3	10.5	2250	134.5	0.25
J2238+59	g [b]	106.5	0.5	163	98.6	26.3	90.3	8.6	*

The types are gamma-selected (g), millisecond (m), binary (b), and radio-selected (r). References to *Fermi* LAT publications specific to these pulsars: a (Abdo et al. 2008) ; b (Abdo et al. 2009s) ; c (Abdo et al. 2009r) ; d (Abdo et al. 2009k) ; e (Abdo et al. 2009a) ; f (Cognard I. et al 2009) ; h (Abdo et al. 2009d) ; i (Weltevrede et al. 2009a) ; j (Abdo et al. 2009b) ; k (Abdo et al. 2009m) ; l (Abdo et al. 2009l) ; m (Abdo et al. 2009e) ; n (Abdo et al. 2009g) ; o (Camilo et al. 2009a) ; p (Abdo et al. 2009q) ; q (Noutsos et al. 2009) ; r (Abdo et al. 2009h) ; s (Abdo et al. 2009i) ; t (Abdo et al. 2009j).

Values taken from the ATNF database (Manchester et al. 2005) except for these notes: (1) (Halpern et al. 2004) ; (2) (Camilo et al. 2009b) ; (3) (Roberts et al. 2002) ; (4) (Halpern et al. 2007) ; (5) S_{1400} is for 2 GHz ; (6) S_{1400} is for 1.66 GHz (Ray et al. 1996).

Table 3. Detection parameters

PSR	Z_2^2 value	H value	maxROI(°)	ObsID
J0007+7303	2072.1	2371.8	1.0	L
J0030+0451	121.1	362.7	1.0	N
J0205+6449	90.9	206.0	1.0	G, J
J0218+4232	24.7	22.5	1.0	N, W
J0248+6021	57.5	75.1	0.5	N
J0357+32	422.7	450.7	1.0	L
J0437-4715	126.9	153.6	1.0	P
J0534+2200	4397.8	15285.0	1.0	N, J
J0613-0200	93.6	139.9	1.0	N
J0631+1036	48.6	44.8	1.0	N, J
J0633+0632	230.2	573.3	1.0	L
J0633+1746	10053.6	20346.4	1.0	L
J0659+1414	80.5	99.0	1.0	N, J
J0742-2822	38.9	44.9	1.0	N, J
J0751+1807	29.7	26.5	1.0	N
J0835-4510	26903.9	74716.7	1.0	P
J1028-5819	291.5	915.9	0.5	P
J1048-5832	208.5	634.0	1.0	P
J1057-5226	1668.9	1772.4	1.0	P
J1124-5916	93.5	179.9	1.0	L
J1418-6058	230.1	343.7	1.0	L
J1420-6048	104.7	114.4	1.0	P
J1459-60	148.2	159.3	1.0	L
J1509-5850	71.6	73.3	0.5	P
J1614-2230	36.2	69.5	0.5	G
J1709-4429	4680.1	5612.1	1.0	P
J1718-3825	111.9	109.8	0.5	N, P
J1732-31	141.2	279.6	1.0	L
J1741-2054	332.6	355.9	1.0	L
J1744-1134	28.4	38.1	1.0	N
J1747-2958	47.2	69.0	0.5	G
J1809-2332	589.3	1562.5	1.0	L
J1813-1246	140.0	162.0	1.0	L
J1826-1256	442.4	979.0	1.0	L
J1833-1034	35.2	87.6	1.0	G
J1836+5925	349.2	385.3	1.0	L
J1907+06	257.1	521.0	1.0	L
J1952+3252	464.8	1008.8	1.0	J, N
J1958+2846	146.9	233.1	1.0	L
J2021+3651	1433.5	4603.7	1.0	G, A
J2021+4026	222.0	275.8	1.0	L
J2032+4127	224.9	485.9	0.5	L
J2043+2740	28.2	38.2	1.0	N, J
J2124-3358	77.8	80.9	1.0	N
J2229+6114	1026.0	1237.4	1.0	G
J2238+59	135.8	373.0	1.0	L

A significance better than 5σ corresponds to $Z_2^2 > 36$ and $H > 42$.
A significance better than 7σ corresponds to $Z_2^2 > 61$.
A significance better than 10σ corresponds to $Z_2^2 > 114$.
H-test significances do not exceed 5.37σ (4.0×10^{-8} chance probability), because the H-test null hypothesis distribution function is computed by Monte-Carlo simulations.

Table 4. Spectral Parameters

PSR	Type[a]	Flux (F_{100} ON) 10^{-8} ph cm^{-2} s^{-1}	Eflux (G_{100} ON) 10^{-5} MeV cm^{-2} s^{-1}	Γ	E_{cutoff} (GeV)	TS	$\mathrm{TS}_{\mathrm{cutoff}}$	Luminosity 10^{-33} erg s^{-1}	Efficiency
J0007+7303	g	30.69 ± 1.09	23.85 ± 0.69	1.38 ± 0.04	4.6 ± 0.4	7384	274.7	89 ± 47	0.20
J0030+0451	m	5.83 ± 0.65	3.29 ± 0.22	1.22 ± 0.16	1.8 ± 0.4	960	59.2	0.57 ± 0.38	0.17
J0205+6449	r	13.23 ± 1.70	4.15 ± 0.34	2.09 ± 0.14	3.5 ± 1.4	346	12.5	54 – 81	0.002 – 0.003
J0218+4232	m	6.24 ± 1.39	2.26 ± 0.33	2.02 ± 0.23	5.1 ± 4.2	119	4.7	27 – 69	0.11 – 0.29
J0248+6021	r	3.66 ± 1.48	1.92 ± 0.36	1.15 ± 0.49	1.4 ± 0.6	103	18.5	15 – 300	0.07 – 1.40
J0357+32	g	10.39 ± 1.01	3.99 ± 0.23	1.29 ± 0.18	0.9 ± 0.2	949	71.6	...	...
J0437−4715	m	3.65 ± 0.70	1.16 ± 0.14	1.74 ± 0.32	1.3 ± 0.7	172	9.9	0.054 ± 0.016	0.02
J0534+2200[b]	r	209.00 ± 18.00	81.60 ± 7.03	1.97 ± 0.06	5.8 ± 1.2	21507	80.2	620 ± 360	0.001
J0613−0200	m	3.38 ± 0.71	2.02 ± 0.22	1.38 ± 0.24	2.7 ± 1.0	285	18.5	$0.89^{+0.75}_{-0.49}$	0.07
J0631+1036	r	2.77 ± 1.01	1.90 ± 0.32	1.38 ± 0.35	3.6 ± 1.8	86	10.0	2.0 – 48	0.01 – 0.27
J0633+06	g	8.41 ± 1.21	5.00 ± 0.40	1.29 ± 0.18	2.2 ± 0.6	370	50.8	...	...
J0633+1746	g	305.27 ± 2.86	211.31 ± 1.78	1.08 ± 0.02	1.9 ± 0.05	62307	5120.4	25^{+25}_{-15}	0.78
J0659+1414	r	10.00 ± 1.20	1.98 ± 0.19	2.37 ± 0.42	0.7 ± 0.5	206	6.9	0.31 ± 0.11	0.01
J0742−2822	r	3.18 ± 0.99	1.14 ± 0.22	1.76 ± 0.40	2.0 ± 1.4	47	4.2	$9.0^{+13}_{-9.0}$	0.07
J0751+1807	m	1.35 ± 0.55	0.68 ± 0.20	1.56 ± 0.58	3.0 ± 4.3	37	3.8	$0.47^{+0.95}_{-0.34}$	0.08
J0835−4510	r	1061.00 ± 5.83	549.56 ± 2.84	1.57 ± 0.01	3.2 ± 0.06	219585	5971.0	87 ± 28	0.01
J1028−5819	r	19.63 ± 2.57	11.07 ± 0.77	1.25 ± 0.17	1.9 ± 0.5	620	75.1	120 ± 80	0.14
J1048−5832	r	19.69 ± 2.49	10.77 ± 0.69	1.31 ± 0.15	2.0 ± 0.4	881	81.8	150 ± 100	0.08
J1057−5226	r	30.45 ± 1.42	17.00 ± 0.51	1.06 ± 0.08	1.3 ± 0.1	4961	366.3	17 ± 11	0.56
J1124−5916	r	5.16 ± 1.48	2.37 ± 0.36	1.43 ± 0.33	1.7 ± 0.7	111	16.7	100^{+40}_{-60}	0.01
J1418−6058	g	27.73 ± 6.90	14.74 ± 1.96	1.32 ± 0.20	1.9 ± 0.4	162	54.1	110 – 700	0.02 – 0.14
J1420−6048	r	24.22 ± 6.62	9.90 ± 1.75	1.73 ± 0.20	2.7 ± 1.0	63	21.4	590 ± 400	0.06
J1459−60	g	17.83 ± 2.81	6.60 ± 0.60	1.83 ± 0.20	2.7 ± 1.1	337	21.1	...	...
J1509−5850	r	8.71 ± 1.99	6.05 ± 0.63	1.36 ± 0.23	3.5 ± 1.1	262	26.3	78 ± 54	0.15
J1614−2230	m	2.89 ± 0.97	1.71 ± 0.26	1.34 ± 0.36	2.4 ± 1.0	149	13.3	5.3 ± 3.6	1.03
J1709−4429	r	149.76 ± 3.38	77.53 ± 1.38	1.70 ± 0.03	4.9 ± 0.4	16009	373.6	290 – 1900	0.09 – 0.57
J1718−3825	r	9.14 ± 4.82	4.21 ± 1.03	1.26 ± 0.62	1.3 ± 0.6	105	19.7	120 ± 80	0.09
J1732−31	g	25.28 ± 2.50	15.10 ± 0.76	1.27 ± 0.12	2.2 ± 0.3	1002	131.2	...	...
J1741−2054	g	20.27 ± 1.73	8.01 ± 0.41	1.39 ± 0.14	1.2 ± 0.2	935	92.6	2.2 ± 1.4	0.24
J1744−1134	m	4.34 ± 1.28	1.75 ± 0.29	1.02 ± 0.59	0.7 ± 0.4	78	20.0	0.43 ± 0.15	0.10
J1747−2958	r	18.19 ± 3.49	8.17 ± 0.85	1.11 ± 0.28	1.0 ± 0.2	213	59.3	63 ± 42	0.02
J1809−2332	g	49.52 ± 2.53	25.79 ± 0.81	1.52 ± 0.06	2.9 ± 0.3	3451	201.9	140 ± 170	0.33
J1813−1246	g	28.11 ± 2.91	10.57 ± 0.67	1.83 ± 0.12	2.9 ± 0.8	482	39.7	...	...
J1826−1256	g	41.77 ± 3.35	20.87 ± 0.91	1.49 ± 0.09	2.4 ± 0.3	1152	138.0	...	...
J1833−1034	r	20.46 ± 3.79	6.34 ± 0.76	2.24 ± 0.15	7.7 ± 4.8	110	4.9	270 ± 90	0.01
J1836+5925[c]	g	65.56 ± 1.46	37.43 ± 0.67	1.35 ± 0.03	2.3 ± 0.1	20982	674.6	<46	<4.0

a. Types are r=radio-selected, g=gamma-selected, m=millisecond.

b. For the Crab the spectral parameters come from (Abdo et al. 2009d).

c. For J1836+5925 the spectral parameters come from the phase-averaged analysis.

d. For J2021+4026 the spectral parameters come from the phase-averaged analysis.

Table 4—Continued

PSR	Type[a]	Flux (F_{100} ON) 10^{-8} ph cm^{-2} s^{-1}	Eflux (G_{100} ON) 10^{-5} MeV cm^{-2} s^{-1}	Γ	$E_{\rm cutoff}$ (GeV)	TS	TS$_{\rm cutoff}$	Luminosity 10^{-33} erg s^{-1}	Efficiency
J1907+06	g	40.25 ± 3.20	17.19 ± 0.80	1.84 ± 0.08	4.6 ± 1.0	1209	59.3	...	...
J1952+3252	r	17.62 ± 1.62	8.36 ± 0.46	1.75 ± 0.10	4.5 ± 1.2	1008	36.4	64 ± 37	0.02
J1958+2846	g	7.65 ± 1.33	5.28 ± 0.43	0.77 ± 0.26	1.2 ± 0.2	491	89.2	...	...
J2021+3651	r	67.35 ± 3.67	29.36 ± 0.91	1.65 ± 0.06	2.6 ± 0.3	3138	223.5	$250\,^{+500}_{-250}$	0.07
J2021+4026[d]	g	152.62 ± 4.06	60.98 ± 1.06	1.79 ± 0.03	3.0 ± 0.2	10180	331.4	260 ± 180	2.2
J2032+4127	g	6.04 ± 1.92	6.96 ± 0.76	0.68 ± 0.38	2.1 ± 0.6	487	56.3	170 ± 120	0.64
J2043+2740	r	2.41 ± 0.75	0.97 ± 0.17	1.07 ± 0.55	0.8 ± 0.3	79	15.1	6.0 ± 4.0	0.09
J2124−3358	m	1.95 ± 0.41	1.72 ± 0.22	1.05 ± 0.28	2.7 ± 1.0	226	22.9	$0.21\,^{+0.42}_{-0.15}$	0.05
J2229+6114	r	32.62 ± 1.82	13.73 ± 0.51	1.74 ± 0.07	3.0 ± 0.5	1929	96.0	17 – 1100	0.001 – 0.05
J2238+59	g	6.77 ± 1.46	3.40 ± 0.37	1.00 ± 0.36	1.0 ± 0.3	219	37.2	...	...

Table 5. Source Associations

PSR	Alt. name	LAT catalog association	EGRET associations	Positional associations
J0007+7303	···	0FGL J0007.4+7303	3EG J0010+7309	CTA 1
			EGR J0008+7308	PWN G119.5+10.2 [1]
J0030+0451	···	0FGL J0030.3+0450	EGR J0028+0457	···
J0205+6449	···	···	···	3C 58
				PWN G119.5+10.2 [1]
J0218+4232	···	···	···	···
J0248+6021	···	···	···	···
J0357+32	···	0FGL J0357.5+3205	···	···
J0437−4715	PSR B0435−47	···	···	PWN G253.4−42.0 [1]
J0534+2200	Crab	0FGL J0534.6+2201	3EG J0534+2200	PWN/SNR G184.6−5.8 [1]
	PSR B0531+21		EGR J0534+2159	HESS J0534+220 [4]
J0613−0200	···	0FGL J0613.9−0202	···	···
J0631+1036	···	0FGL J0631.8+1034	···	···
J0633+0632	···	0FGL J0633.5+0634	3EG J0631+0642	···
			EGR J0633+0646	
J0633+1746	Geminga	0FGL J0634.0+1745	3EG J0633+1751	PWN G195.1+4.3 [1]
	PSR B0630+17			MGRO J0632+17 [3]
J0659+1414	PSR B0656+14	···	···	SNR 203.0+12.0
J0742−2822	PSR B0740−28	···	···	···
J0751+1807	···	···	···	···
J0835−4510	Vela	0FGL J0835.4−4510	3EG J0834−4511	PWN G263.9−3.3 [1]
	PSR B0833−45			HESS J0835-455 [5]
J1028−5819	···	0FGL J1028.6−5817	3EG J1027−5817	···
J1048−5832	PSR B1046−58	0FGL J1047.6−5834	3EG J1048−5840	PWN G287.4+0.58 [1]
			EGR J1048-5839	
J1057−5226	PSR B1055−52	0FGL J1058.1−5225	3EG J1058−5234	···
			EGR J1058-5221	
J1124−5916	···	···	···	MSH 11−54
				PWN/SNR G292.0+1.8 [1]
J1418−6058	···	0FGL J1418.8−6058	3EG J1420−6038	PWN G313.3+0.1 [1]
				HESS J1418-609 [6]
J1420−6048	···	···	3EG J1420-6038	PWN G313.6+0.3 [1]
			EGR J1418-6040	HESS J1420-607 [6]
J1459−60	···	0FGL J1459.4−6056	···	···
J1509−5850	···	0FGL J1509.5−5848	···	PWN G319.97−0.62 [1]
J1614−2230	···	···	3EG J1616−2221	···
J1709−4429	PSR B1706−44	0FGL J1709.7−4428	3EG J1710−4439	PWN G343.1−2.3 [1]
				HESS J1708-443 [7]
J1718−3825	···	···	···	HESS J1718-385 [8]
J1732−31	···	0FGL J1732.8−3135	3EG J1734-3232	···
			EGR J1732-3126	
J1741−2054	···	0FGL J1742.1−2054	3EG J1741−2050	···
J1744−1134	PSR B1741−11	···	···	···
J1747−2958	···	···	···	PWN G359.23−0.82 [1]
J1809−2332	···	0FGL J1809.5−2331	3EG J1809−2328	PWN G7.4−2.0 [1]
J1813−1246	···	0FGL J1813.5−1248	···	···
J1826−1256	···	0FGL J1825.9−1256	3EG J1826−1302	PWN G18.5−0.4 [1]
J1833−1034	···	···	···	PWN G21.5−0.9 [1]
				HESS J1833-105 [9]

Table 5—Continued

PSR	Alt. name	LAT catalog association	EGRET associations	Positional associations
J1836+5925	···	0FGL J1836.2+5924	3EG J1835+5918	···
J1907+06	···	0FGL J1907.5+0602	···	MGRO J1908+063 [3]
				HESS J1908+06 [10]
J1952+3252	PSR B1952+32	0FGL J1953.2+3249	···	CTB 80
				PWN G69.0+2.7 [1]
J1958+2846	···	0FGL J1958.1+2848	3EG J1958+2909	···
J2021+3651	···	0FGL J2020.8+3649	···	PWN G75.2+0.1 [1]
				MGRO J2019+37 [3]
J2021+4026	···	0FGL J2021.5+4026	3EG J2020+4017	γ Cygni
				SNR G078.1+01.8 [2]
J2032+4127	···	0FGL J2032.2+4122	3EG J2033+4118	MGRO J2031+41 [3]
			EGR J2033+4117	
J2043+2740	···	···	···	···
J2124−3358	···	0FGL J2124.7−3358	···	PWN G10.9−45.4 [1]
J2229+6114	···	0FGL J2229.0+6114	3EG J2227+6122	PWN G106.6+2.9 [1]
			EGR J2227+6114	MGRO J2228+60 [3]
J2238+59	···	···	···	···

References. — 1. Roberts et al. (2005), 2. Green (2009), 3. Abdo et al. (2009u), 4. Aharonian et al. (2006a), 5. Aharonian et al. (2006b), 6. Aharonian et al. (2006c), 7. Hoppe et al. (2009), 8. Aharonian et al. (2007), 9. H. E. S. S. Collaboration: A. Djannati-Atai et al. (2007), 10. Aharonian et al. (2009)

Table 6. Pulse shape parameters

PSR	Type[a]	Peak multiplicity	Radio lag δ	γ-ray peak separation Δ	Off-pulse definition ϕ
J0007+7303	g	2	...	0.23 ± 0.01	0.29 − 0.87
J0030+0451	m	2	0.18 ± 0.01	0.44 ± 0.01	0.68 − 0.12
J0205+6449	r	2	0.08 ± 0.01	0.50 ± 0.01	0.64 − 0.02
J0218+4232	m	2	0.32 ± 0.02	0.36 ± 0.02	0.84 − 0.16
J0248+6021	r	1	0.35 ± 0.01	...	0.71 − 0.19
J0357+32	g	1	...	...	0.34 − 0.86
J0437−4715	m	1	0.43 ± 0.02	...	0.60 − 0.20
J0534+2200	r	2	0.09 ± 0.01	0.40 ± 0.01	0.62 − 0.98
J0613−0200	m	1	0.42 ± 0.01	...	0.56 − 0.16
J0631+1036	r	1	0.54 ± 0.02	...	0.80 − 0.20
J0633+06	g	2	...	0.48 ± 0.01	0.09 − 0.45
J0633+1746	g	2	...	0.50 ± 0.01	0.24 − 0.54
J0659+1414	r	1	0.21 ± 0.01	...	0.40 − 1.00
J0742−2822	r	1	0.61 ± 0.02	...	0.84 − 0.44
J0751+1807	m	1	0.43 ± 0.02	...	0.63 − 0.99
J0835−4510	r	2	0.13 ± 0.01	0.43 ± 0.01	0.66 − 0.06
J1028−5819	r	2	0.19 ± 0.01	0.47 ± 0.01	0.76 − 0.12
J1048−5832	r	2	0.15 ± 0.01	0.42 ± 0.02	0.64 − 0.04
J1057−5226	r	2	0.35 ± 0.05	0.20 ± 0.07	0.72 − 0.20
J1124−5916	r	2	...	0.49 ± 0.01	0.60 − 0.96
J1418−6058	g	2	...	0.47 ± 0.01	0.54 − 0.90
J1420−6048	r	2[b]	0.26 ± 0.02	0.18 ± 0.02	0.60 − 0.10
J1459−60	g	2	...	0.15 ± 0.03	0.34 − 0.78
J1509−5850	r	2[b]	0.18 ± 0.03	0.20 ± 0.03	0.52 − 1.00
J1614−2230	m	2	0.19 ± 0.01	0.51 ± 0.01	0.92 − 0.14
J1709−4429	r	2	0.24 ± 0.01	0.25 ± 0.01	0.66 − 0.14
J1718−3825	r	1	0.42 ± 0.02	...	0.68 − 0.20
J1732−31	g	2	...	0.42 ± 0.02	0.49 − 0.93
J1741−2054	g	2	0.30 ± 0.01	0.18 ± 0.02	0.67 − 0.19
J1744−1134	m	1	0.83 ± 0.02	...	0.08 − 0.44
J1747−2958	r	2	0.18 ± 0.01	0.42 ± 0.04	0.64 − 0.10
J1809−2332	g	2	...	0.35 ± 0.01	0.41 − 0.89
J1813−1246	g	2	...	0.47 ± 0.02	0.56 − 0.90
J1826−1256	g	2	...	0.47 ± 0.01	0.54 − 0.94
J1833−1034	r	2	0.15 ± 0.01	0.44 ± 0.01	0.68 − 0.10
J1836+5925	g	2	...	0.48 ± 0.01	...
J1907+06	g	2	...	0.40 ± 0.01	0.46 − 0.94
J1952+3252	r	2	0.15 ± 0.01	0.49 ± 0.01	0.68 − 0.08
J1958+2846	g	2	...	0.45 ± 0.01	0.55 − 0.95
J2021+3651	r	2	0.17 ± 0.01	0.47 ± 0.01	0.70 − 0.04
J2021+4026	g	2	...	0.48 ± 0.01	...
J2032+4127	g	2	0.15 ± 0.01	0.50 ± 0.01	0.60 − 0.92
J2043+2740	r	2	0.20 ± 0.01	0.36 ± 0.01	0.64 − 0.08
J2124−3358	m	1	0.86 ± 0.02	...	0.92 − 0.58
J2229+6114	r	1	0.49 ± 0.01	...	0.64 − 0.14
J2238+59	g	2	0.00 ± 0.01	0.50 ± 0.01	0.60 − 0.92

a. Types are r=radio-selected, g=gamma-selected, m=millisecond.

b. For some pulse profiles the current dataset does allow clear discrimination between a single, broad pulse and two unresolved pulses. See the discussion in (Weltevrede et al. 2009a) regarding PSRs J1420−6048 and J1509−5850.

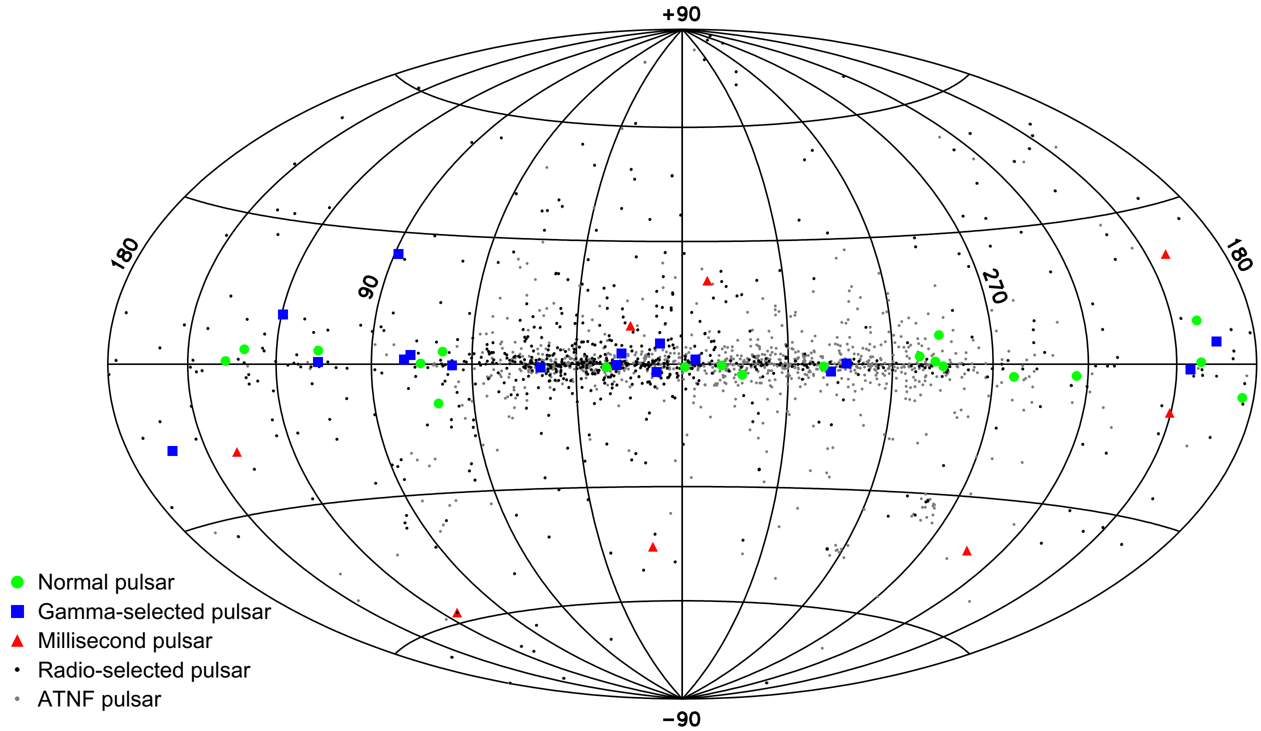

Fig. 1.— Pulsar sky map. Blue squares: gamma-selected pulsars. Red triangles: millisecond gamma-ray pulsars. Green disks: all other radio loud gamma-ray pulsars. Black dots: Pulsars for which gamma-ray pulsation searches were conducted using rotation ephemerides. Gray dots: All other ATNF pulsars.

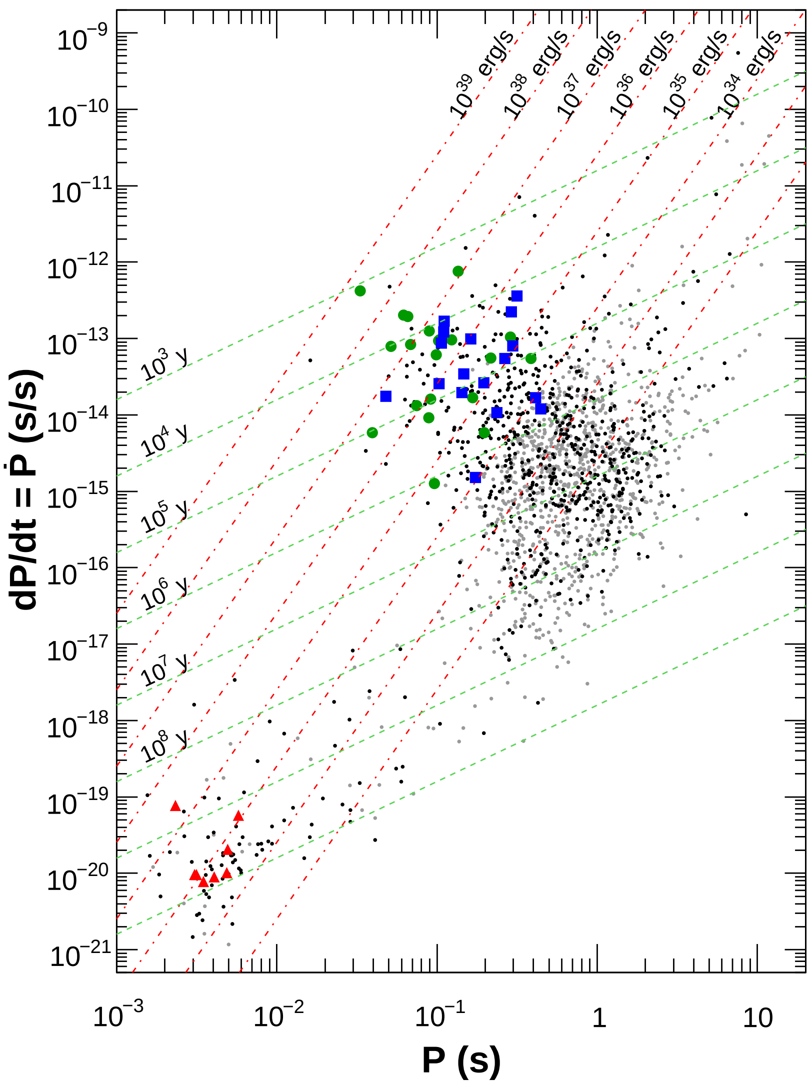

Fig. 2.— $P - \dot{P}$ diagram. Dashed lines: timing age. Dot-dashed lines: rotational energy loss rate. Symbols as in Figure 1.

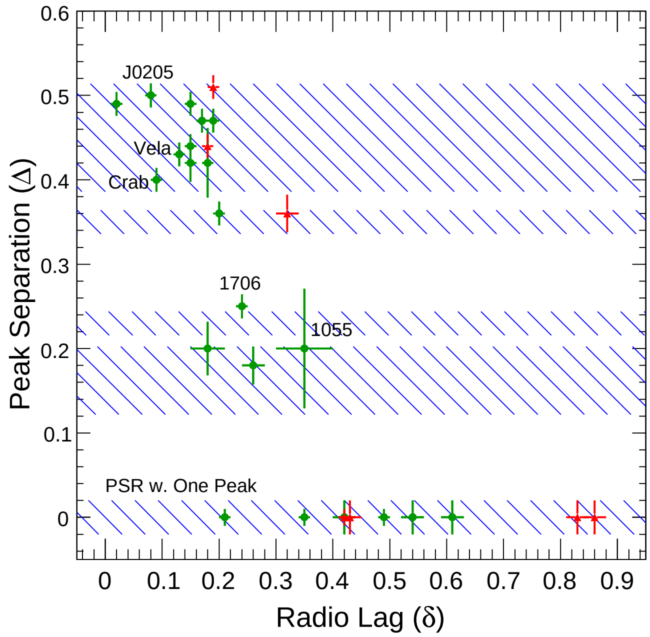

Fig. 3.— Phase-difference Δ between the gamma-ray peaks, versus the phase-difference δ between the main radio peak and the nearest gamma-ray peak. When there is only one gamma-ray peak, Δ is set to zero. For pulsars undetected in radio, the blue-hashed zone covers the full δ range. Symbols as in Figure 1.

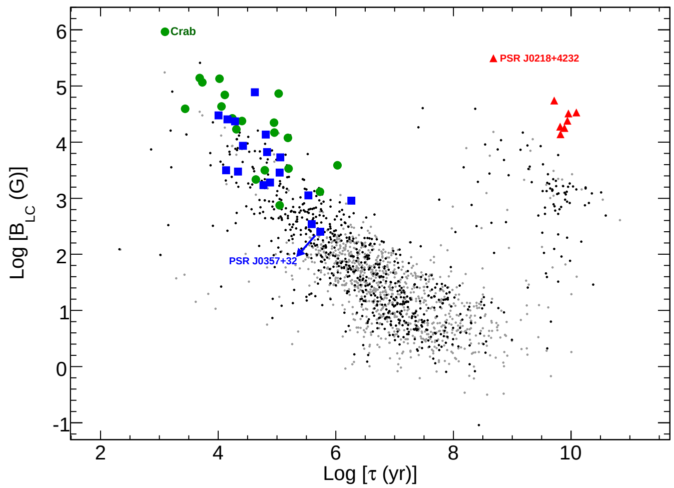

Fig. 4.— Magnetic field strength at the light cylinder versus pulsar characteristic age. Symbols as in Figure 1.

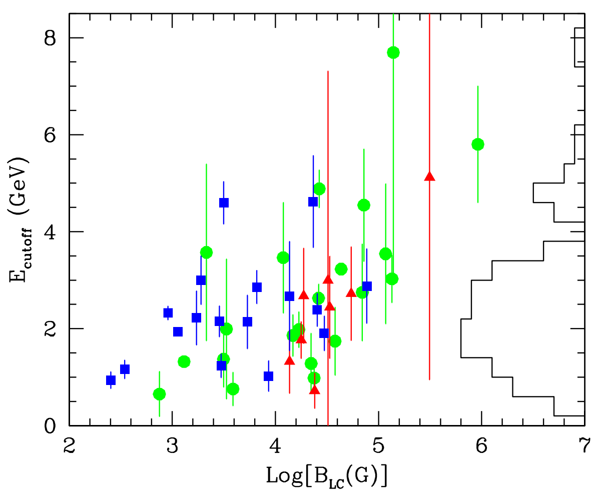

Fig. 5.— Value of the exponential cutoff of the power-law energy spectrum, versus the magnetic field strength at the light cylinder. Symbols as in Figure 1. The histogram of the cut-off values is projected along the right-hand axis.

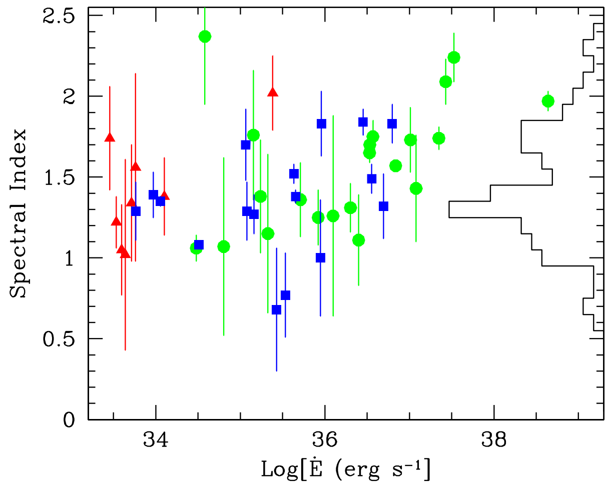

Fig. 6.— Spectral index versus the rotational energy loss rate, $\dot{E}$. Symbols as in Figure 1. The histogram of the spectral indices is projected along the right-hand axis.

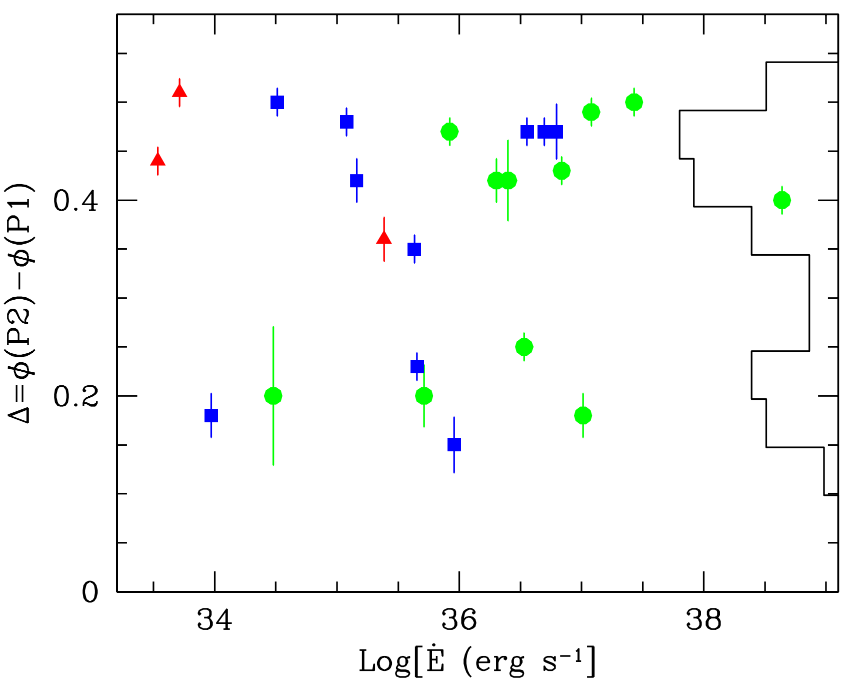

Fig. 7.— Separations Δ between the gamma-ray peaks, for those pulsars with two gamma-ray peaks, versus the spin-down power $\dot{E}$. Symbols as in Figure 1.

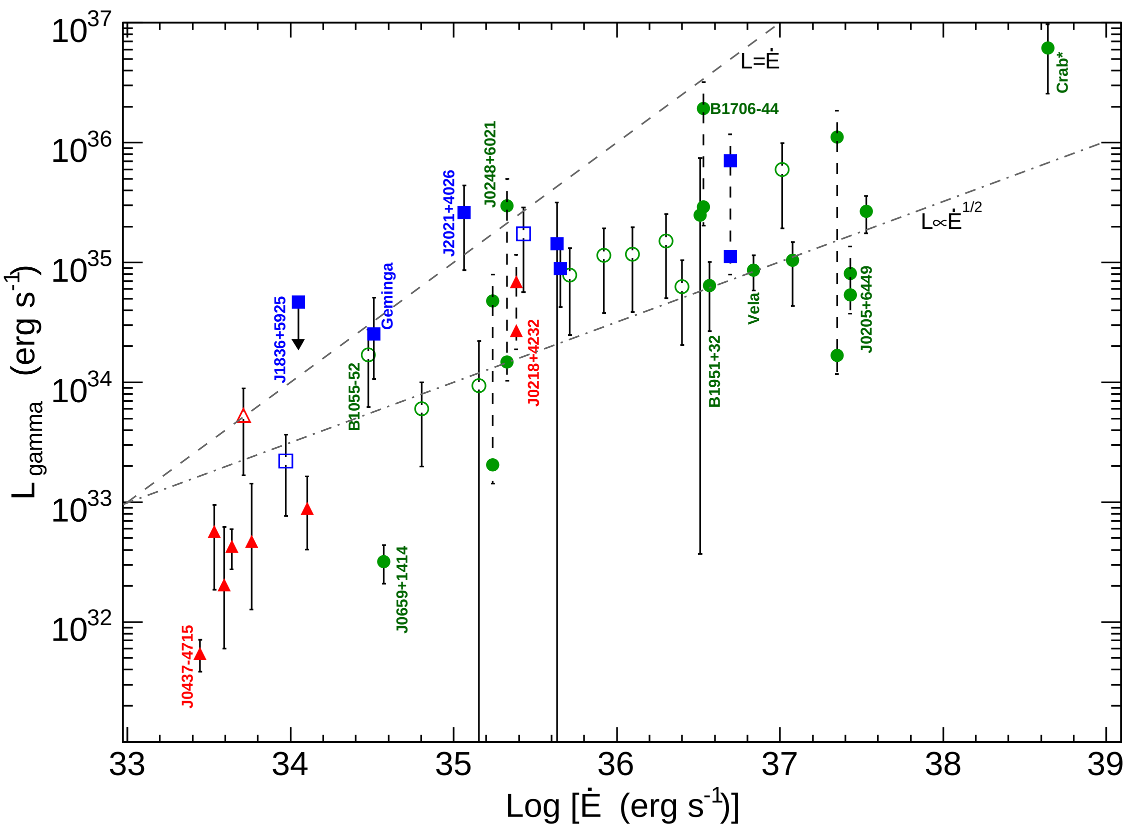

Fig. 8.— Gamma-ray luminosity versus the rotational energy loss rate. Dashed line: luminosity equal to the spin-down power. Dot-dashed line: luminosity proportional to the square root of the spin-down power. The gamma-ray luminosity is calculated using a beam correction factor $f_\Omega = 1$ for all pulsars and the integral energy flux G_{100} from the On-pulse spectral analysis. For the Crab we account for the X-ray luminosity as described in the text ($L = L_X + L_\gamma$). Symbols as in Figure 1. Unfilled markers indicate pulsars for which only a DM-based distance estimate is available. Pulsars with double distance estimate have two markers connected with dashed error bars.

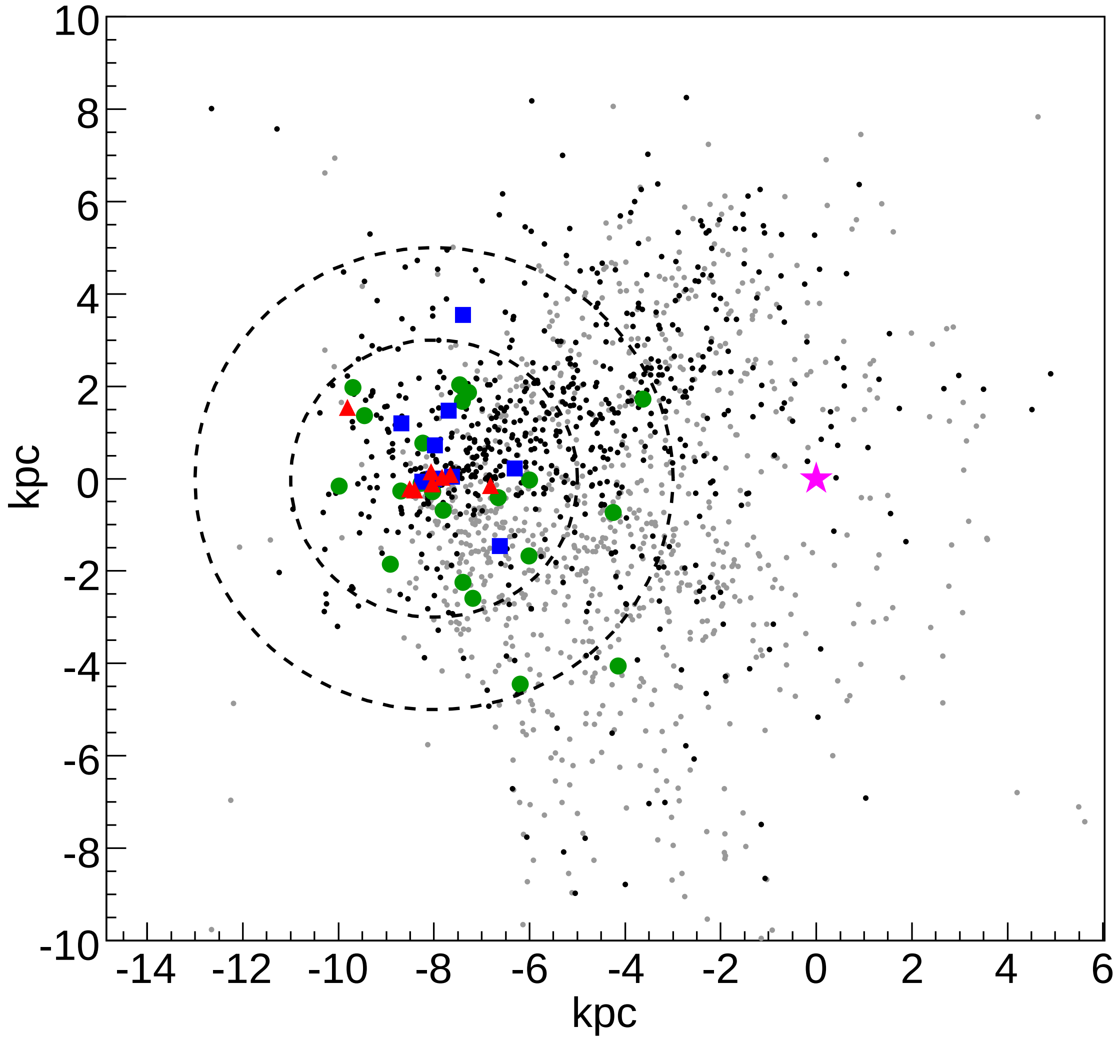

Fig. 9.— Galactic plane pulsar distribution (polar view). The star represents the Galactic center. The two circles centered at the Earth's position have radii of 3 kpc and 5 kpc. For pulsars with different possible distances, the nearer values from Table 1 are used. Symbols as in Figure 1.

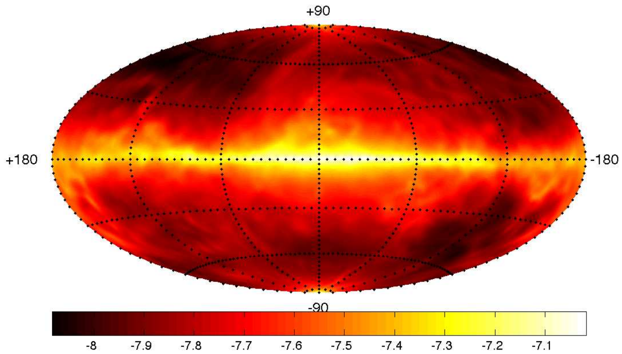

Fig. 10.— Aitoff projection sky map of the 5σ flux sensitivity for six months of *Fermi* LAT sky survey data, for the model of the diffuse gamma-ray background described in the text, and pulsar spectra with differential photon indexes of $\Gamma = 1.4$ and an exponential cut-off energy of $E_{\rm cutoff} = 2.2$ GeV.

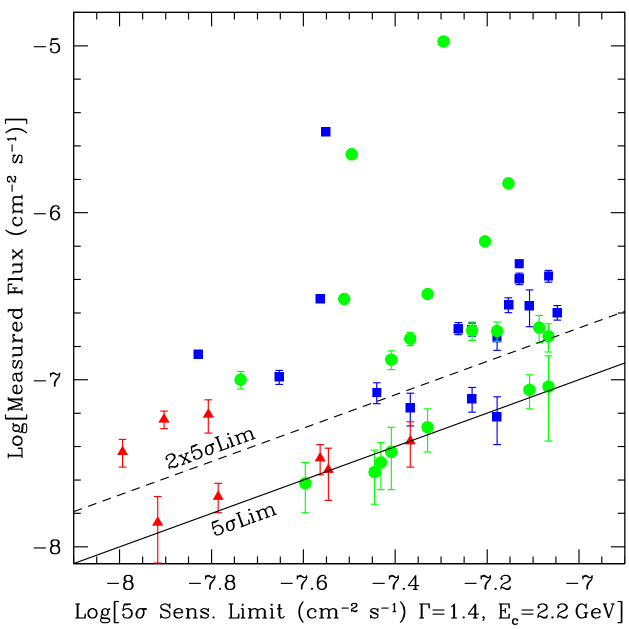

Fig. 11.— Measured integral photon flux above 100 MeV versus the 5σ flux sensitivity described in the preceding figure. Symbols as in Figure 1.

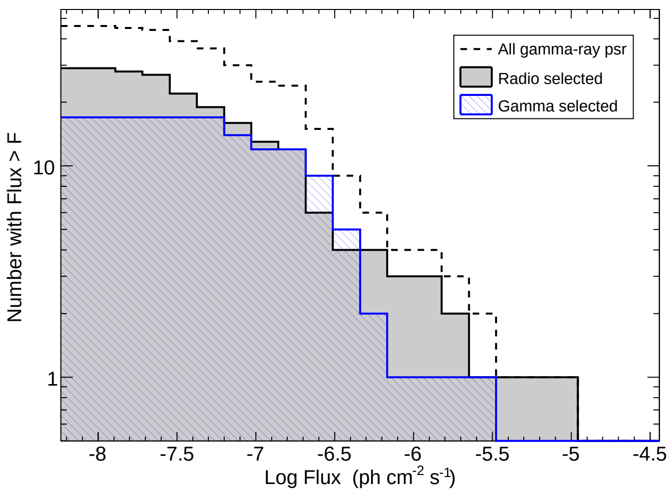

Fig. 12.— LogN-LogS distribution for all the detected pulsars (black dashed line), the radio-selected gamma-ray pulsars including MSPs (grey histogram), and the gamma-selected pulsars (blue hatched histogram).

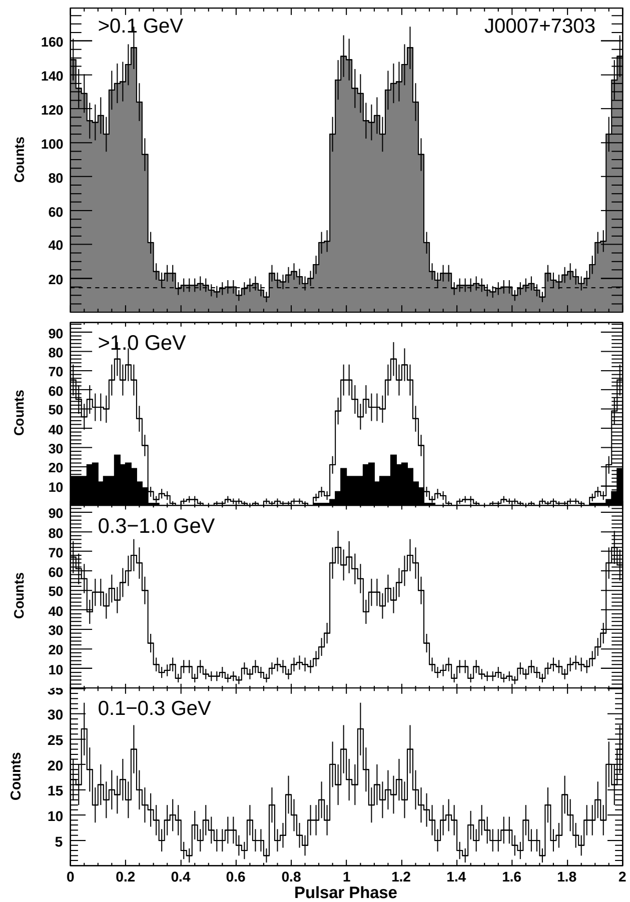

Fig. 13.— Light curves for PSR J0007+7303.

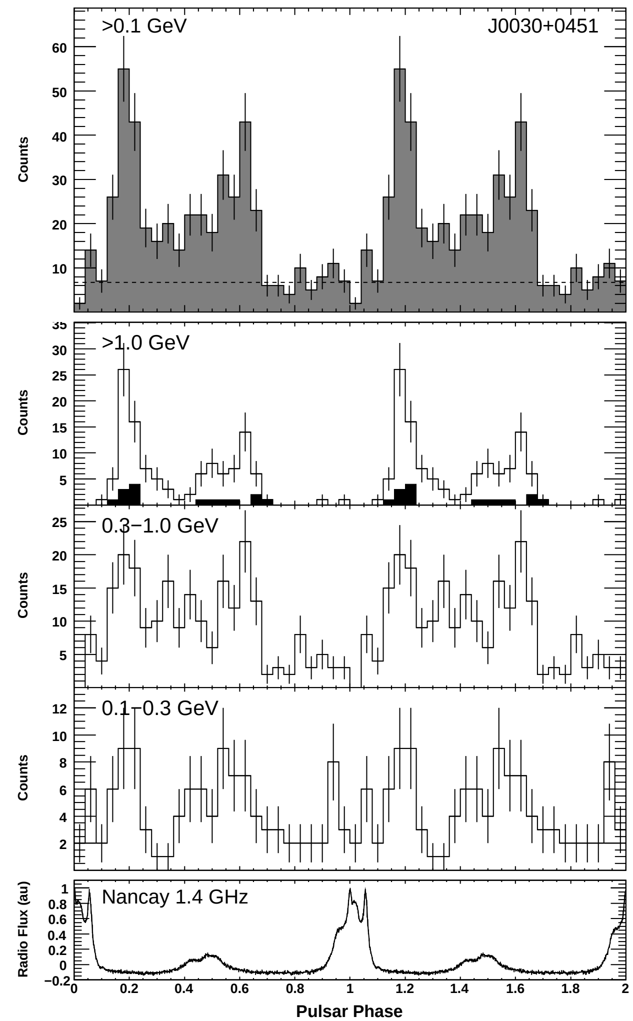

Fig. 14.— Light curves for PSR J0030+0451.

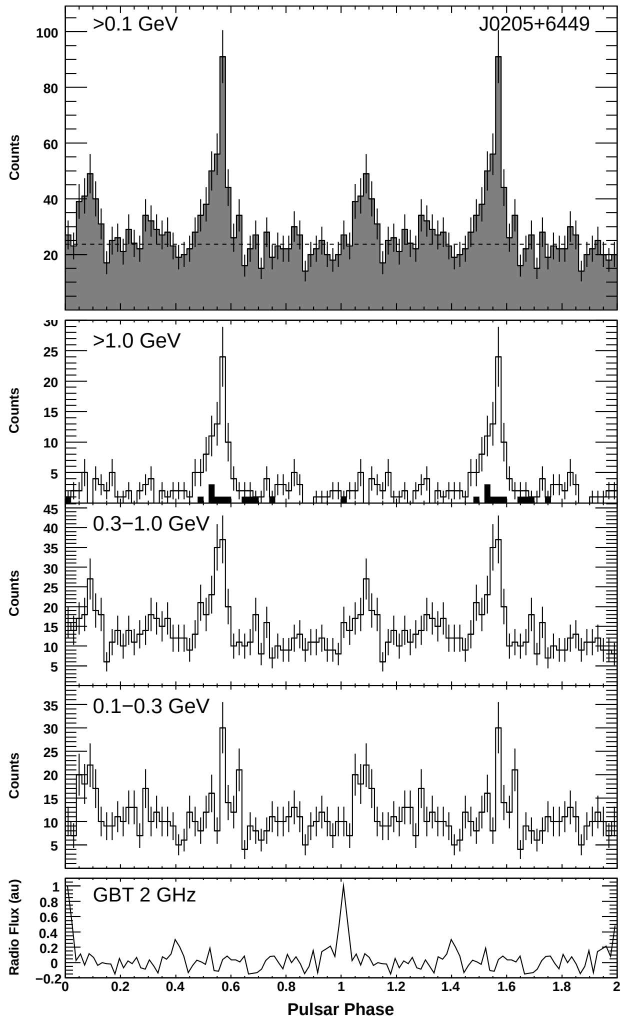

Fig. 15.— Light curves for PSR J0205+6449.

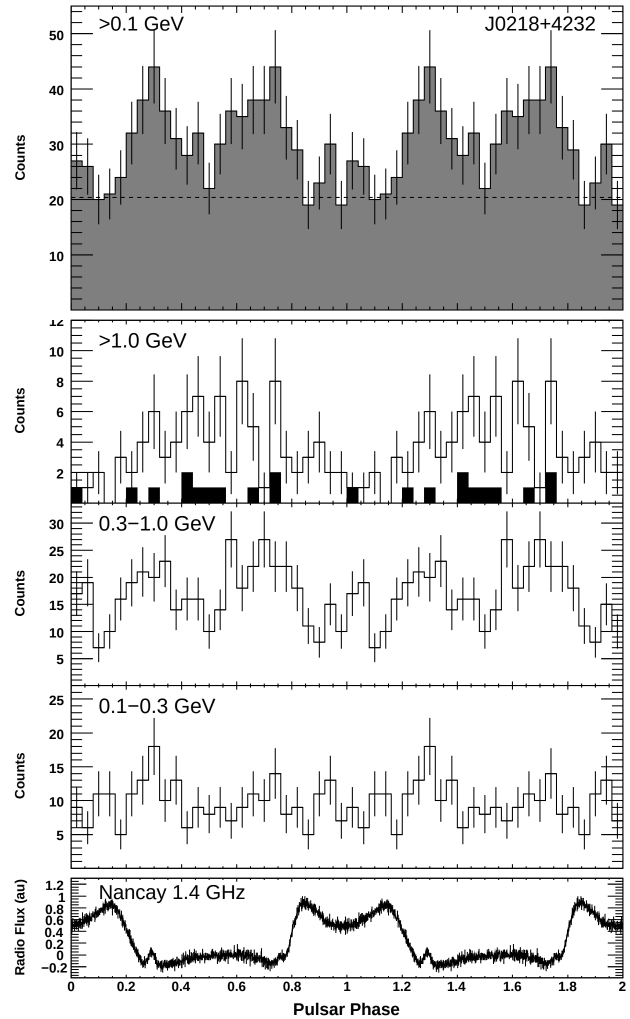

Fig. 16.— Light curves for PSR J0218+4232.

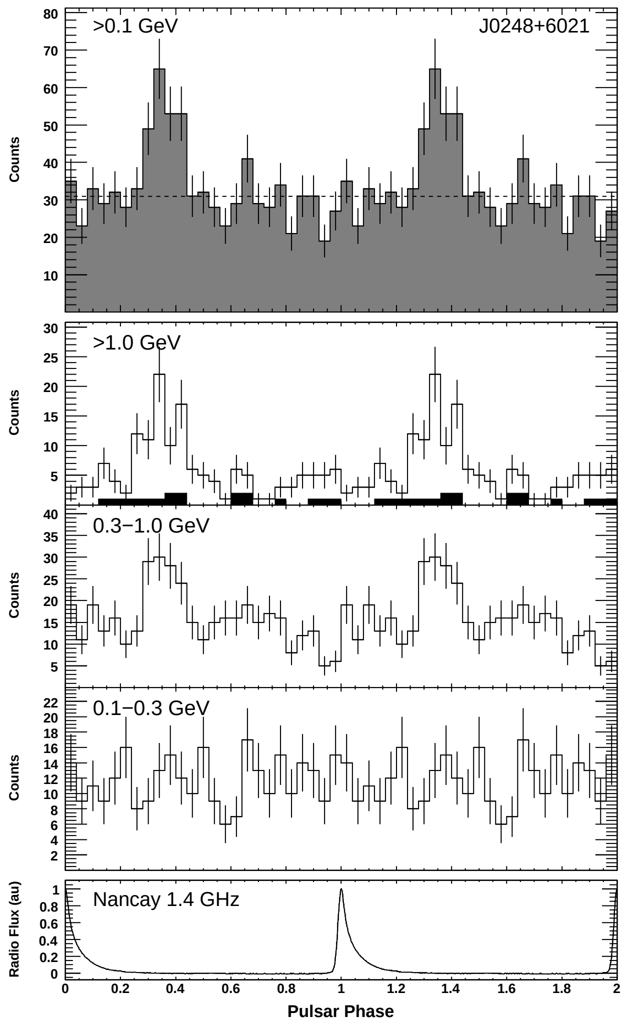

Fig. 17.— Light curves for PSR J0248+6021.

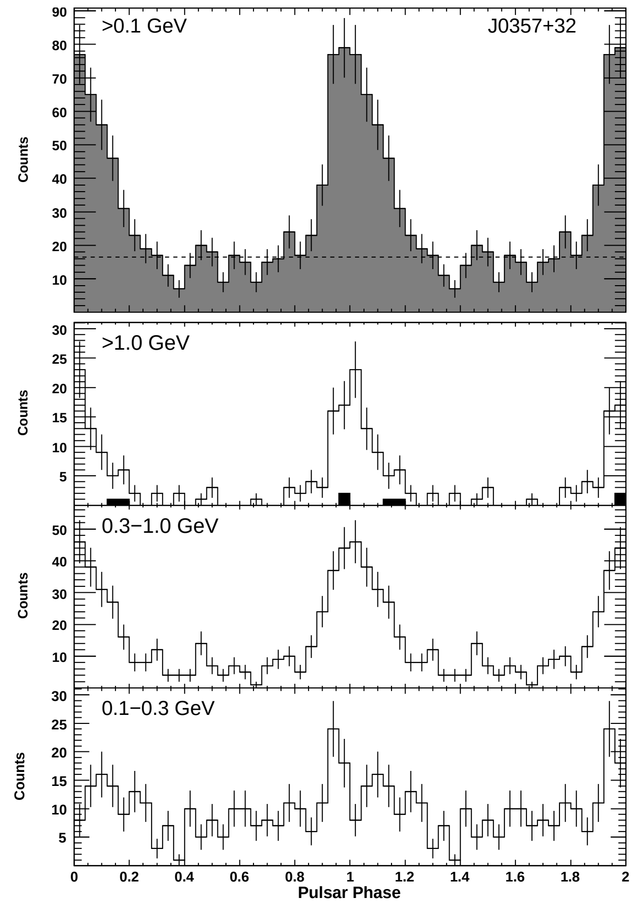

Fig. 18.— Light curves for PSR J0357+32.

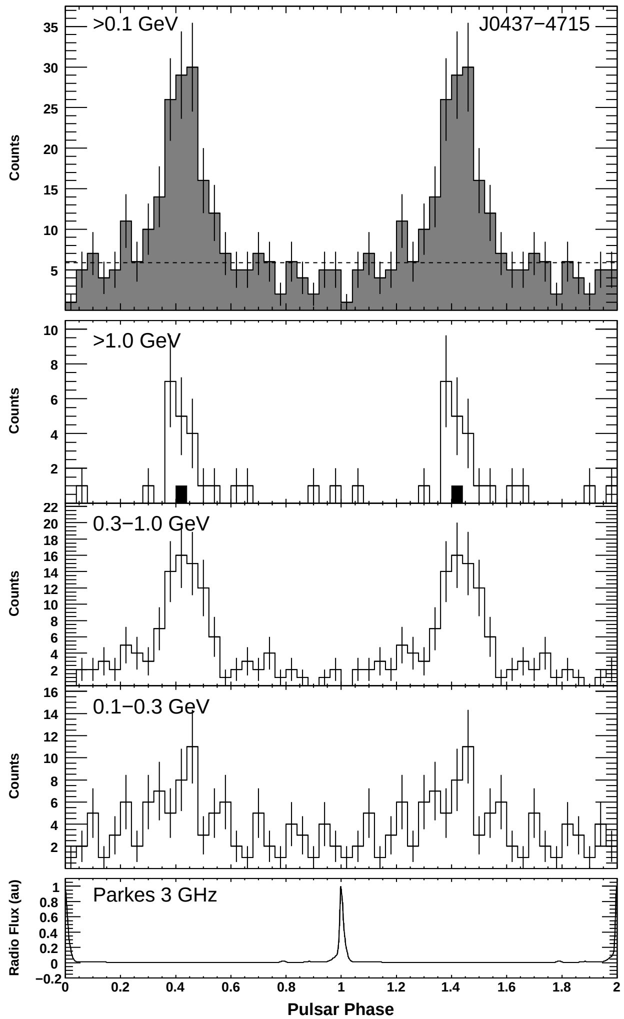

Fig. 19.— Light curves for PSR J0437–4715.

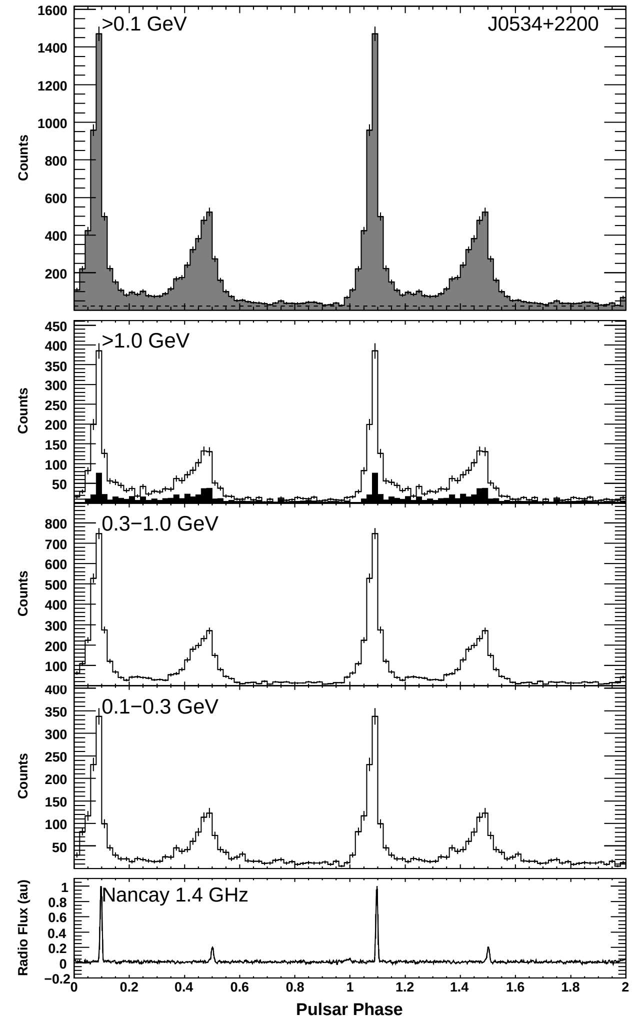

Fig. 20.— Light curves for PSR J0534+2200 (Crab pulsar).

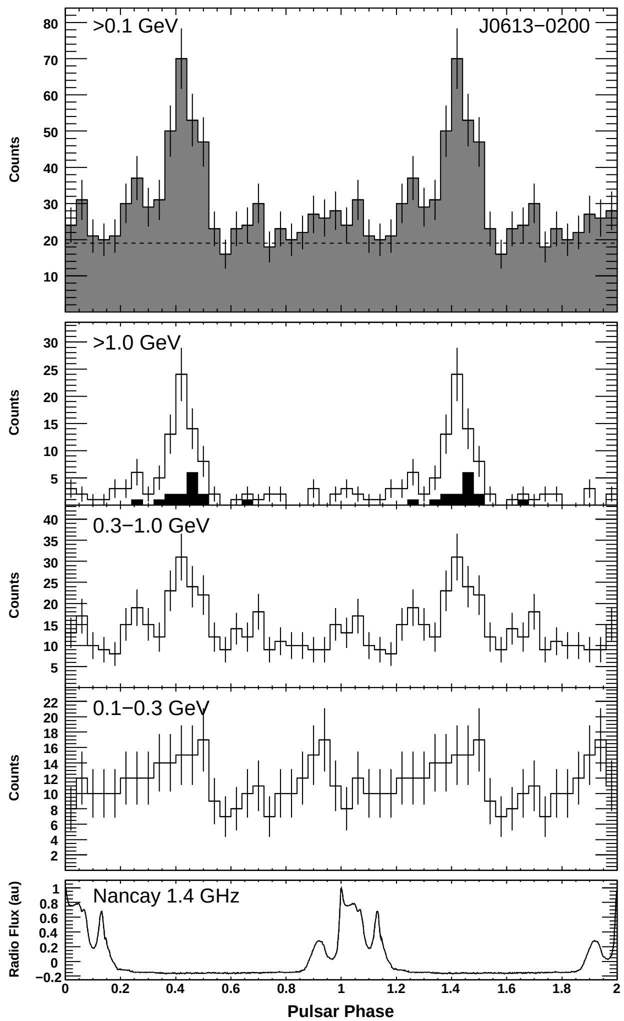

Fig. 21.— Light curves for PSR J0613–0200.

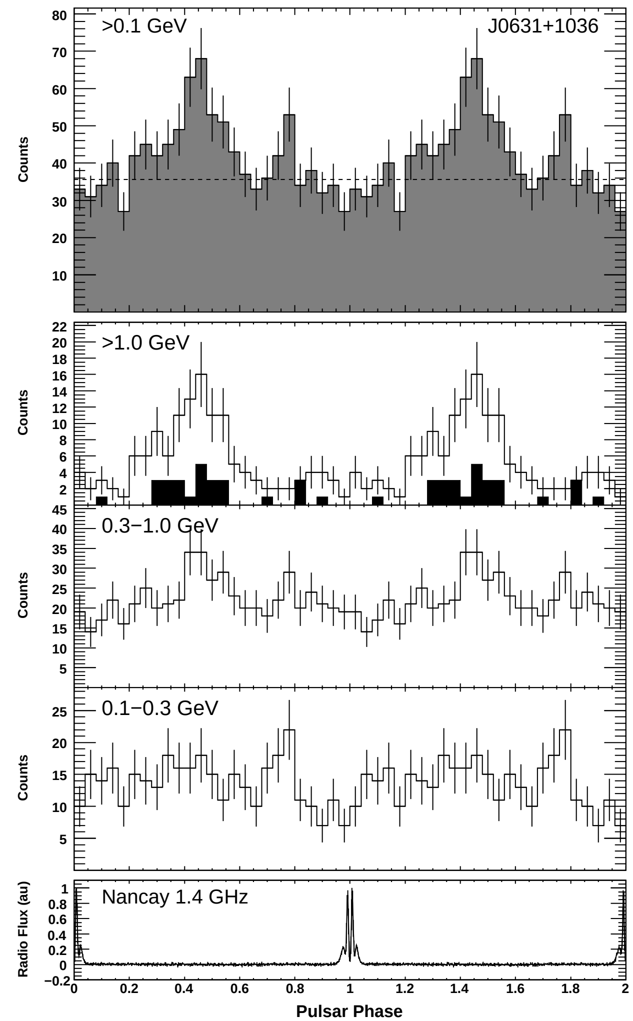

Fig. 22.— Light curves for PSR J0631+1036.

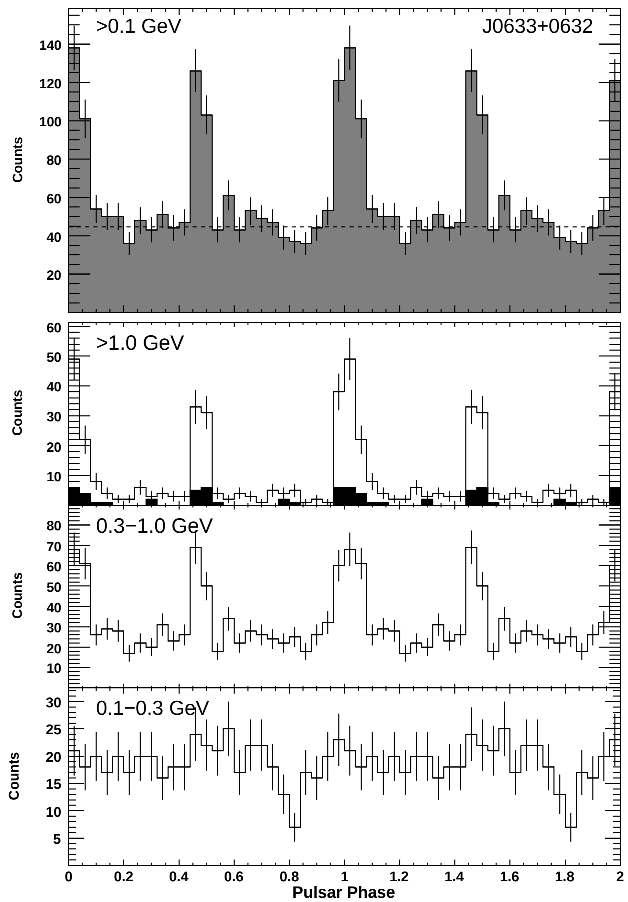

Fig. 23.— Light curves for PSR J0633+0632.

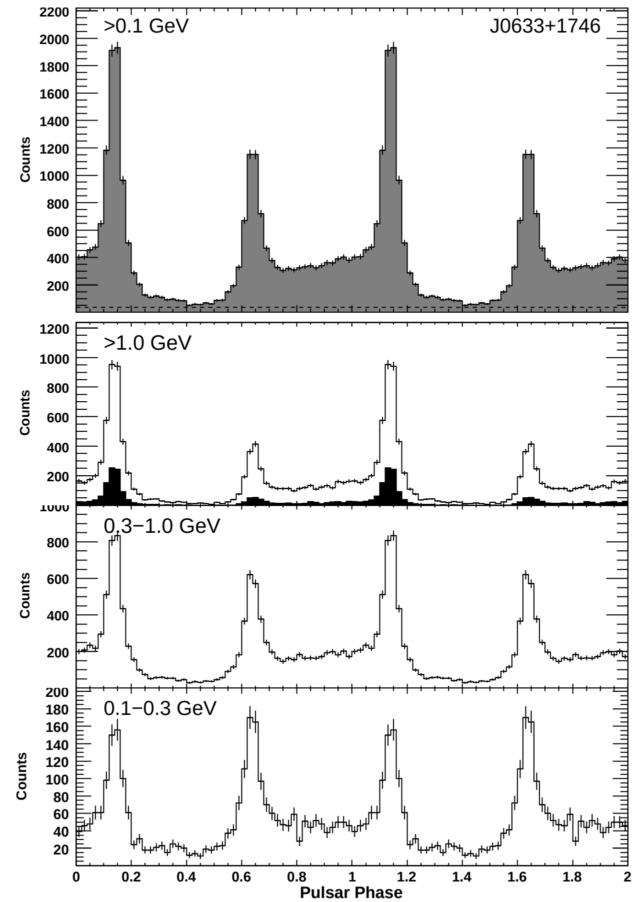

Fig. 24.— Light curves for PSR J0633+1746.

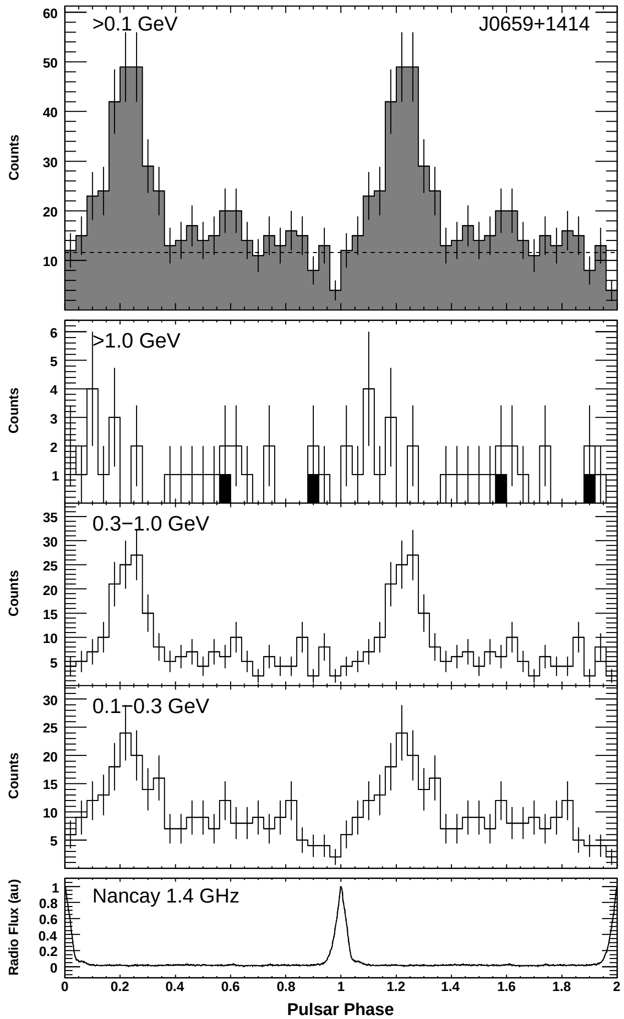

Fig. 25.— Light curves for PSR J0659+1414.

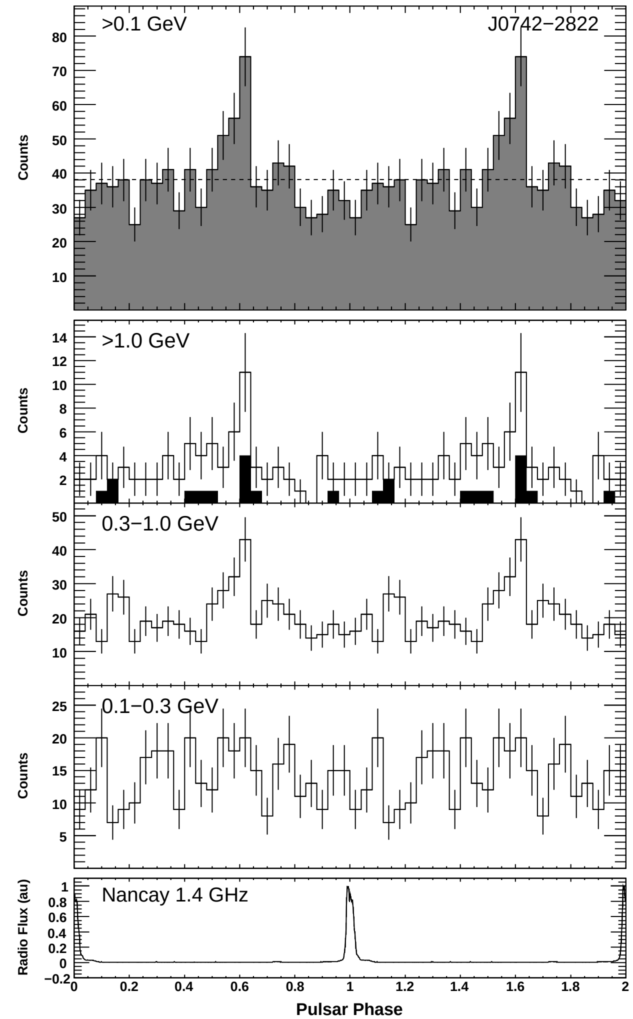

Fig. 26.— Light curves for PSR J0742–2822.

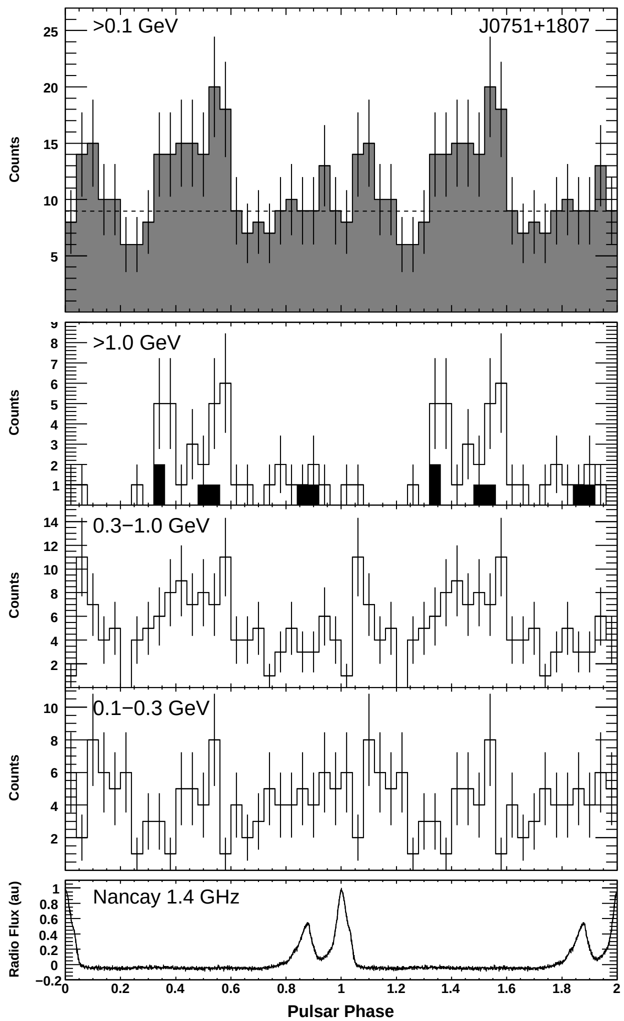

Fig. 27.— Light curves for PSR J0751+1807.

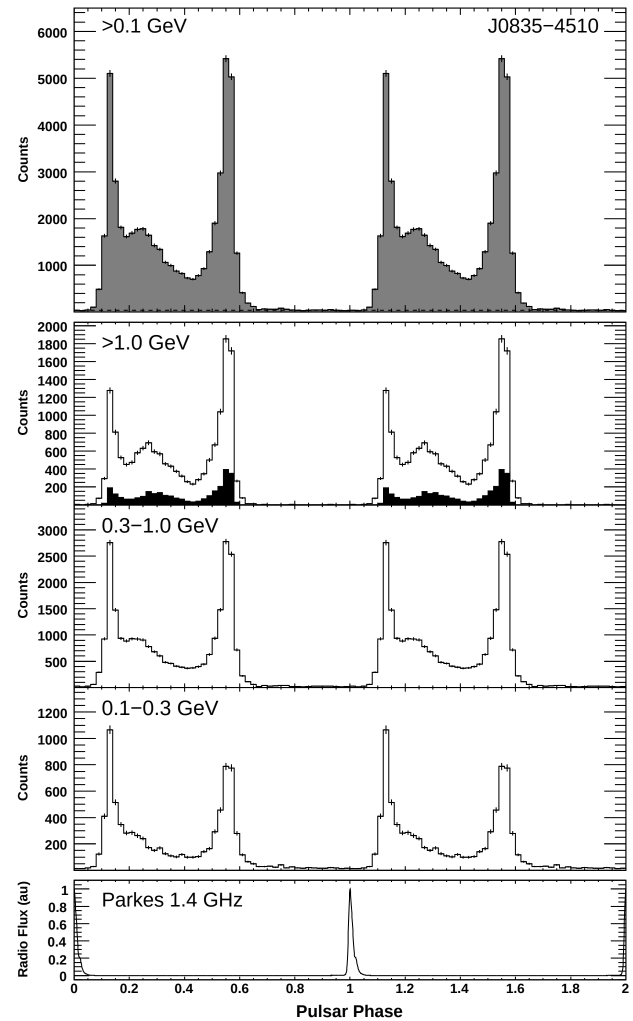

Fig. 28.— Light curves for PSR J0835–4510.

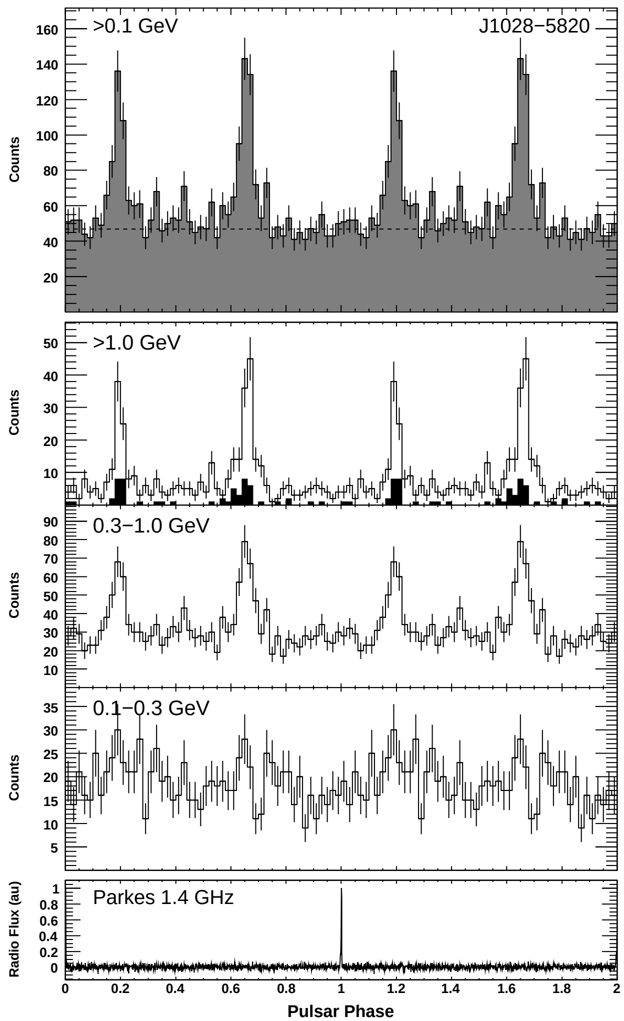

Fig. 29.— Light curves for PSR J1028–5820.

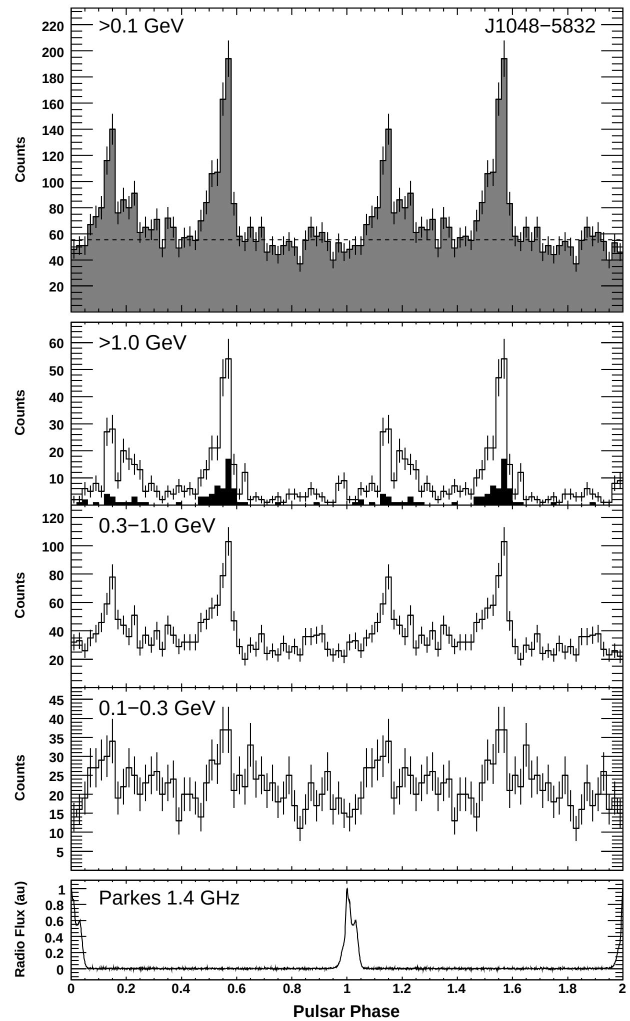

Fig. 30.— Light curves for PSR J1048–5832.

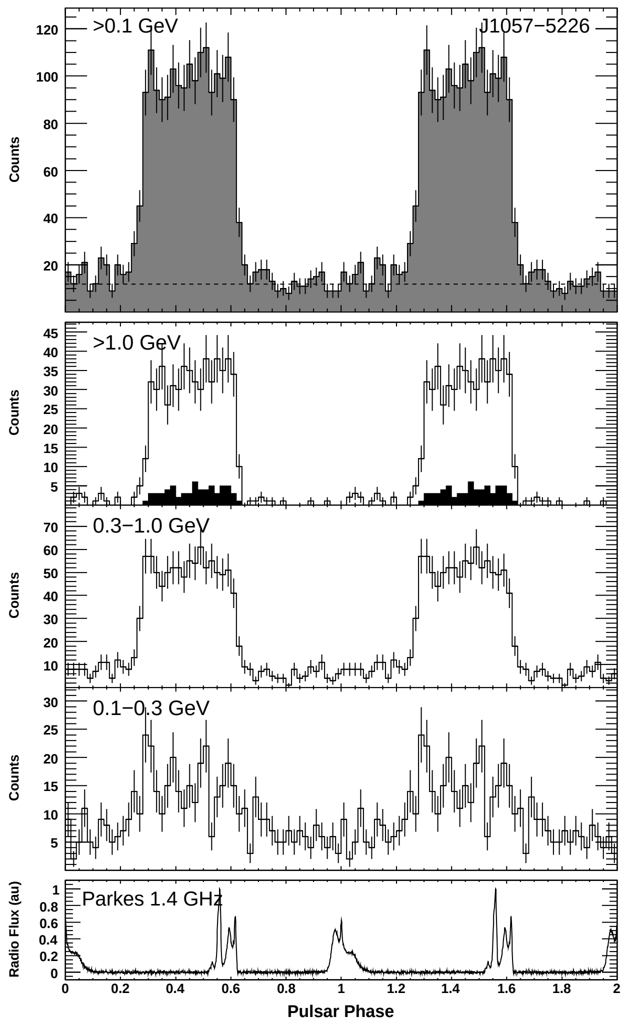

Fig. 31.— Light curves for PSR J1057–5226.

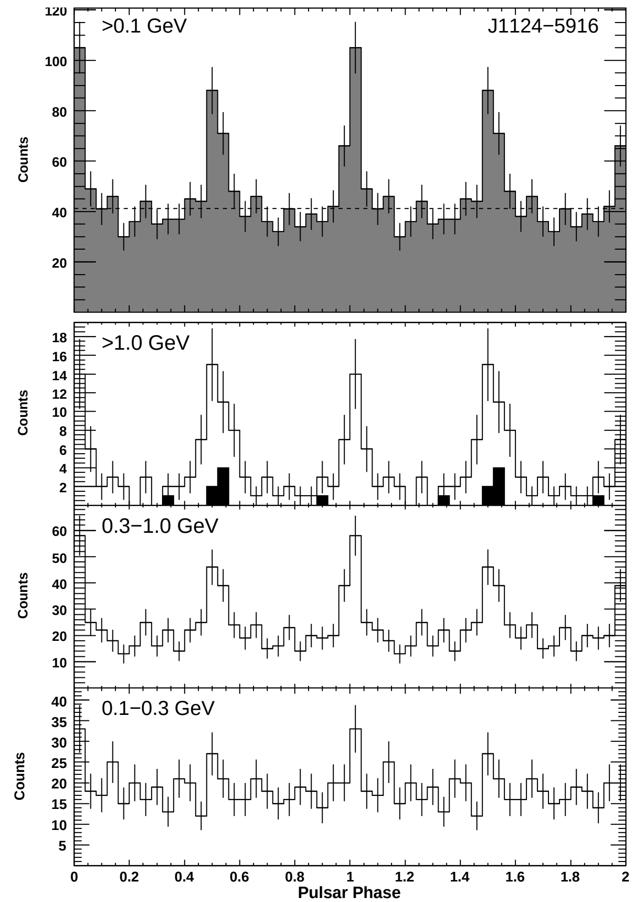

Fig. 32.— Light curves for PSR J1124–5916.

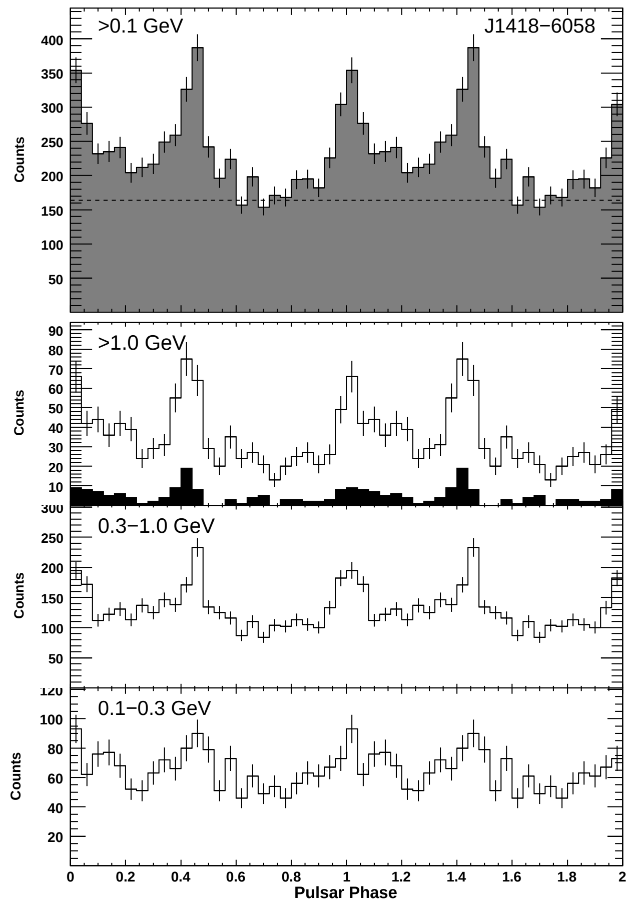

Fig. 33.— Light curves for PSR J1418–6058.

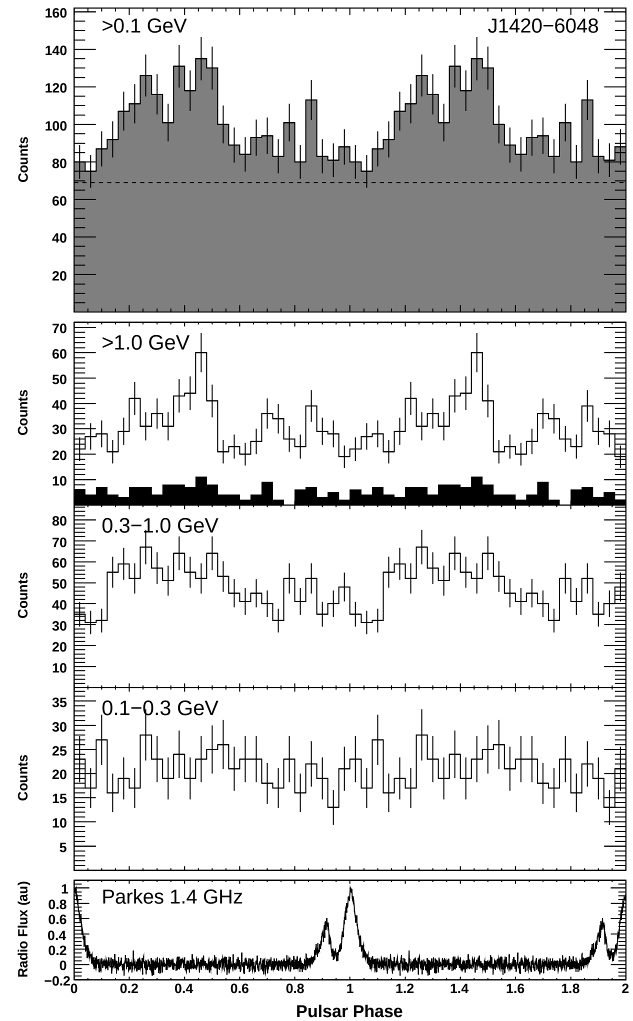

Fig. 34.— Light curves for PSR J1420–6048.

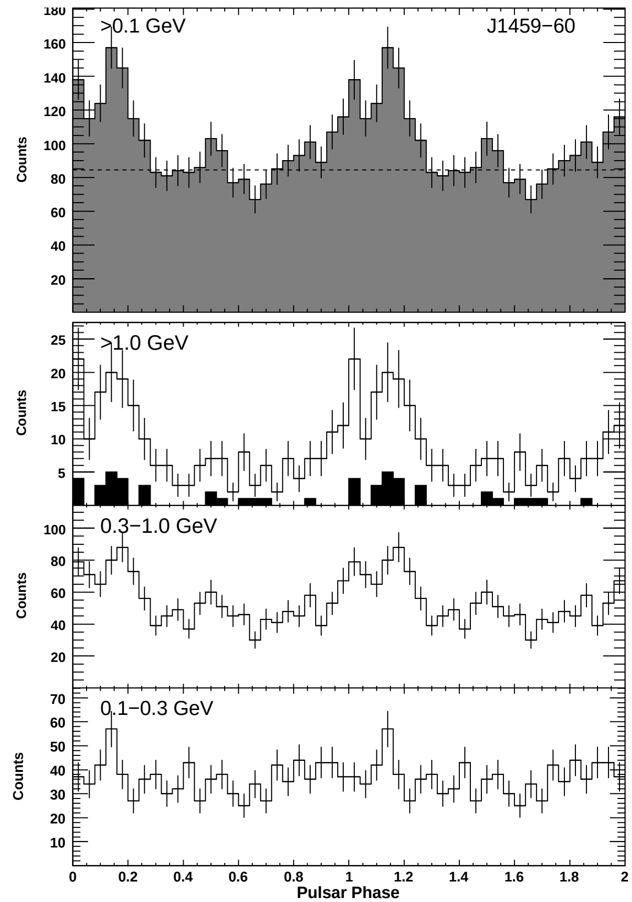

Fig. 35.— Light curves for PSR J1459–60.

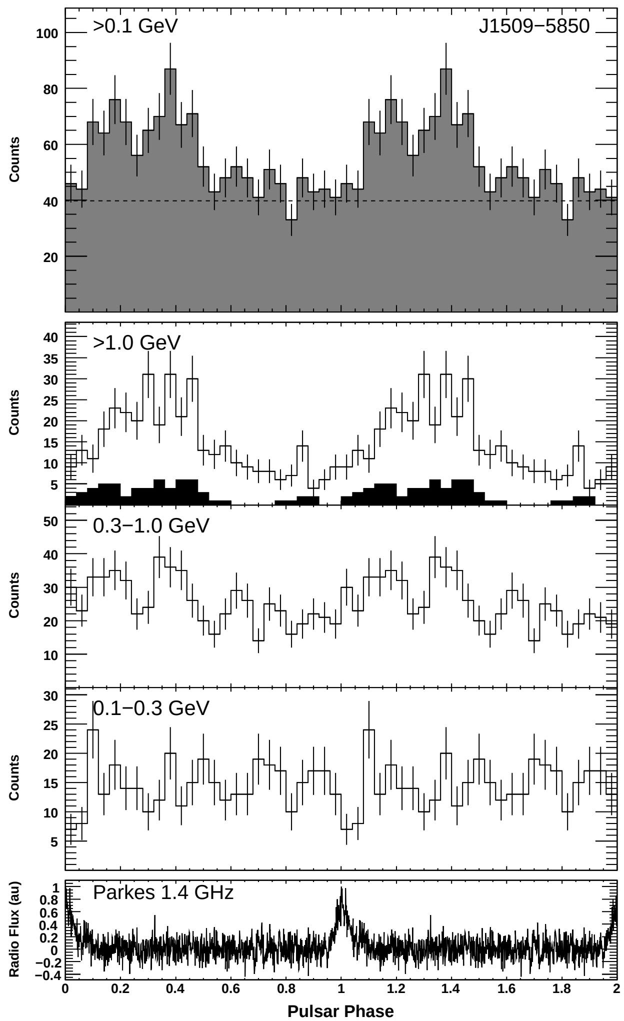

Fig. 36.— Light curves for PSR J1509–5850.

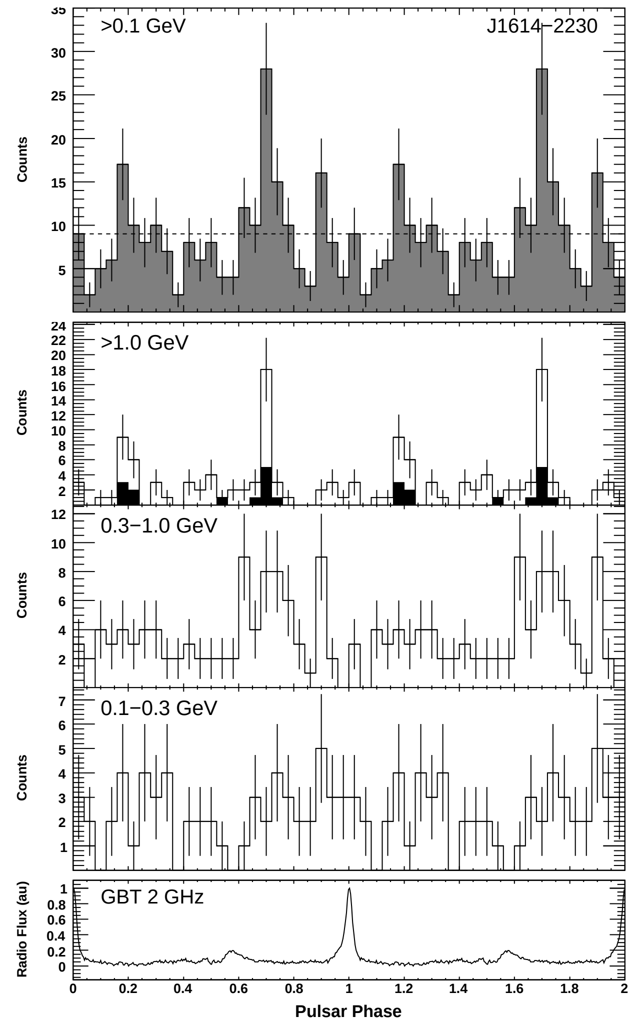

Fig. 37.— Light curves for PSR J1614–2230.

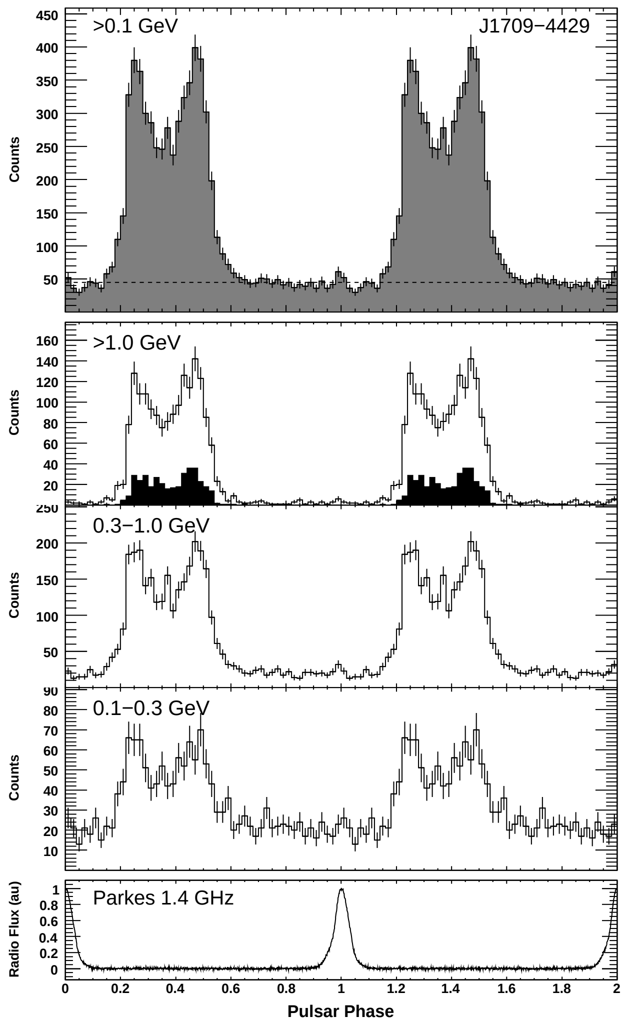

Fig. 38.— Light curves for PSR J1709–4429.

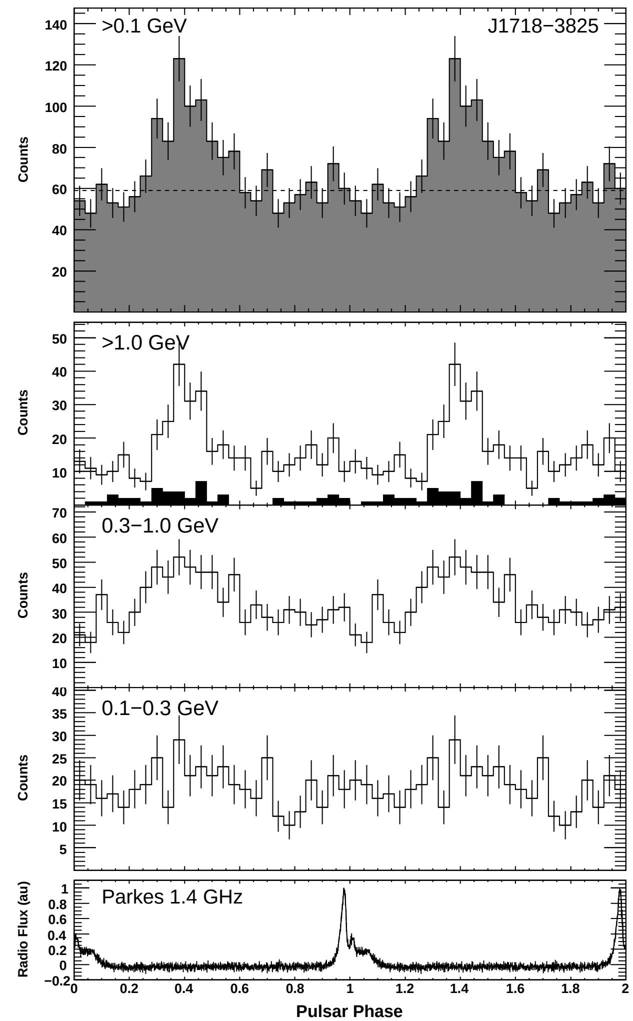

Fig. 39.— Light curves for PSR J1718–3825.

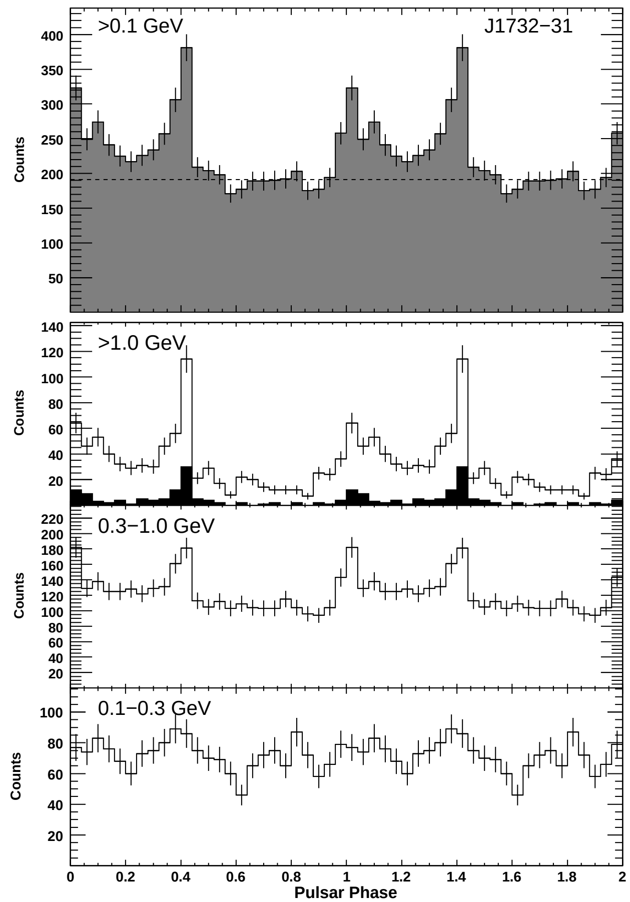

Fig. 40.— Light curves for PSR J1732–31.

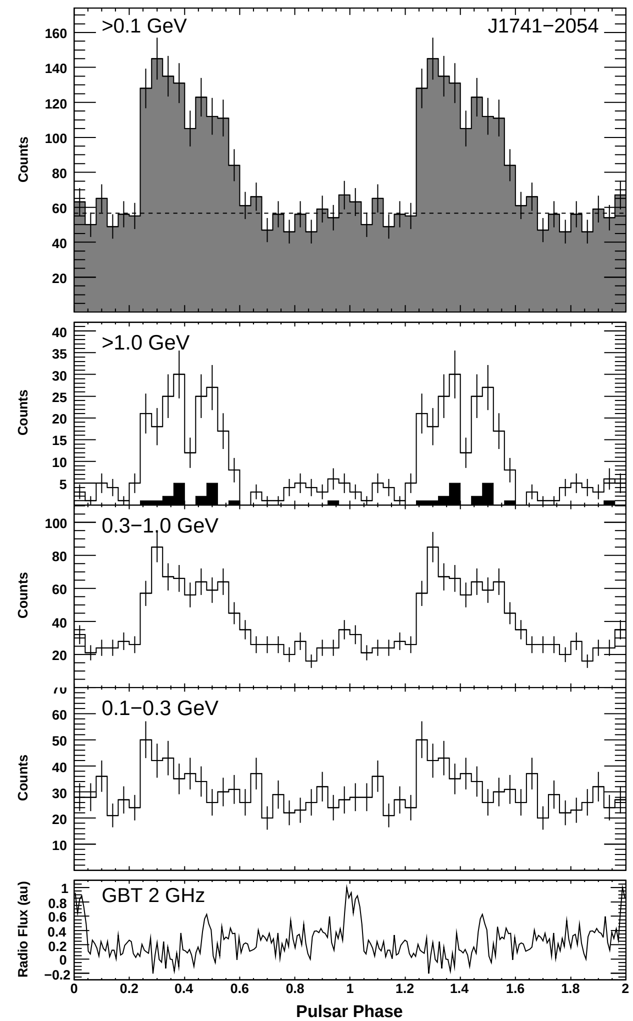

Fig. 41.— Light curves for PSR J1741–2054.

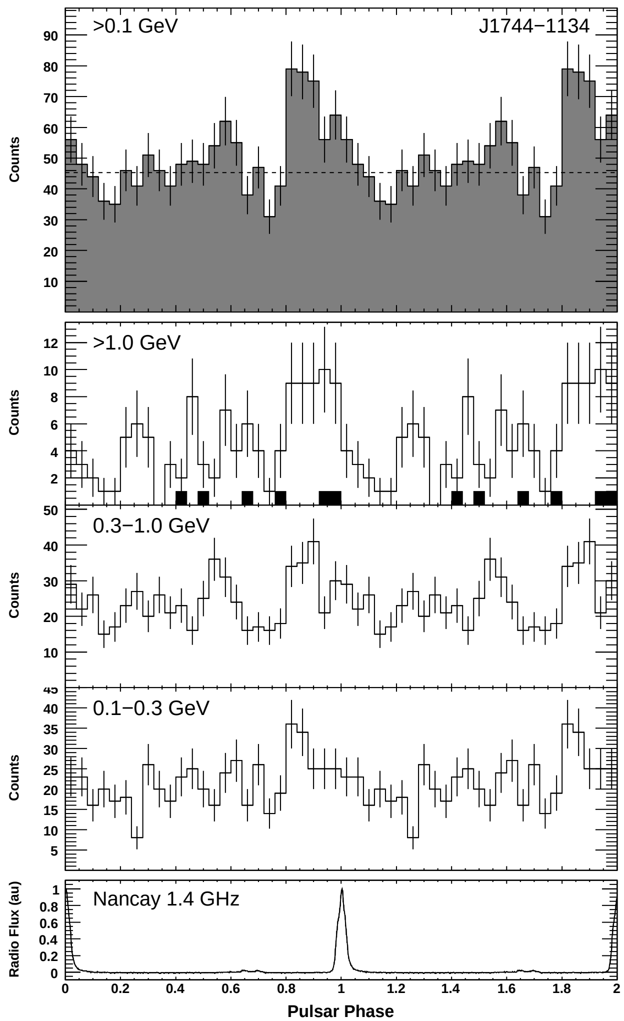

Fig. 42.— Light curves for PSR J1744–1134.

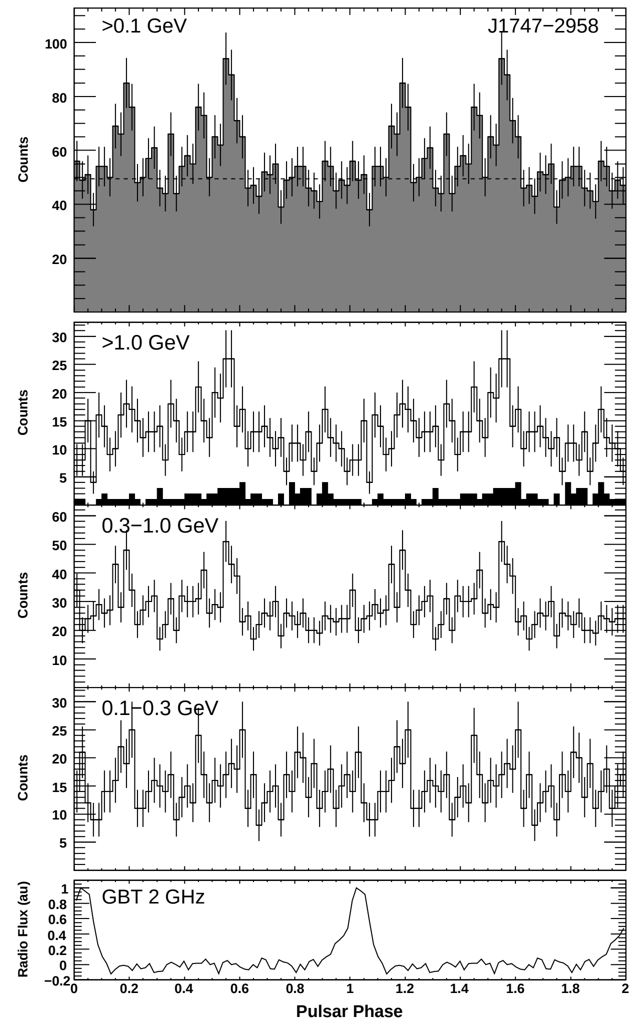

Fig. 43.— Light curves for PSR J1747–2958.

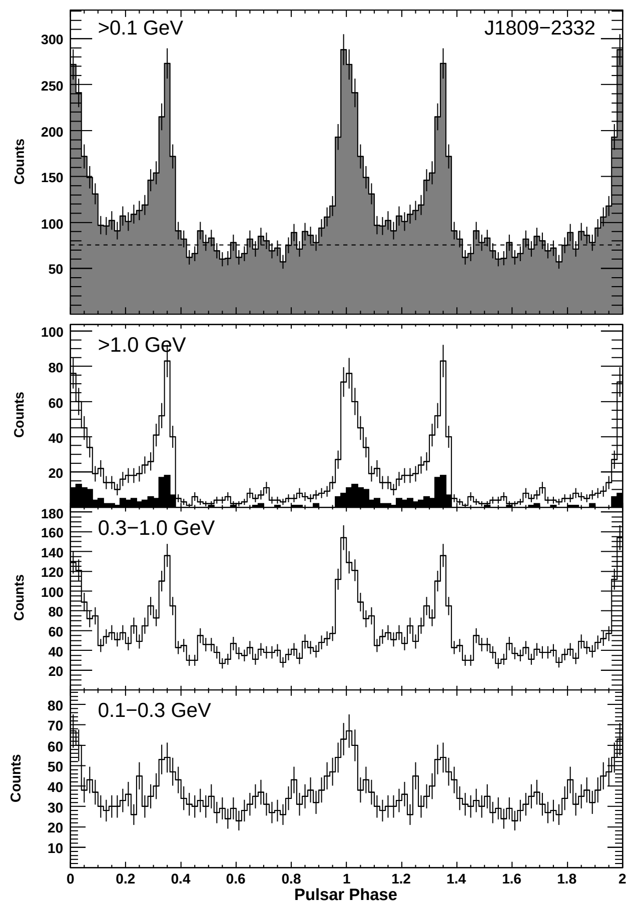

Fig. 44.— Light curves for PSR J1809–2332.

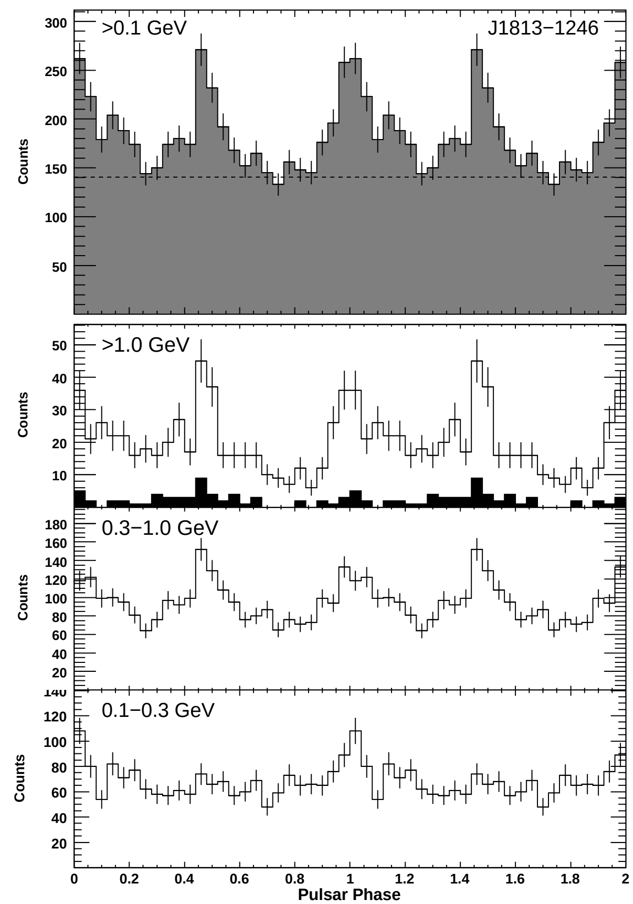

Fig. 45.— Light curves for PSR J1813–1246.

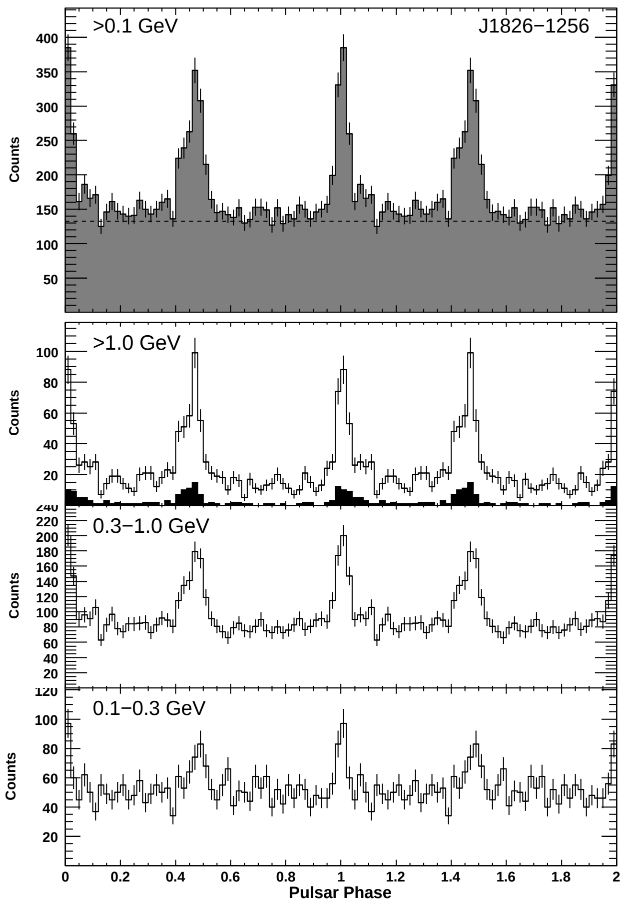

Fig. 46.— Light curves for PSR J1826–1256.

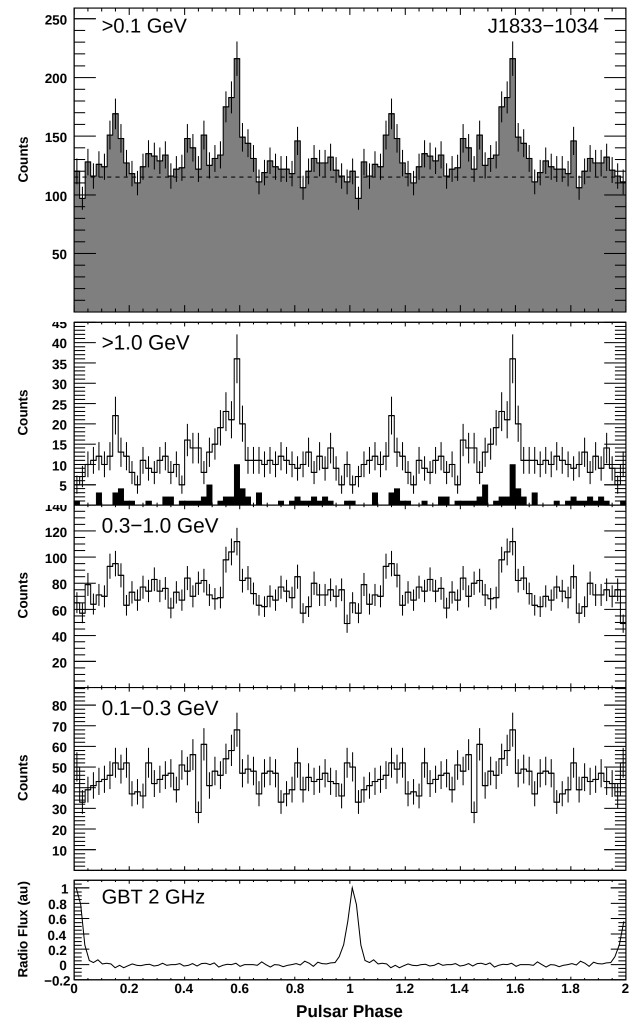

Fig. 47.— Light curves for PSR J1833–1034.

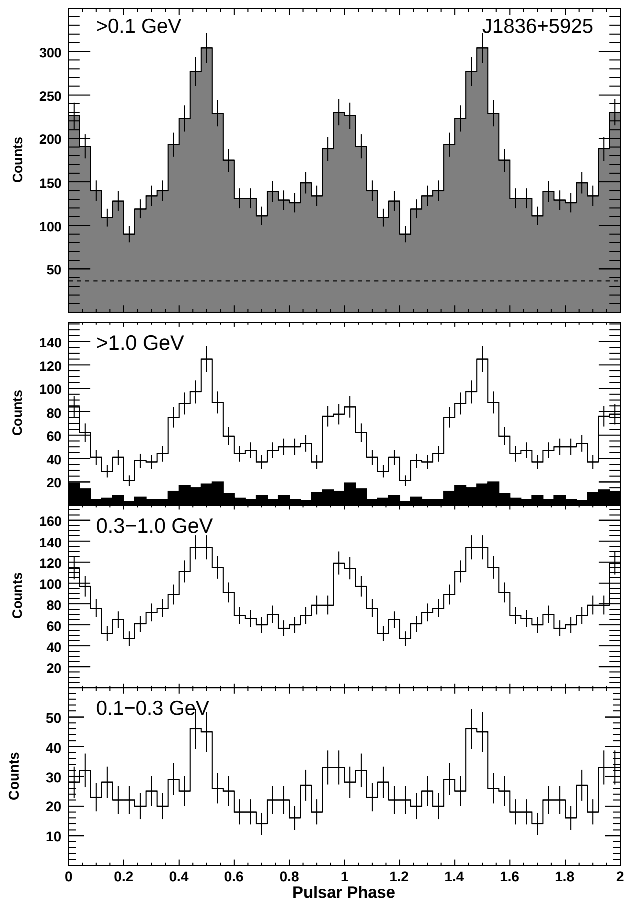

Fig. 48.— Light curves for PSR J1836+5925.

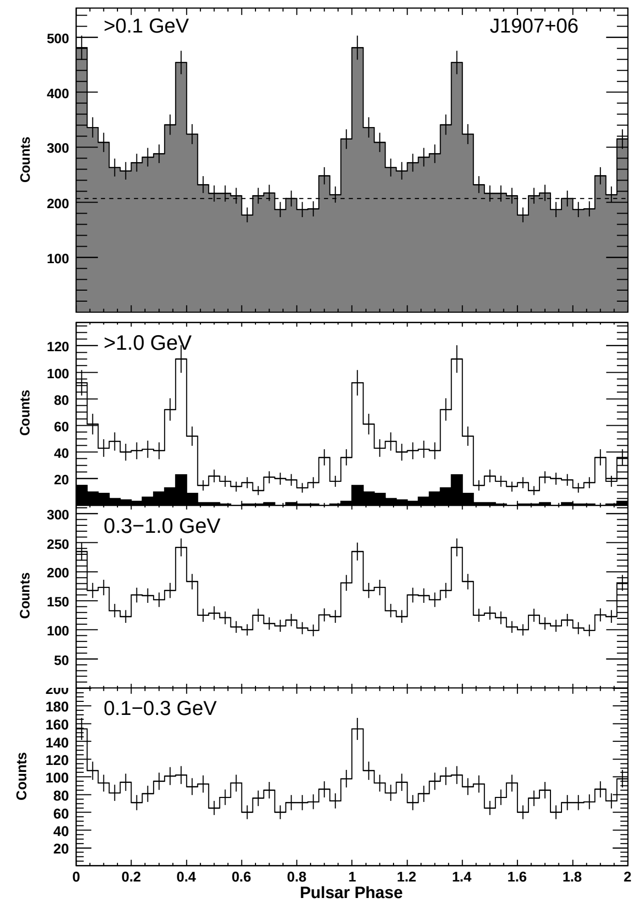

Fig. 49.— Light curves for PSR J1907+06.

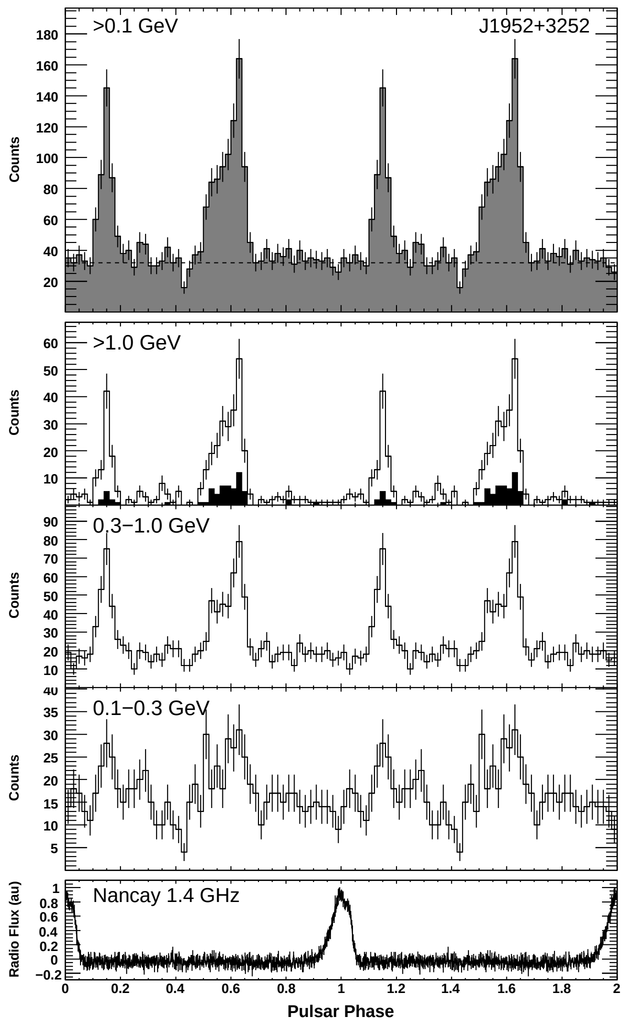

Fig. 50.— Light curves for PSR J1952+3252.

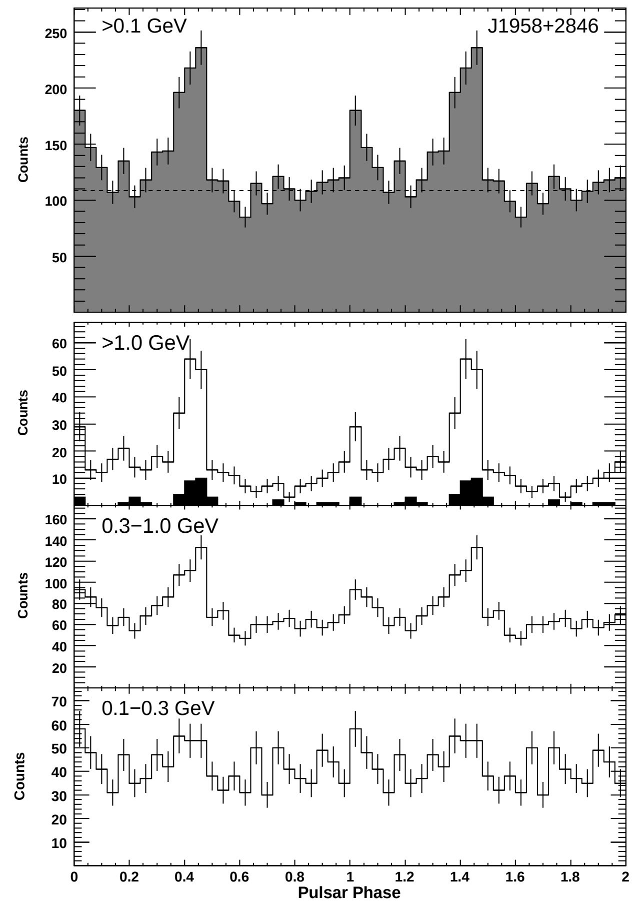

Fig. 51.— Light curves for PSR J1958+2846.

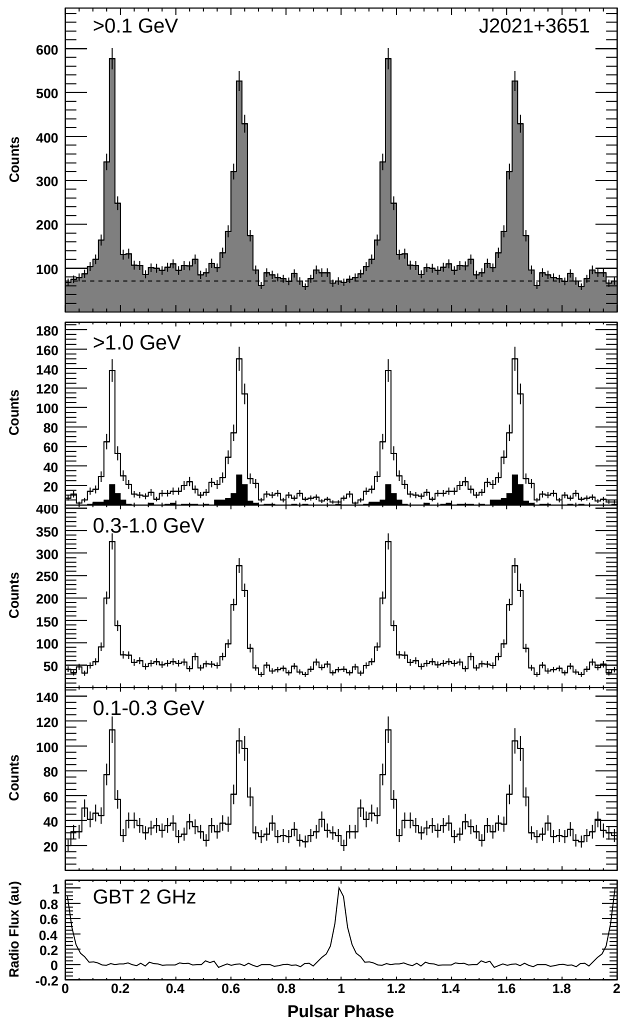

Fig. 52.— Light curves for PSR J2021+3651.

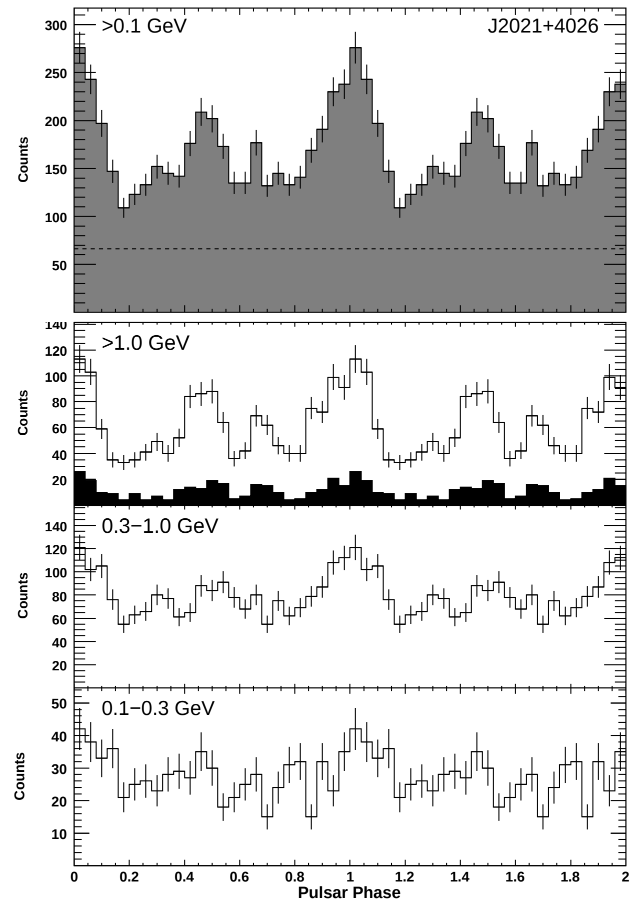

Fig. 53.— Light curves for PSR J2021+4026.

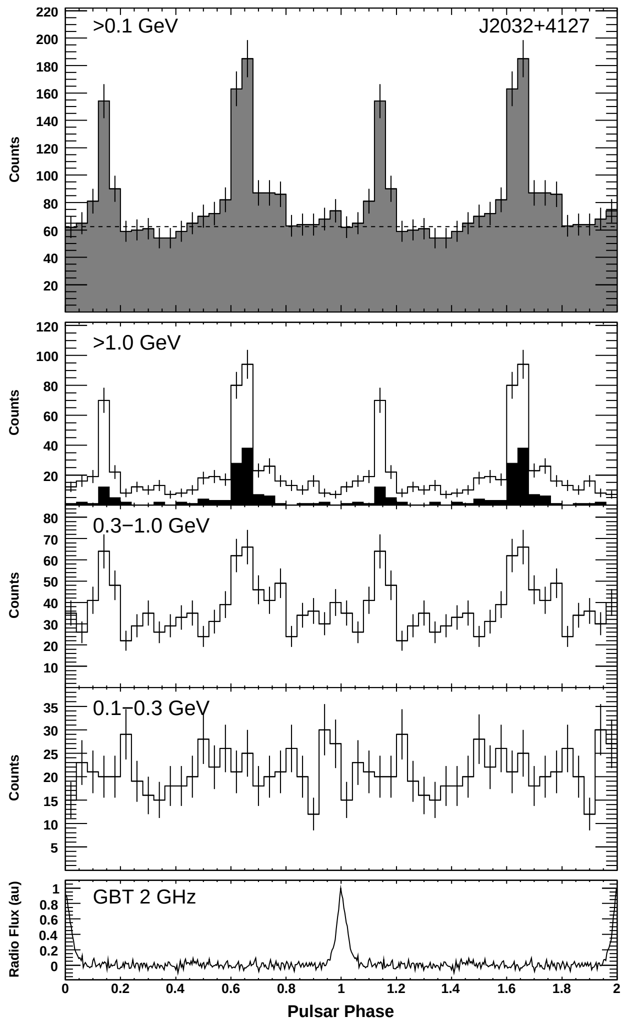

Fig. 54.— Light curves for PSR J2032+4127.

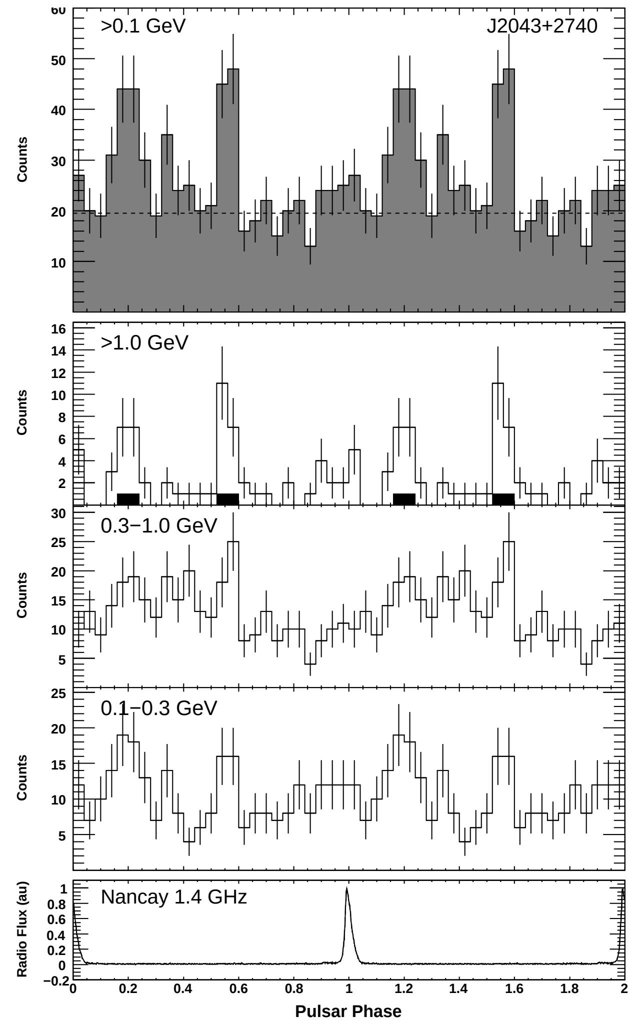

Fig. 55.— Light curves for PSR J2043+2740.

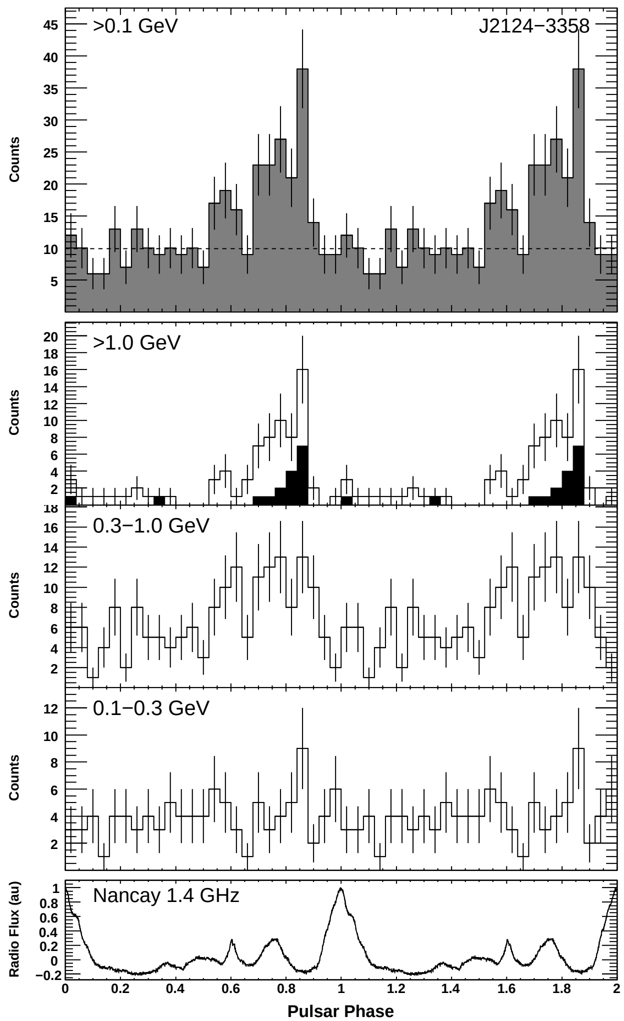

Fig. 56.— Light curves for PSR J2124–3358.

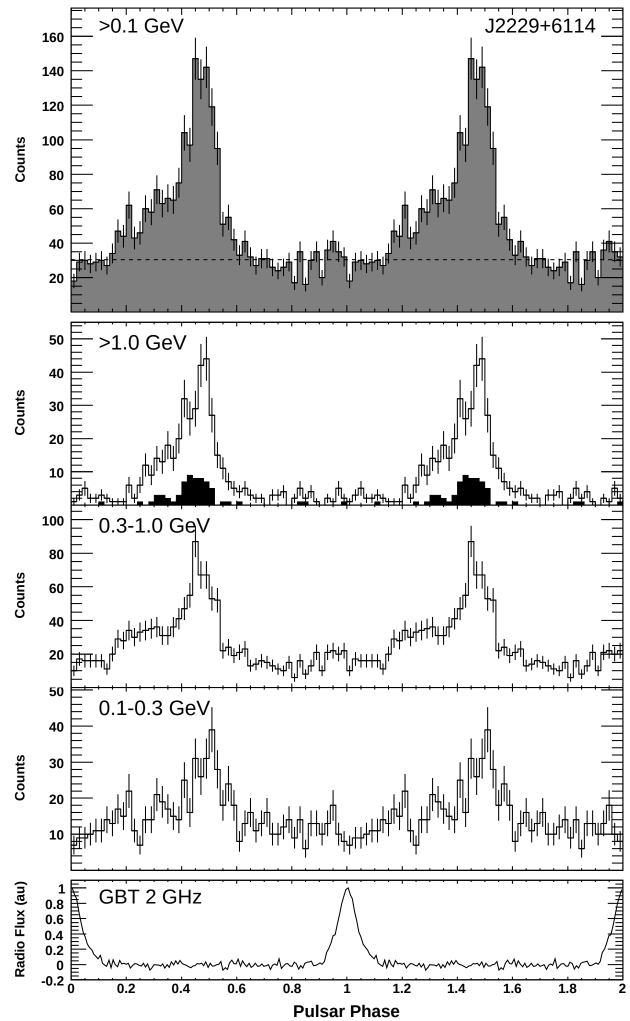

Fig. 57.— Light curves for PSR J2229+6114.

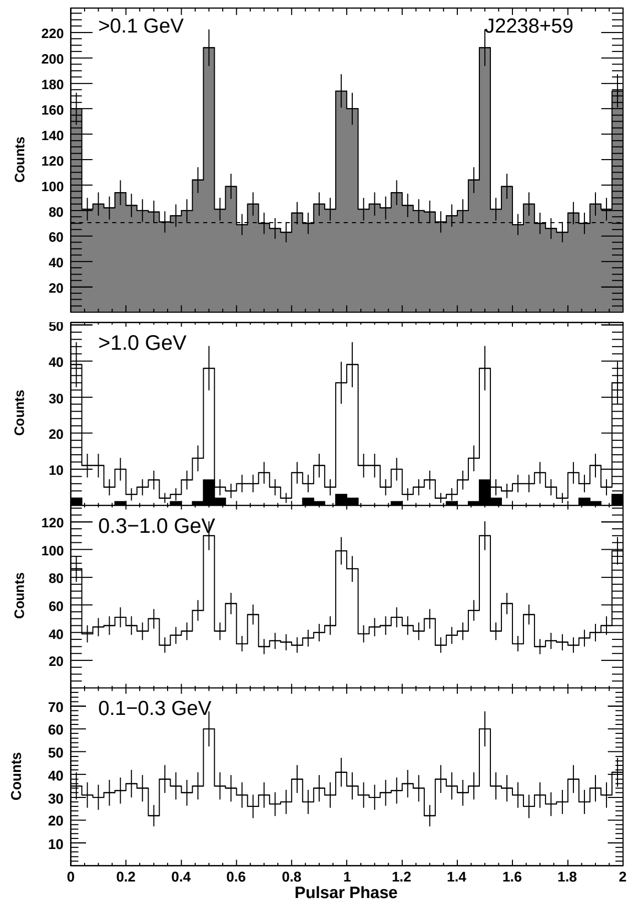

Fig. 58.— Light curves for PSR J2238+59.